Universität Rostock Traditio et Innovatio

# On Stability- and Fracture-Driven Failure of Engineering Materials and Architected Interfaces

**Doctoral thesis**
submitted in fulfillment of the requirements
for the academic degree Doctor of Engineering (Dr.-Ing.)
at the Faculty of Mechanical Engineering and Marine Technologies,
University of Rostock

submitted by

**Michelle Lund Sahl Hedvard**

**Reviewers:**

Prof. Dr.-Ing. Philipp Weißgraeber
University of Rostock
Chair of Lightweight Design

Dr.-Ing Lars Radtke
University of Rostock
Chair of Structural Mechanics

Date of submission: 22.01.2026
Date of defense: 23.03.2026

**Chair of Lightweight Design**
**2026**

https://doi.org/10.18453/rosdok_id00005798

# Acknowledgements

This thesis is the result of my work at the Chair of Lightweight Design at the University of Rostock. I would like to express my sincere gratitude to all those who have contributed to this work. I would like to thank Professor Dr.-Ing. Philipp Weißgraeber for the continuous support and guidance he granted throughout this work. I am grateful to my colleagues for their collaboration, valuable scientific discussions, and for creating a positive working atmosphere. A special thanks goes to Albrecht Radtke, with whom I have shared this entire journey. Finally, I would like to thank my friends and family for their support, especially my partner, Jonas.

# Abstract

Mechanical design never works without a choice of materials. The classical engineering materials available already span a wide range of properties. To expand the range further, the interest in mechanical metamaterials has increased. The architected topology of these materials has been demonstrated to yield superior material properties; however, novel analysis is necessary to comprehend and leverage the behavior of these materials. In the context of failure processes in engineering materials, the central aim of this thesis is to expand the material choice in mechanical engineering design.

Material selection requires an evaluation of multiple constraints and objectives in order to find the best compromise. Systematic, quantitative material selection methods, such as the Ashby method, help engineers navigate the large number of materials and their properties. In this work, the material selection process will be studied in detail with respect to the filtering of too brittle materials, which can lead to catastrophic failure of the product. The basis for such a filtering is defined by consideration of fundamental linear elastic fracture mechanics, leading to a fracture toughness-to-strength filtering ratio to distinguish between brittle and ductile failure. Based on a material dataset and by use of the Ashby chart, the effect of the proposed filtering method is evaluated. While previous fracture toughness-based filtering is too strict, the proposed filtering method provides a physically justified selection criterion for a more accurate classification.

To expand the horizon of available engineering materials, the interest in mechanical metamaterials has increased over the last decade with the development of additive manufacturing. To fully utilize these materials, it is essential to develop a comprehensive understanding of their failure mechanisms. However, these studies are still limited, especially in the field of confined metamaterials or architected interfaces, where boundary effects are introduced. In this work, novel approaches for examining the failure process of confined metamaterials are proposed, with a focus on stretching-dominated lattice interface materials. A numerical model that incorporates the failure of individual lattices is employed to assess the overall failure process and the impact of boundary conditions. Due to the confinement of the interface, small rotations can be imposed from deformations of the confining substrates of the lattice boundaries.

A concept of boundary rotation imperfections is proposed for the analysis of confined lattice structures that are rigidly connected to surrounding elements. Rotation imperfections may arise either as static imperfections or as kinematic imperfections governed by

the interactions between connected structural elements. Kinematically induced, load-dependent rotation imperfections can occur even in initially perfect structures and may therefore be easily overlooked. Nevertheless, such imperfections can lead to a substantial reduction in the load-bearing capacity, in some cases reducing the critical load below that of structures with connections allowing free rotation. The concept of rotation imperfections, together with geometrical imperfections, is incorporated into an analytical framework for the assessment of architected interfaces. Four critical evaluation points were identified for the damage onset along the lattices. While geometrical imperfections reduce the critical load across all interface densities, the influence of rotation imperfections is found to be most pronounced at higher relative densities, where bending stresses become increasingly significant. Additionally, softening of the interface due to buckling is identified for low relative densities by a numerical reference model.

This work contributes to improved material choices in mechanical design. By enhancing the methods to navigate among existing materials, a broader and more reliable span of materials becomes available. In addition, by advancing evaluation methods for confined mechanical metamaterials, introducing the concept of rotation imperfections of such lattice materials, and identifying relevant design rules, this work supports the ongoing work toward a deeper understanding and improved control of this promising material class.

# Contents


**1. Introduction** **1**
- 1.1. Motivation . . . 1
- 1.2. Research gap . . . 3
- 1.3. Scope and outline of the work . . . 5

**2. Theoretical background and state of the art** **7**
- 2.1. Material selection . . . 7
  - 2.1.1. Ashby chart method . . . 8
  - 2.1.2. Filtering of brittle materials . . . 11
- 2.2. Mechanical metamaterials . . . 13
- 2.3. Mechanical behavior of materials and structures . . . 17
  - 2.3.1. Linear elasticity theory . . . 17
  - 2.3.2. Linear theory of beams . . . 19
  - 2.3.3. Energy methods . . . 23
- 2.4. Stability of elastic structures . . . 25
  - 2.4.1. Classical Euler buckling . . . 25
  - 2.4.2. Imperfections . . . 26
  - 2.4.3. Buckling of lattice structures . . . 27
- 2.5. Fracture mechanics . . . 30
  - 2.5.1. Linear elastic fracture mechanics . . . 30
  - 2.5.2. Finite fracture mechanics . . . 33
- 2.6. Interface modeling . . . 35
  - 2.6.1. Double cantilever beam . . . 35
  - 2.6.2. Winkler foundation . . . 37
  - 2.6.3. Confined metamaterials . . . 38

**3. Material selection: A reevaluation of brittleness filters** **41**
- 3.1. Motivation for reevaluating the brittleness filter . . . 41
- 3.2. Theoretical deviation: LEFM filter . . . 44
- 3.3. Results and discussion . . . 45
  - 3.3.1. Evaluation of the LEFM filtering method . . . 45
  - 3.3.2. Screening using the LEFM filter . . . 46
  - 3.3.3. Material fracture toughness considerations . . . 47
  - 3.3.4. Material selection: mass minimization of deformation-limited design 49
  - 3.3.5. Material defect size . . . 50

3.4. Conclusion . . . 54

**4. Numerical modeling of stretching-dominated architected interfaces 55**
4.1. Introduction . . . 55
4.2. Numerical framework . . . 56
4.2.1. Considered structural situation . . . 56
4.2.2. Material damage model . . . 57
4.2.3. Analytical estimations . . . 59
4.2.4. Numerical setup . . . 60
4.3. Result and discussion . . . 61
4.3.1. Damage of lattice interfaces . . . 61
4.3.2. Bending of interface lattices . . . 65
4.3.3. Material fracture toughness . . . 67
4.4. Conclusion . . . 69

**5. Stability behavior of lattice structures 71**
5.1. Introduction . . . 71
5.2. Modeling approach . . . 72
5.2.1. Column buckling with static rotation imperfections . . . 72
5.2.2. Kinematic imperfections from column shortening . . . 78
5.2.3. Rigidly connected lattice structures . . . 81
5.2.4. Numerical reference model . . . 85
5.3. Results and discussion . . . 87
5.3.1. Static imperfections . . . 87
5.3.2. Kinematic imperfections from column shortening . . . 88
5.3.3. Case studies: lattice structures . . . 91
5.4. Conclusion . . . 97

**6. Compression failure of stretching-dominated architected interfaces 99**
6.1. Introduction . . . 99
6.2. Modeling approach . . . 100
6.2.1. Adherend deflection and rotation . . . 100
6.2.2. Failure of the pillar interface . . . 103
6.2.3. Numerical reference model . . . 107
6.3. Results and discussion . . . 108
6.3.1. Critical strain position . . . 108
6.3.2. Critical load for initially perfect interfaces . . . 109
6.3.3. Geometrical imperfection . . . 112
6.4. Conclusion . . . 113

**7. Conclusion and outlook 115**

**Bibliography 119**

A. Material list 135

# Nomenclature

## List of abbreviations

| | |
|---|---|
| BC | Boundary condition |
| CC | Continuity condition |
| CFRP | Carbon fiber reinforced polymer |
| CZ | Compression zone |
| DCB | Double cantilever beam |
| ERR | Energy release rate |
| FEA | Finite element analysis |
| FFM | Finite fracture mechanics |
| LEFM | Linear elastic fracture mechanics |
| ODE | Ordinary differential equation |
| PP | Polypropylene |
| SC | Symmetry condition |
| TZ | Tension zone |

## Latin symbols

| | |
|---|---|
| $A$ | Area |
| $A_{\mathrm{G}}, \tilde{A}_G$ | Geometrical imperfection amplitude, normalized |
| $a, \tilde{a}$ | Crack length, normalized |
| $\Delta A, \Delta a$ | Finite surface area, crack length |
| $B$ | Column distance |
| $B_{\mathrm{tot}}$ | Total beam length |
| $b$ | Width |
| $\boldsymbol{b}$ | Body force |
| $C_{\mathrm{a}}$ | Shear rigidity |
| $\mathbb{C}$ | Fourth-order elasticity tensor |
| $c$, $\tilde{c}$ | Compliance, normalized |
| $c_1, ..., c_6$ | Constants |
| $D_{\mathrm{a}}$ | Bending rigidity |
| $d_0$ | Initial imperfection displacement |

| | |
|---|---|
| $E$ | Young's modulus |
| $E_\mathrm{a}$ | Young's modulus of adherend |
| $E_\mathrm{D}$ | Softening tangent modulus |
| $E_\mathrm{i}$,$\tilde{E}_\mathrm{i}$ | Young's modulus of interface, normalized |
| $E_\mathrm{s}$ | Young's modulus of bulk material |
| $F$,$\tilde{F}$ | Force, normalized |
| $F_\mathrm{c}$ | Critical force |
| $F_\mathrm{Clamp}$ | Critical force assuming clamped Euler buckling |
| $F_\mathrm{CZ}$ | Critical force for compression-zone failure |
| $F_\mathrm{max}$ | Maximal force |
| $F_\mathrm{Pin}$ | Critical force assuming pined Euler buckling |
| $F_\mathrm{TZ}$ | Critical force for tension-zone failure |
| $G_\mathrm{a}$ | Shear modulus of adherend |
| $\mathcal{G}$ | Energy release rate |
| $\mathcal{G}_\mathrm{c}$ | Fracture toughness |
| $g$ | Geometrical imperfection fraction |
| $h_\mathrm{a}$ | Height of adherend |
| $h_\mathrm{i}, \tilde{h}_\mathrm{i}$ | Height of interface, normalized |
| $I$ | Second moment of area |
| $I_\mathrm{a}$ | Second moment of area of adherend |
| $I_\mathrm{b}$ | Second moment of area of confining beam |
| $K_\mathrm{I}$, $K_\mathrm{II}$, $K_\mathrm{III}$ | Mode I, II, and III stress intensity factors |
| $K_\mathrm{Ic}$, $K_\mathrm{IIc}$, $K_\mathrm{IIIc}$ | Mode I, II and III fracture toughness |
| $k$ | Spring stiffness |
| $k$ | Large constant for material softening |
| $L$ | Length |
| $L$,$\tilde{L}$ | Column height, normalized |
| $L_\mathrm{arc}$ | Arc length |
| $L_\mathrm{i}$ | Length of interface |
| $L_\mathrm{lever}$,$\tilde{L}_\mathrm{lever}$ | Lever length, normalized |
| $L_\mathrm{T}$ | Transition length |
| $l$ | Lattice length |
| $l_\mathrm{elm}$ | Element size |
| $\Delta L, \Delta\tilde{L}$ | Column shortening, normalized |
| $M$ | Material index |
| $M$ | Moment resultant |
| $M_\mathrm{B}$ | Reaction moment from the buckling process |
| $M_\mathrm{C}$ | Reaction moment in clamped connection |
| $M_\mathrm{Clamp}$ | Critical moment assuming clamped Euler buckling connections |
| $M_\mathrm{I}$ | Imperfection moment |
| $M_\mathrm{Pin}$ | Critical moment assuming pined Euler buckling |
| $m$ | Mass |
| $m$ | Buckling mode |
| $n$ | Boundary condition correction factor |
| $P, \tilde{P}$ | Compression load, normalized |

| | |
|---|---|
| $P_{\mathrm{cr}}$ | Critical Euler buckling load |
| $\mathcal{P}$ | Point |
| $\boldsymbol{p}$ | Position vector |
| $Q$ | Shear force resultant |
| $q$,$\boldsymbol{q}$ | Distributed load |
| $q_{\mathrm{Clamp}}$ | Critical load assuming Euler buckling under clamped connections |
| $q_{\mathrm{Pin}}$ | Critical load assuming Euler buckling under pined connections |
| $\boldsymbol{r}$ | Position vector |
| $r$ | Radius |
| $r_{\mathrm{p}}$ | Plastic zone size |
| $\mathcal{S}$ | Surface |
| $s$ | Unit cell size |
| $t$ | Lattice thickness |
| $\boldsymbol{t}$ | Traction vector |
| $u$,$v$,$w$ | Deflection in the $x$, $y$, $z$ direction respectively. |
| $\boldsymbol{u}$ | Displacement vector |
| $U$ | Strain energy |
| $W, \tilde{W}$ | Total column deflection, normalized |
| $W_{\mathrm{B}}$ | Column deflection from buckling |
| $W_{\mathrm{E}}$ | External work |
| $W_{\mathrm{I}}$ | Column deflection from imperfection |
| $W_{\Delta \mathrm{L}}$ | Column deflection for shorted column |
| $\tilde{w}$ | Normalized beam deflection |
| $X$,$Y$,$Z$ | Cartesian coordinates (column reference frame) |
| $x$,$y$,$z$ | Cartesian coordinates |
| $x_{\mathrm{Z}}$,$\tilde{x}_{\mathrm{Z}}$ | Transition point between tension and compression zones, normalized |
| $Y$ | Shape factor |
| $z$ | Scaling factor |

## Greek symbols

| | |
|---|---|
| $\alpha$,$\tilde{\alpha}$ | Imperfection amplitude, normalized |
| $\gamma$ | Shear parameter |
| $\Delta$ | Applied displacement |
| $\Delta_c$ | Critical displacement |
| $\delta, \tilde{\delta}$ | Deflection, normalized |
| $\delta_{\max}$ | Maximum deflection |
| $\epsilon$ | Threshold |
| $\boldsymbol{\varepsilon}$ | Linearized strain tensor |
| $\varepsilon$ | Strain |
| $\varepsilon_a$ | Axial strain |

| | |
|---|---|
| $\varepsilon_b$ | Bending strain |
| $\varepsilon_c$ | Critical strain |
| $\varepsilon_{\mathrm{com}}$ | Critical compressive strain |
| $\varepsilon_{\mathrm{max}}$ | Maximum strain |
| $\varepsilon_{\mathrm{min}}$ | Minimum strain |
| $\varepsilon_{\mathrm{ten}}$ | Critical tensile strain |
| $\varepsilon_{\mathrm{u}}$ | Cutoff strain |
| $\Theta$ | Total interface imperfection |
| $\Theta_{\mathrm{F}}$ | Imperfection from adherend rotation |
| $\Theta_{\mathrm{G}}$ | Geometrical imperfection of interface |
| $\theta$ | Boundary rotation |
| $\theta_0$ | Initial boundary rotation |
| $\lambda$ | Characteristic wavelength |
| $\Pi$ | Potential energy |
| $\rho, \tilde{\rho}$ | Density, relative |
| $\rho_{\mathrm{s}}$ | Density of bulk material |
| $\sigma$ | Stress |
| $\boldsymbol{\sigma}$ | Cauchy stress tensor |
| $\sigma_{\mathrm{c}}$ | Material strength |
| $\sigma_{\mathrm{s}}$ | Bulk material strength |
| $\sigma_{\mathrm{y}}$ | Yield strength |
| $\phi$ | Rotation |

# 1. Introduction

## 1.1. Motivation

Mechanical design always requires a choice of materials. Exploring new material brings new opportunities for the development and improvement of engineering products. A novel material choice is not limited to the use of novel materials but also includes already well-known materials in new settings. The design of a product is directly dependent on the material choice, the material characteristics, and the corresponding processing methods. Therefore, a clear idea of the material choice should be present from the early concept phase to specify the functional structure and design principles (Bender and Gericke, 2021). To navigate among the available materials, each material is characterized by a list of properties, such as density, strength, stiffness, fracture toughness, cost, environmental impact, etc., describing the overall material characteristics. A material selection must balance multiple objectives, including performance, economics, and environmental objectives. In many design cases, multiple material choices are required for a single product (see Figure 1.1a). To make good material choices, material selection processes provide a structured method to navigate between the over 200,000 engineering materials (Ashby, 2016).

The constantly growing demands for engineering designs require novel material choices, but also the development of novel materials to expand the material property range. The evolution of material composition over time can be illustrated by the case of the airplane. Initially, the structural material composition of airplanes was predominantly composed of wood and fabric (Boyer et al., 2015). Later, the dominant material was changed to aluminum and, more recently, to engineered materials of the lightweight carbon fiber reinforced polymers (CFRP) (see Figure 1.1b). The engineered materials, mechanical metamaterials, also known as architected materials, can achieve superior material properties, such as ultra-lightness and ultra-stiffness (Zheng et al., 2014), negative Poisson's ratios, high energy absorption, etc. (Surjadi et al., 2019). A few examples of such materials and use cases are presented in Figure 1.2. Mechanical metamaterials are driven by their geometrical structure on the mesoscale level, significantly altering the macroscopic material behavior compared to the base material, expanding the available material property range. However, due to the complex structure of such materials, the availability is highly dependent on the available production methods. With the development of additive manufacturing processes, the design possibilities for mechanical

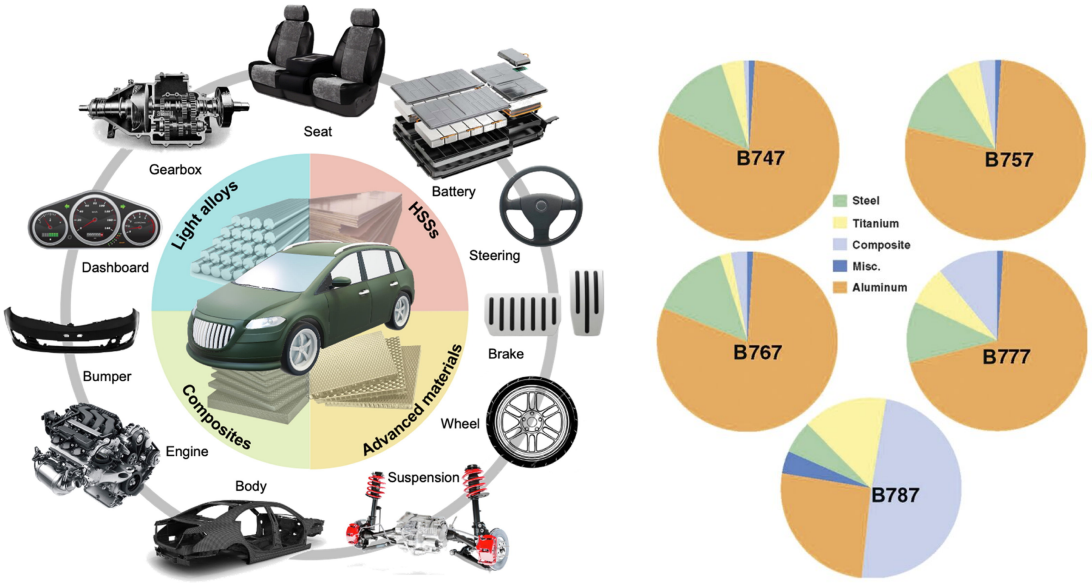


(a) (b)

Figure 1.1.: Material use in structural designs. (a) The components of an automobile (Zhang and Xu, 2022). (b) Materials used for Boeing commercial aircrafts. Reproduced with permission from Springer Nature (Boyer et al., 2015).

metamaterials are rapidly expanding, so structures that previously were only theoretically possible can today be fabricated with the feature size from nano-scale to meter-scale range (Fan et al., 2021; Lu et al., 2022).

A key aspect in mechanical engineering design is to make the product withstand critical loading. In this aspect, both strength failure and fracture are potential critical failure modes. When the stress concentrations are low, the failure analysis can be performed from the global stress field, where the material strength governs the design. Exceeding the material strength (e.g., yield strength) results in permanent strength failure. When introducing a defect, crack, or notch into the material, a local stress increase appears. For high stress gradients, the evaluation of the local stresses with respect to the material strength becomes insufficient, and the failure assessment must also include the energy-driven damage formation. For brittle materials, the energy-driven damage formation can be analyzed with respect to the material fracture toughness, where, in the special case of a crack with a square root singularity, the fracture toughness alone suffices for analyzing the fracture onset (Weißgraeber et al., 2016). While the global stress field can be found by a finite element analysis (FEA), the local stress intensification from the defects requires additional knowledge about potential defects, their sizes, and position. Design against fracture is generally more challenging. Additionally, fracture is a rapid form of failure, which is hard to detect before a catastrophic collapse occurs (Anderson, 2017). Therefore, for many design cases, ductile materials prone to strength failure are preferred.

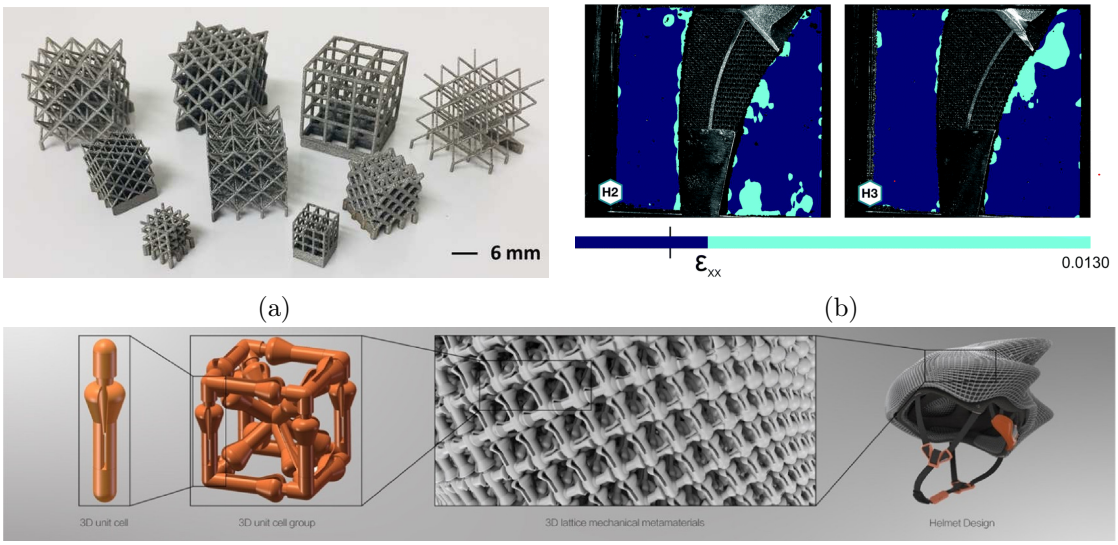


(a) (b)

(c)

Figure 1.2.: Mechanical metamaterials in the form of lattice structures. (a) Additive manufactured mechanical metamaterials. Reprinted from (Hanks et al., 2020) with permission from Elsevier. (b) Improved implant–bone contact for hip stems using mechanical metamaterials (Kolken et al., 2018). (c) Helmet design using a mechanical metamaterial with a two-step deformation and adjustable energy absorption (Liu et al., 2024).

## 1.2. Research gap

In material selection processes, brittle materials prone to fracture are often removed by a fracture toughness attribute limit already in the screening phase. Among engineers, there exists a rule of thumb to use an attribute limit of $K_{\mathrm{Ic}} > 15\,\mathrm{MPa}\sqrt{\mathrm{m}}$ (Ashby, 2016). However, filter limit values between $5 - 20\,\mathrm{MPa}\sqrt{\mathrm{m}}$ have also been reported in literature (Rashedi et al., 2012; Ferro and Bonollo, 2019). Considering that fractures are governed by the fracture toughness, the choice of the fracture toughness attribute limit might seem obvious. However, such attribute limits restrict the available material significantly to mainly metals and composites (see Figure 1.3). Thereby, also low-strength materials that never reach the fracture condition are eliminated. This includes the removal of ductile polymers, which are not brittle by any means. Accurate filtering methods are essential to the material selection process, determining the available materials for the further ranking phase. An overly restrictive filtering process can eliminate promising, innovative material candidates. In contrast, a filtering process that is not sufficiently restrictive includes unusable materials. A filtering method that takes both the potential of strength and fracture failure into account is needed to identify a more accurate filtering method for the screening phase of the material selection process.

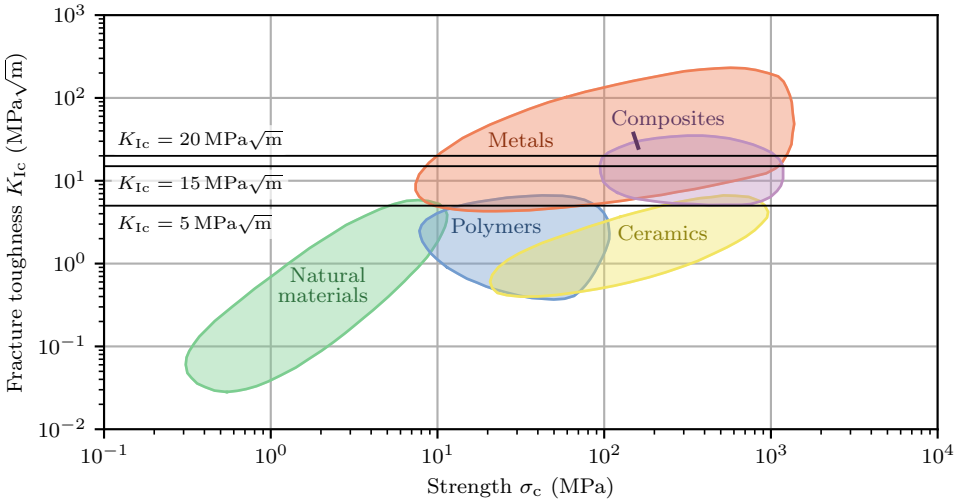


Figure 1.3.: Fracture toughness attribute limit values found in literature represented on an Ashby chart (Rashedi et al., 2012; Ashby, 2016; Ferro and Bonollo, 2019). Materials with a fracture toughness below the limit are removed in the material selection process. The diagram is adapted from (Ashby, 2016).

For conventional bulk materials, a wide range of standardized methods has been developed to evaluate the material strength (e.g. yield strength) and fracture toughness, characterizing the material's resistance to strength failure and fracture, respectively. For mechanical metamaterials, the characterization of strength and fracture toughness is more complex, where both the topology, relative density, material properties, and local effects must be taken into account. The study of damage and failure of mechanical metamaterials has increased significantly in recent years, with the focus on determining an effective strength or toughness of such materials for comparison to conventional materials (Tankasala et al., 2015; Chen et al., 2022; Shaikeea et al., 2022; Omidi and St-Pierre, 2023). However, for such materials, small changes such as the topology orientation (Gu et al., 2018), the number of unit cells placed in the crack length (Shaikeea et al., 2022), or the absence of a single lattice (Sanner et al., 2025) can have a significant effect on the material properties. Additionally, the architecture of the material can alter the damage pattern, which also influences the effective material properties (Tankasala and Fleck, 2020; Sanner et al., 2025).

In specific use cases, e.g., biomedical implants (Wang et al., 2023) or interface materials (Athanasiadis et al., 2021), the mechanical metamaterials are positioned in confined settings. While today mechanical metamaterials are typically studied under the assumption of an infinite length scale of the domain, confining the materials alters the boundary conditions. Such boundary changes can significantly alter the stress field or change the local material behavior or damage process (de Waal et al., 2025b). Considering

a mechanical metamaterial as an interface material, also referred to as an architected interface, introduces new opportunities for controlling the interface properties and damage process. However, the literature on confined metamaterials is limited and further studies are needed to fully understand the behavior and damage of confined metamaterials.

## 1.3. Scope and outline of the work

This work aims to improve the material selection of existing engineering materials and the analysis and design of mechanical metamaterials. Improving the material selection process is intended by introducing more accurate filtering criteria with respect to the consideration of brittle materials. Building on the principles of linear elastic fracture mechanics (LEFM), the objective is to develop physically justified methods for screening of brittle materials. In this work, the scope of mechanical metamaterials is restricted to confined, stretching-dominated lattice materials. With respect to the damage analysis of architected interfaces, this work aims to develop methods for the analysis of architected interfaces and improve the general understanding of the damage processes. A numerical method is developed for architected interfaces, allowing for damage to individual lattices. Through parametric analysis, the objective is to improve the general understanding of how architected interfaces are damaged in relation to their geometrical properties. With respect to stability-driven failure of lattice interfaces, the aim is to develop methods to account for boundary-induced imperfections from the interaction between connection elements of lattice structures. Improving the understanding of stability behavior and failure analysis of lattice structures and architected interfaces with respect to stiffness-related interaction between connected elements.

The work is separated into seven chapters. Chapter 2 introduces the theoretical background and state of the art, serving as a foundation for the presented work. Chapter 3 presents the novel filtering methods for the screening of brittle materials together with a validation and a detailed analysis of its effect on the material selection process. Chapter 4 presents a numerical method for the analysis of damage in architected lattice interfaces. The method is used for two stretching-dominated topologies where the damage patterns and failure modes are evaluated. Chapter 5 presents methods for stability analysis, including boundary-induced imperfections in lattice structures. Analyses of simple lattice structures are presented to emphasize the effect of the presented imperfection type. Chapter 6 introduces the boundary-induced imperfections to the stability-driven failure analysis of architected interfaces. Finally, Chapter 7 presents the conclusion together with an outlook with suggestions for further research. Figure 1.4 presents an overview of the content in chapters two to six.

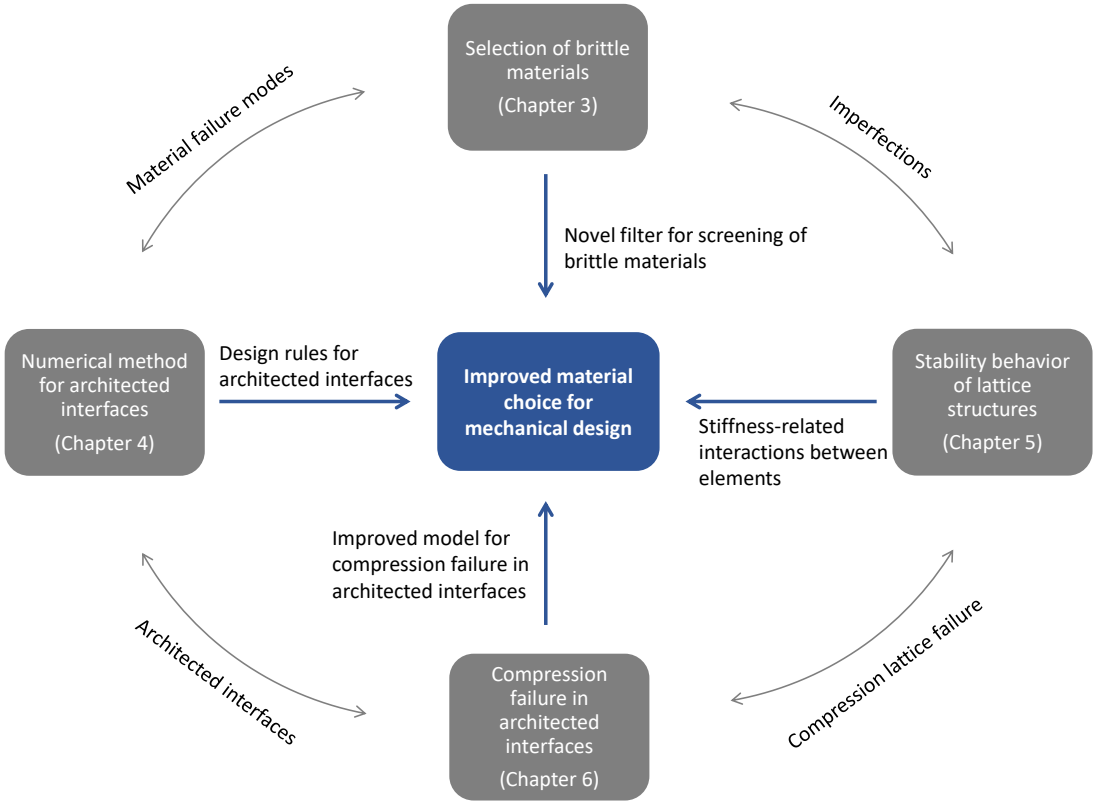


Figure 1.4.: Overview of the content in this work, its interactions, and its contribution to the main objective of improving the material choice in mechanical design.

# 2. Theoretical background and state of the art

*This chapter provides the relevant theoretical foundation for the present work. Topics include material selection methods with a focus on the Ashby chart method; metamaterials with a focus on lattice structures; mechanical behavior of materials and structures, with a focus on beam theory; stability of elastic structures, with a focus on buckling and imperfections; fracture mechanics, with a focus on the fracture of brittle materials; and interface modeling, with a focus on the modeling of confined metamaterials. Literature reviews are included for the selected topics: filtering of brittle materials, column buckling analysis including imperfections, buckling of lattice structures, and confined mechanical metamaterials.*

## 2.1. Material selection

Selecting the optimal material for a given design task in the early concept phase is challenging. Each material has a unique combination of properties (e.g., strength, modulus, cost, and density). Due to the wide variety of engineering materials currently available, the selection process must be approached systematically. The available material selection processes span various methods used to identify the materials that will perform best for a given task. In general, the material selection processes can be separated into four phases (Ashby, 2016; Rahim et al., 2020); (1) Translation of requirements: From the function intended for the design, the objective, constraint, and free variables must be identified. The constraints cover the non-negotiable conditions, for example, A coffee cup must be able to withstand temperatures up to 100 °C, the material inside a wire must have a low electrical resistivity, while the material around it must be an electrical insulator. The objectives describe what needs to be optimized, for example, minimizing the weight, cost or carbon footprint of a component or maximizing the strength. The free variables describe the parameters that are free to change. (2) Screening: Based on the constraints, all materials that are not suitable for the given design task are removed from the material selection process. This can be done by an evaluation of the material properties. An overview of available methods is provided in Figure 2.1a. (3) Ranking: The potential material candidates available after the screening methods are ranked based on

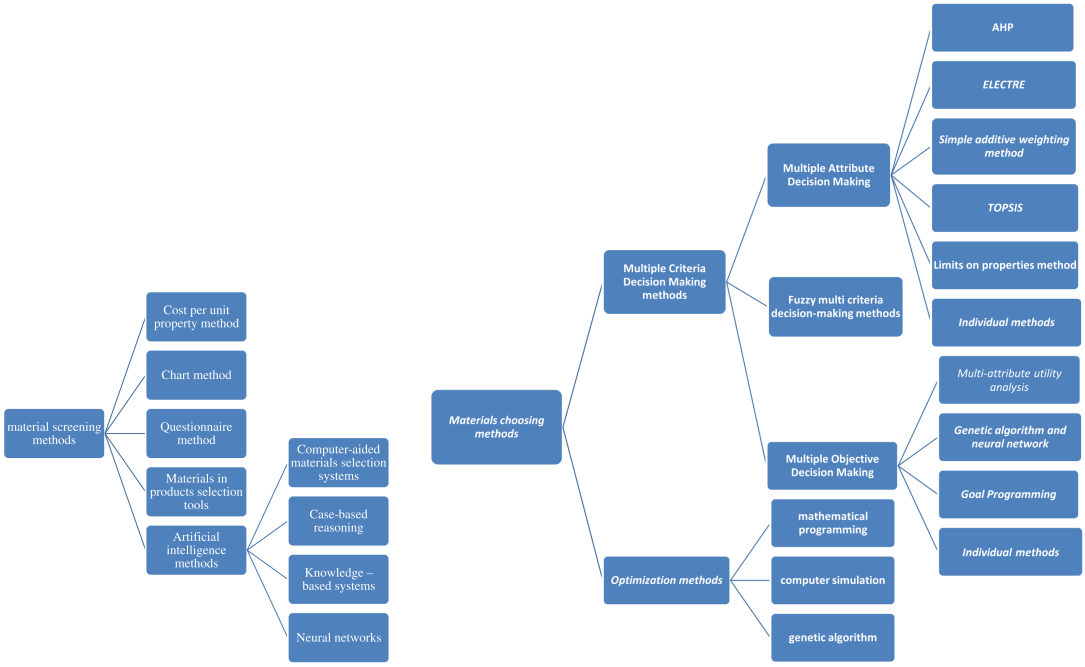


(a) Screening methods (b) Ranking methods

Figure 2.1.: Overview of available material selection methods from the literature. Reprinted from (Jahan et al., 2010), with permission from Elsevier.

the objectives. Multiple conflicting objectives are often present, which must be balanced to find the top-ranked materials. An overview of available methods ranking is provided in Figure 2.1b. (4) Additional knowledge: To make the final material choice, additional knowledge is required of the top-ranked materials. Consideration of the production methods, the environment, or other overlooked constraints that are not described by simple attribute limits must be taken into consideration. Gathering information about the workability, environmental impact, previous experiences, etc., is needed to compare the top-ranked materials in a broader spectrum and not overlook important drawbacks of the final design choice.

### 2.1.1. Ashby chart method

Ashby (1989) suggested a graphical method for the material selection procedure, representing the constraints and objectives on Ashby charts. Ashby charts provide a visual representation of the material properties by placing the materials on logarithmic scatter charts using the material properties for the axes. Materials from the same material classes cluster together and can be represented in the graph by a closed envelope, providing a structural overview of the different engineering material types. To navigate between the materials,

constraints and objectives can be represented on the chart by filter (e.g. attribute limits) or material indices, respectively. The requirements often lead to conflicting constraints or multiple objectives. Here, a single material will rarely be the optimal solution for the individual requirements and corresponding material indices; instead, a compromise is needed to find the best-performing material. In the Ashby approach for material selection, coupling equations and penalty functions are introduced to deal with such problems (Ashby, 2016). In literature, the Ashby approach is used for a wide range of material selection processes, such as the design of micro-electromechanical systems (MEMS) (Parate and Gupta, 2011; Mehmood et al., 2018), design of wind turbines (Rashedi et al., 2012), case study of travel luggage (Choi, 2023), or for football helmets Bird et al. (2018). van Innis and Pardoen (2024) use the method with respect to adhesive bondlines with varying thicknesses, considering both the material strength and fracture toughness in joint failure estimation. To visualize the procedure, the method is here described by a simple example.

**Example:** In this example, a material is needed for the design of a fishing net handle with a circular cross-section. The handle's length is denoted as $L$, and its radius of the cross-section is denoted as $r$. For ease of use, the handle should be light. When in use, the handle is estimated to behave as a cantilever beam loaded in bending, and the allowed deflection is limited to $\delta_{\max}$ when loaded by a force $F$. Since the handle will be used on water, it should float if dropped.
**(1) Translation of requirements:** First, the functions, constraints, and objective function and free variables are identified.

- Describe the function: the handle is considered as a cantilever beam loaded in bending.

- Constrains: Under the loading $F$ the deflection is constrained by $\delta \leq \delta_{\max}$. The bar must float on water, so the density of the material should be less than the density of water $\rho < 1000\,\mathrm{kg/m^3}$. Additionally, the length of the beam is fixed to $L$.

- Objective function: The objective is to minimize the mass for which the objective function is given by the mass of the beam $m = \pi r^2 L \rho$

- Free variables: The radius $r$ of the cross-sectional area and choice of material.

Next, the objective function is rewritten by replacing the free variables of the objective function with the constraints and rearranging the variables into groups of functional requirements, geometry, and material properties. In the given example, the maximum bending under loading

$$\delta = \frac{FL^3}{3EI} \leq \delta_{\max}, \tag{2.1}$$

where $E$ is Young's modulus of the material and $I = \pi r^4/4$. By isolating the free variable

$r$ and inserting it in the objective function, the objective function is given by

$$m \geq \sqrt{\frac{4\pi F}{3\delta_{\max}}}\sqrt{L^5}\frac{\rho}{\sqrt{E}}. \tag{2.2}$$

The lightest material that will fulfill all the requirements is the material minimizing the material parameters $\rho/\sqrt{E}$. The material index is usually defined as the function of the material parameters we seek to maximize to fulfill the objective, so in the given example, the material index is given by

$$M = \frac{\sqrt{E}}{\rho}. \tag{2.3}$$

Besides the material index Eq. (2.2) also identifies relations for the geometrical properties and functional requirements. As shown $m \propto L^{(5/2)}$, so doubling the length $L$ increases the mass by a factor of 5.7, while $m \propto 1/\delta_{\max}$ for which doubling the allowed deflection $\delta_{\max}$ halves the mass. The performance metric described the performance as a function of the functional requirements $F^*$, the geometric properties $G^*$, and the material properties $M^*$

$$p = f(F^*,G^*,M^*). \tag{2.4}$$

The performance metric can often be separated into three groups containing the functional requirements, the geometric properties, and the material properties $M^*$:

$$p = f_F(F^*)f_G(G^*)f_M(M^*), \tag{2.5}$$

for which the optimal material choice is independent of the choice of geometry $G^*$ and functional requirements $F^*$. The best performing material is then determined from the material index $f_M(M^*)$, independent of the final design details.

**(2) Screening:** Materials not satisfying the constraints are filtered out in the screening phase. In this example, the density is restricted to $\rho < 1000\,\mathrm{kg/m^3}$. This is graphically represented on Young's modulus - density chart in Figure 2.2. The vertical line at $\rho = 1000\,\mathrm{kg/m^3}$ represents the attribute limit, where the gray area to the right of the line (Ex.) indicates the excluded materials, while the area to the left of the line is the material remaining for the further ranking phase.

**(3) Ranking:** The materials remaining after the screening phase are ranked using an increasing material index. This is graphically represented on the Young's modulus - density chart for the material index $M = \sqrt{E}/\rho$ (see Figure 2.2). The material index represented by the dashed lines is moved in parallel to the upper left corner, marking the best-performing materials. Due to the logarithmic scale, the material indices are represented by a linear line with a slope of two. As the composites and ceramics were removed in the screening phase, the natural materials and foam materials are identified as the two top-performing material classes.

**(4) Additional knowledge:** To make the final design choice, additional knowledge needs to be taken into consideration for the top-ranked materials. Foam materials have a low Young's modulus, which increases the radius of the handle. Additionally, the porous

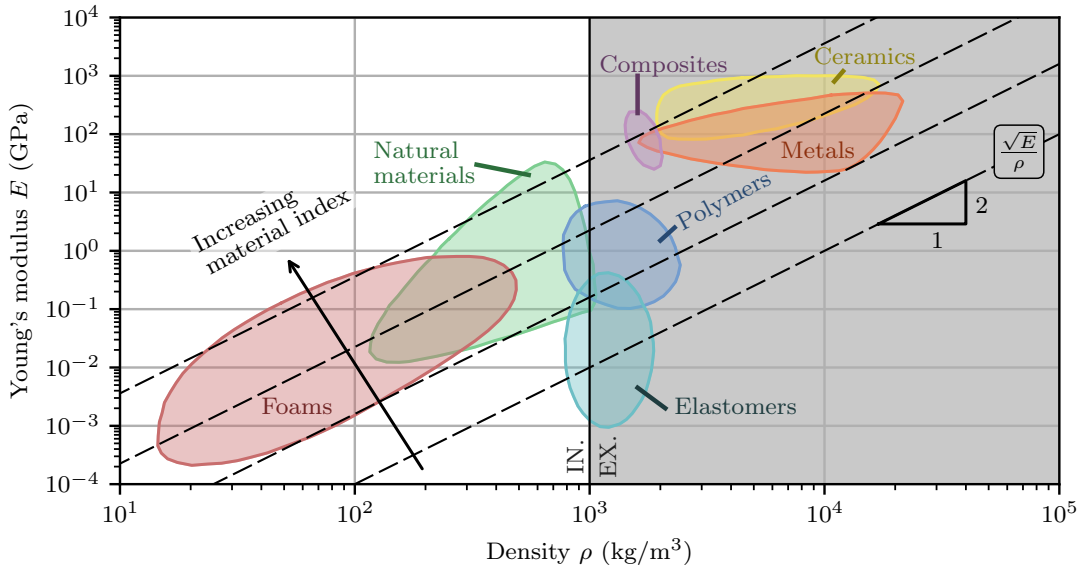


Figure 2.2.: Screening and ranking phase represented on a Young's modulus - density Ashby chart for deflection-limited beam under bending. Materials with a density below 1000 kg/m$^3$ are excluded (EX.) in the screening phase. The remaining included (IN.) materials are ranked by a material index. The Young's modulus - density diagram is adapted from (Ashby, 2016).

structure of foam materials can lead to high water absorption, which increases their weight when used in water and contradicts the objective of minimizing mass. An alternative material, such as wood, belonging to the natural materials, has a much higher modulus and is often used with respect to water for boats or rafts.

The example presented here is only meant as a simple example to visualize the overall procedure of the Ashby material selection methods. Better design choices can lead to better results. For example, using a hollow pipe for the handle would increase the second moment and the corresponding stiffness of the handle. If the ends are closed, this will also improve its ability to float, thereby relaxing the constraint of $\rho \leq 1000\,\mathrm{kg/m^3}$, including more materials in the ranking phase.

### 2.1.2. Filtering of brittle materials

Structural components must be able to withstand critical loads. In practice, damage is unavoidable. Defects may be introduced during manufacturing or develop over time, thereby altering the material's effective properties. Inspections are commonly employed to ensure safety and integrity, but these rely on gradual deterioration. Brittle materials are

prone to brittle fracture, a rapid and unstable damage process characterized by sudden crack initiation and fast propagation with little to no warning before failure. To mitigate this risk, it is beneficial in some design cases to exclude brittle materials in material selection processes in the screening phase.

The concept of brittleness has been characterized in the literature through various approaches. Lawn and Marshall (1979) suggested the material index of the hardness to fracture toughness ratio. Brostow et al. (2006) has quantified the brittleness of polymers in terms of elongation at break and storage modulus. While in the field of fracture mechanics, brittle materials are characterized by small process zones compared to the characteristic length (Ashby, 2016; Zhang and Zhou, 2022; Hua et al., 2023), often considered as the crack length (Anderson, 2017; Molnár et al., 2025). From a material selection point of view, brittleness is typically defined when the catastrophic failure of fracture is introduced at lower loads than other failure modes, e.g., yielding. Material resistance to fracture is characterized by the material properties: fracture toughness, which is either expressed by critical stress intensity factor $K_{\mathrm{Ic}}$ or the critical energy release rate $\mathcal{G}_{\mathrm{Ic}}$.

Different methods have been used in the material selection process to avoid fracture. In a material selection process for floor panels of refrigerated trucks Sirisalee et al. (2006) performed a material selection process with three conflicting objectives: minimizing the mass, cost, and heat loss. From a catalog of 2945 available materials 1760 were eliminated already in the screening phase from constraints on the density ($\rho \leq 10\,000\,\mathrm{kg/m^3}$), shear modulus ($G \geq 11\,\mathrm{GPa}$), and fracture toughness ($\mathcal{G}_{\mathrm{c}} \geq 1\,\frac{\mathrm{kJ}}{\mathrm{m^2}}$). In a case study for mass minimization of the metro vehicle interior grab rail Carruthers et al. (2009) performed a material selection process using the Ashby approach where brittle materials were removed by a constraint on the fracture toughness ($K_{\mathrm{Ic}} > 10\,\mathrm{MPa}\sqrt{\mathrm{m}}$). Rashedi et al. (2012) have also considered an attribute limit on the fracture toughness ($K_{\mathrm{Ic}}$), in a material selection process of wind turbines. A fracture toughness limit value of $5\,\mathrm{MPa}\sqrt{\mathrm{m}}$ was used for small blades, while a limit of $15\,\mathrm{MPa}\sqrt{\mathrm{m}}$ was used for larger blades and the tower. Ferro and Bonollo (2019) used the fracture toughness limit of $K_{\mathrm{Ic}} > 20\,\mathrm{MPa}\sqrt{\mathrm{m}}$ for the material selection, considering a bicycle fork. Ashby (2016) have identified three rules of thumb against brittle fracture. For load-limited designs $K_{\mathrm{Ic}} > 15\,\mathrm{MPa}\sqrt{\mathrm{m}}$, for energy limited designs $\mathcal{G}_{\mathrm{c}} > 1\,\frac{\mathrm{kJ}}{\mathrm{m^2}}$ and for displacement limit designs $\frac{K_{\mathrm{Ic}}}{E} > 0.001\,\sqrt{\mathrm{m}}$. For a case study of an oar, they used the constraint of $\mathcal{G}_{\mathrm{c}} > 1\,\frac{\mathrm{kJ}}{\mathrm{m^2}}$ to avoid brittle materials. An overview of the methods is provided in the Table 2.1. As shown, for the screening phase, fracture toughness attribute limits are used as a constraint to avoid brittle materials. For the ranking phase, the approach for avoiding brittle fracture is different. Ashby (2016) has presented different case studies, all with the aim of avoiding brittle fracture. The limit of brittle facture can be used as a constraint to rewrite the objective function of a volume minimization, resulting in a material index of $M = K_{\mathrm{Ic}}$ for load-limited design, $M = K_{\mathrm{Ic}}^2/E$ for energy limited design and $M = K_{\mathrm{Ic}}/E$ for displacement limited design. For a safe pressure vessel, the material index of $M = K_{\mathrm{Ic}}/\sigma_y$ was derived from the objective of designing a pressure vessel that must yield before fracture, while the

Table 2.1.: Material selection methods to avoid brittle fracture. The material fracture toughness is given by $K_{\mathrm{Ic}}$ or $G_{Ic}$, $E$ is Young's modulus of the material and $\sigma_y$ is the material yield strength. For the ranking phase, $M$ refers to the material index.

| Phase | Reference | Application | Method |
|---|---|---|---|
| Screening | (Sirisalee et al., 2006) | Floor panels of refrigerated trucks | $\mathcal{G}_{\mathrm{c}} \geq 1\,\frac{\mathrm{kJ}}{\mathrm{m}^2}$ |
| Screening | (Carruthers et al., 2009) | Metro vehicles of | $K_{\mathrm{Ic}} > 10\,\mathrm{MPa}\sqrt{\mathrm{m}}$ |
| Screening | (Rashedi et al., 2012) | Wind turbines | Small blades: $K_{\mathrm{Ic}} > 5\,\mathrm{MPa}\sqrt{\mathrm{m}}$<br>Large blades: $K_{\mathrm{Ic}} > 15\,\mathrm{MPa}\sqrt{\mathrm{m}}$<br>Towers: $K_{\mathrm{Ic}} > 15\,\mathrm{MPa}\sqrt{\mathrm{m}}$ |
| Screening | (Ashby, 2016, table 5.18) | Rule of thumb | Load limited: $K_{\mathrm{Ic}} > 15\,\mathrm{MPa}\sqrt{\mathrm{m}}$<br>Energy limited: $\mathcal{G}_{\mathrm{c}} > 1\,\frac{\mathrm{kJ}}{\mathrm{m}^2}$<br>Displacement limited: $\frac{K_{\mathrm{Ic}}}{E} > 0.001\,\sqrt{\mathrm{m}}$ |
| Screening | (Ashby, 2016, p. 147) | Oars | $\mathcal{G}_{\mathrm{c}} > 1\,\frac{\mathrm{kJ}}{\mathrm{m}^2}$ |
| Screening | (Ferro and Bonollo, 2019) | Bicycle forks | $K_{\mathrm{Ic}} > 20\,\mathrm{MPa}\sqrt{\mathrm{m}}$ |
| Ranking | (Ashby, 2016, pp. 177-178) | Fracture limited design | Load limited: $M = K_{\mathrm{Ic}}$<br>Energy limited: $M = \frac{K_{\mathrm{Ic}}^2}{E}$<br>Displacement limited: $M = \frac{K_{\mathrm{Ic}}}{E}$ |
| Ranking | (Ashby, 2016, pp. 181-182) | Safe pressure vessel | Load limited: $M = K_{\mathrm{Ic}}$<br>Yield before break: $M = \frac{K_{\mathrm{Ic}}}{\sigma_y}$<br>Leak before break: $M = \frac{K_{\mathrm{Ic}}^2}{\sigma_y}$ |
| Ranking | (Ashby, 2016, p. 325) | Light pressure vessel | No yielding: $M_1 = \frac{\rho}{\sigma_y}$<br>No fracture: $M_2 = \frac{\rho}{K_{\mathrm{Ic}}}$<br>Coupling: $M_1 = \sqrt{c\pi}M_2$ |

material index becomes $M = K_{\mathrm{Ic}}^2/\sigma_y$ from the objective of leak before fracture. For a light-pressure vessel, the material indices of minimizing the potential of strength and fracture failure were derived individually as two conflicting objectives and are combined by a coupling function.

## 2.2. Mechanical metamaterials

Mechanical metamaterials are a class of materials for which the effective properties are governed primarily by topology rather than by the intrinsic properties of the base material. Through the architectural design, these metamaterials can exhibit superior mechanical properties and property combinations that are not accessible by conventional materials. A wide variety of metamaterial structures are available today, including beam-based, plate-based, and minimal-surface-based topologies (see Figure 2.3). Material properties such as ultra-high strength-to-density and stiffness-to-density ratios (Zheng et al., 2014), high and adaptive energy absorption (Wang et al., 2026), and ultra-high load-bearing capacity

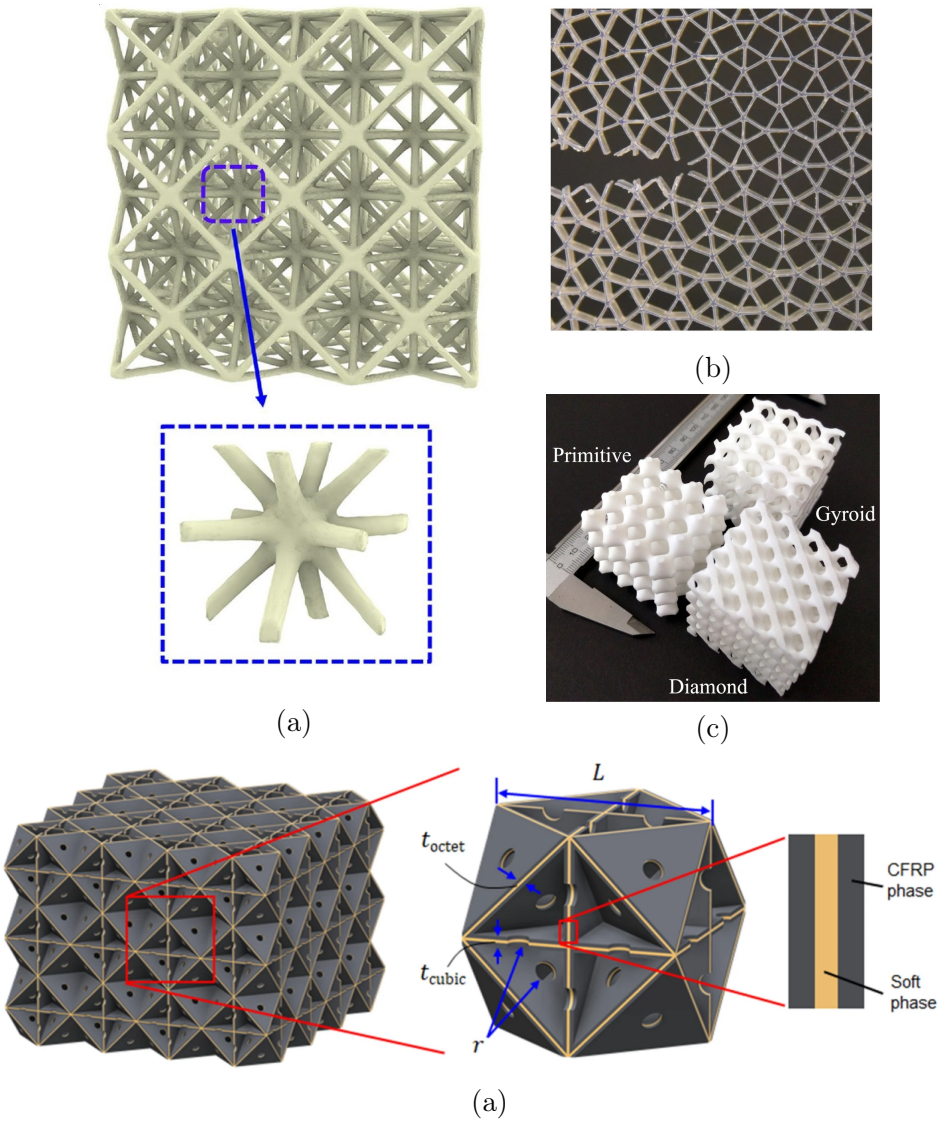


Figure 2.3.: Mechanical metamaterials examples for (a) 3D lattice structure represented by an octet truss lattice structure. Reprinted from (Chen et al., 2022) with permission from Elsevier. (b) 2D lattice structure represented by a snub-square lattice structure with an edge crack (Omidi and St-Pierre, 2023). (c) Minimum surface structures (Maskery et al., 2018). (d) Plate structure represented by a bi-material isotropic cubic+octet plate-lattice. Reproduced with permission from Springer Nature (Hsieh et al., 2021).

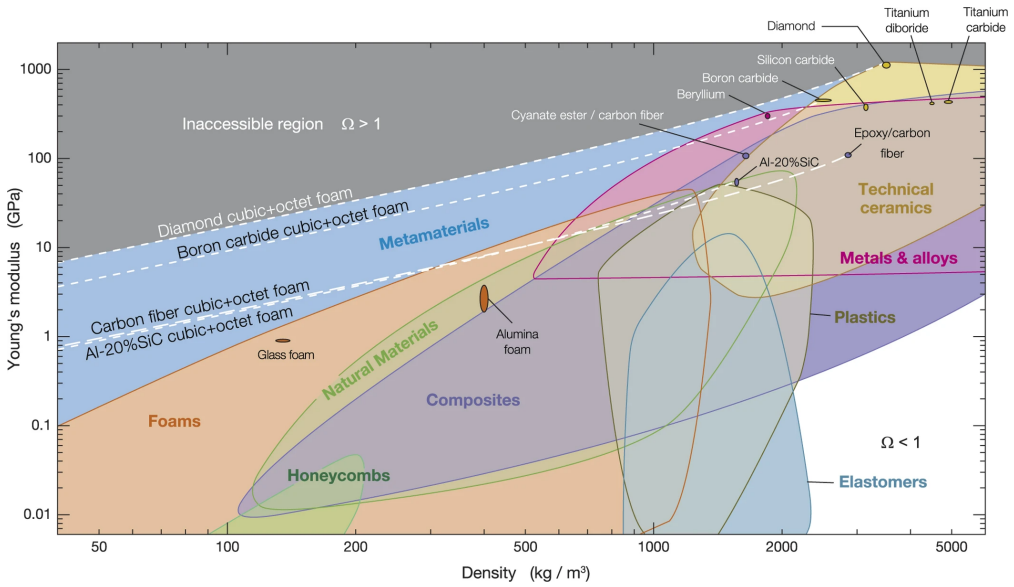


Figure 2.4.: Young's modulus - density Ashby charge for isotropic and nearly isotropic materials. The theoretical limit for mechanical metamaterials is derived from the Hashin–Shtrikman upper bound. Reproduced with permission from Springer Nature (Berger et al., 2017)

(Yan et al., 2024) have been reported in the literature. When Young's modulus–density relationship is represented on an Ashby chart (see Figure 2.4), the theoretical modulus of mechanical metamaterials exceeds that of conventional materials, particularly in the low-density regime. Furthermore, torsional couplings are achieved for Chiral metamaterials (Lin et al., 2021), negative Poisson's ratios are achieved for auxetic metamaterials, and vanishing shear modulus are achieved for pentamode metamaterials (Wu et al., 2021). Overall, the design possibilities of mechanical metamaterials are extensive, and only a brief overview is provided here.

The present work focuses on mechanical metamaterials in the form of two-dimensional lattice structures (see Figure 2.3 (b)). Such structures are defined by placing lattices in a repeating arrangement represented by the corresponding unit cell. The size of the lattice material is characterized by the length $l$ and thickness $t$ of the individual lattices. While the relative density $\tilde{\rho} = \rho/\rho_s$ is the ratio between the density of the mechanical metamaterials $\rho$ and the density of the solid base material $\rho_s$ from which the lattices are constructed. In this work, the subscript $s$ refers to the material property of the solid base material.

The material properties of mechanical metamaterials are directly linked to the structural behavior of the lattices. In general, the materials are separated into two overall groups, stretching and bending-dominated lattices. For the stretching-dominated structures,

the individual lattices are loaded in either tension or compression, while the bending-dominated lattices are loaded in pure bending. For a structure to be stretching-dominated, the necessary condition by Maxwell (1864) must be satisfied. In two and three dimensions, the conditions are given by, respectively

$$b \geq 2j - 3 \quad (2D), \tag{2.6}$$
$$b \geq 3j - 6 \quad (3D), \tag{2.7}$$

where $b$ is the number of lattices and $j$ is the number of joints. Calladine (1978) generalized those rules by

$$b - 2j + 3 = s - m \quad (2D), \tag{2.8}$$
$$b - 3j + 6 = s - m \quad (3D), \tag{2.9}$$

where $s$ is the number of self-stresses and $m$ is the number of mechanisms. The number of self-stress modes corresponds to the degree of structural redundancy that allows the structure to remain stable, while mechanism modes describe an under-constrained system that permits motion without resistance, assuming that the joints allow for free rotation. For lattice structures, the average node connectivity $Z$ represents the average number of lattices connected to a node, which can be used to estimate the number of lattices $b \approx jZ/2$ for Eq. (2.6) to (2.9). For periodic frameworks where the nodes are all similarly situated[1], having a node connectivity of $Z = 6$ in 2D and $Z = 12$ in 3D is a necessary and sufficient condition for the lattice structure to be stretching-dominated (Deshpande et al., 2001).

Mechanical properties of lattice structures can be expressed as a power law between the property and either the relative density ($\tilde{\rho}$) or the aspect ratio of the lattices ($t/l$). For low aspect ratios ($t/l < 0.2$) the relative densities $\tilde{\rho} \propto (t/l)$ in 2D or $(\rho/\rho_s) \propto (t/l)^2$ in 3D (Zhong et al., 2023). In the field of lightweight structures, the material modulus $E$ and material strength $\sigma_c$ are some of the key properties. In this work, $\sigma_c$ refers to the limit of the linear elastic area, e.g., yield strength for metals. The strength and modulus can, for low relative densities, be described by a power law relation

$$E = A \left( \frac{\rho}{\rho_s} \right)^a E_\mathrm{s}, \tag{2.10}$$
$$\sigma_\mathrm{c} = B \left( \frac{\rho}{\rho_s} \right)^b \sigma_\mathrm{s}, \tag{2.11}$$

where the constants $A$ and $B$ are determined by the topology, and the constants $a$ and $b$ are determined by the stretching-dominated or bending-dominated structural behavior, as specified in Table 2.2. The properties from the base materials $E_\mathrm{s}$ and $\sigma_\mathrm{s}$ are the

[1]The nodes are similarly situated if the rest of the framework appears the same and in the same orientation when viewed from any node (Deshpande et al., 2001).

Table 2.2.: Constants for material properties power low relations (Gibson and Ashby, 1997; Wang and McDowell, 2004; Lu et al., 2022)

| | **Stretching-dominated** | | **Bending-dominated** | |
|---|---|---|---|---|
| | **2D** | **3D** | **2D** | **3D** |
| a | 1 | 1 | 3 | 2 |
| b | 1 | 1 | 2 | 1.5 |
| c | 3 | 2 | 3 | 2 |

modulus and critical material strength, respectively. Considering the porosity of the lattice structure and assuming slender lattice elements, the lattice structure is prone to buckling failure under compression loading. The critical strength under the assumption of Euler buckling is given by

$$\sigma_{\mathrm{E}} = C \left( \frac{\rho}{\rho_s} \right)^c E_{\mathrm{s}} \tag{2.12}$$

where $C$ depends of the topology and $c$ depends on the structural behavior and is specified in Table 2.2.

## 2.3. Mechanical behavior of materials and structures

This section establishes the theoretical foundations for analyzing the mechanical behavior of materials and structures under the assumption of linear elasticity. It serves as a basis for the understanding of continuum materials and structural elements. The section ends with a short introduction to relevant energy methods. For further details, the reader is referred to standard textbooks such as (Hjelmstad, 2005; Sadd, 2021).

### 2.3.1. Linear elasticity theory

The theory of linear elasticity describes the relationship between stresses, strains, and deformations in solid bodies under the assumptions of linear elastic material behavior and small deformations. The formulations presented here provide the theoretical foundation for the subsequent development of linear beam theory.

Consider a solid body $\mathcal{B}$ undergoing a deformation as shown in Figure 2.5. The subscript 0 refers to the reference configuration, where the state after transformation is referred to as the deformed configuration. The position of a point $\mathcal{P}$ is described by the position vector $\boldsymbol{r} = x\mathbf{e}_1 + y\mathbf{e}_2 + z\mathbf{e}_3$ where where the vector base $\{\mathbf{e}_1,\ \mathbf{e}_2,\ \mathbf{e}_3\}$ is the unit vectors in the $x$, $y$ and $z$ direction respectively. By the transformation of the body, the point $\mathcal{P}$

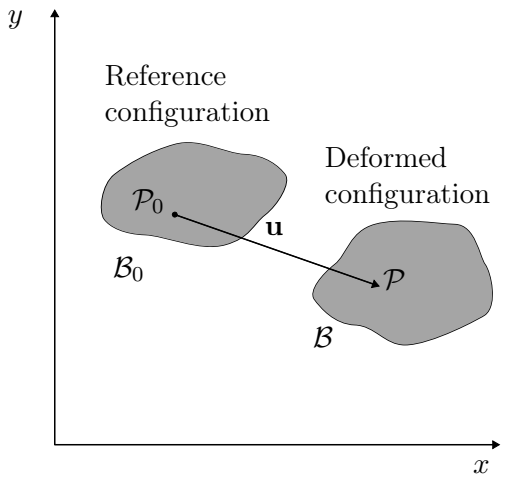


Figure 2.5.: Deformation of a body $\mathcal{B}$.

will undergo a displacement of

$$\boldsymbol{u} = \boldsymbol{r} - \boldsymbol{r}_0,$$

where the components are denoted as $u_i = \{u,v,w\}$. From the assumption of small deformations, the symmetric linearized strain tensor $\boldsymbol{\varepsilon}$ is considered, with the components

$$\varepsilon_{ij} = \frac{1}{2}\left(u_{i,j} + u_{j,i}\right), \tag{2.13}$$

where the components are denoted as

$$\boldsymbol{\varepsilon} = \begin{bmatrix} \varepsilon_{xx} & \varepsilon_{xy} & \varepsilon_{xz} \\ \varepsilon_{yx} & \varepsilon_{yy} & \varepsilon_{yz} \\ \varepsilon_{zx} & \varepsilon_{zy} & \varepsilon_{zz} \end{bmatrix}. \tag{2.14}$$

The compatibility relations ensure a continuous single-valued displacement field. The compatibility equations are given by

$$\varepsilon_{ij,kl} + \varepsilon_{kl,ij} - \varepsilon_{ik,jl} - \varepsilon_{jl,ik} = 0 \tag{2.15}$$

resulting in six relevant equations.

Exposing an elastic body to an external loading, either by surface forces or body forces, the body will deform. To evaluate the deformation of the body, the external load is first transformed into the corresponding stress field of the body. For an area $\Delta A$ on a section of the body with an outward normal vector $\boldsymbol{n}$ and the force $\Delta \boldsymbol{f}$ acting on the surface,

the traction vector is defined by

$$\boldsymbol{t} = \lim_{\Delta A \to 0} \frac{\Delta \boldsymbol{f}}{\Delta A}. \tag{2.16}$$

The Cauchy stress tensor $\boldsymbol{\sigma}$ is the uniquely defined tensor that transforms the normal vector to the traction for a chosen point.

$$t_i = \sigma_{ij} n_j. \tag{2.17}$$

It is a symmetric stress tensor describing the normal and shear stresses. The components are denoted as

$$\boldsymbol{\sigma} = \begin{bmatrix} \sigma_{xx} & \sigma_{xy} & \sigma_{xz} \\ \sigma_{yx} & \sigma_{yy} & \sigma_{yz} \\ \sigma_{zx} & \sigma_{zy} & \sigma_{zz} \end{bmatrix}. \tag{2.18}$$

The equilibrium equations for a static equilibrium state that

$$\sigma_{ij,j} + b_i = 0, \tag{2.19}$$

where $\boldsymbol{b}$ is the vector of the body forces.

The relation between the stress and strains is connected by the constitutive relation. Considering linear elastic materials, the constitutive equation is given by Hooke's law

$$\boldsymbol{\sigma} = \mathbb{C} : \boldsymbol{\varepsilon} \tag{2.20}$$

where $\mathbb{C}$ is the fourth order elasticity tensor. For an anisotropic material, the elasticity tensor has 21 independent components.

For isotropic materials, Eq. (2.20) is reduced to the generalized Hooke's law for linear isotropic elastic solids

$$\sigma_{ij} = \lambda \varepsilon_{kk} \delta_{ij} + 2G\varepsilon_{ij} \tag{2.21}$$

where $\delta_{ij}$ is the Kronecker delta, $\lambda$ is Lamé's first parameter and $G$ is the shear modulus of rigidity. The components $\lambda$ and $G$ can be related to Young's modulus $E$ and Poisson's ratio $\nu$ by the following expressions

$$\lambda = \frac{E\nu}{(1+\nu)(1-2\nu)} \quad \text{and} \quad G = \frac{E}{2(1+\nu)}. \tag{2.22}$$

### 2.3.2. Linear theory of beams

Reducing the three-dimensional continuum mechanics to either two-dimensional (plate or shell) or one-dimensional (beam) theory is a powerful method to simplify problems,

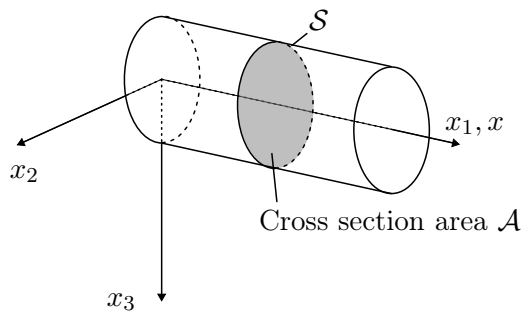


Figure 2.6.: Beam in 3D positioned so the longitudinal axis is coincident with the $x$-axis. $\mathcal{A}$ refers to the cross-sectional area where $\mathcal{S}$ is the outer boundary.

enabling closed-form solutions of some structural problems or reducing the degrees of freedom in numerical methods such as finite element simulations. Satisfying the assumptions for those theories, the reduction of dimensions only leads to small or insignificant errors. The governing equations for such one-dimensional beams are presented in this section based on the two well-known theories *Euler Bernoulli beam theory* and *Timoshenko beam theory*. (Hjelmstad, 2005)

Consider a beam, a long, slender body, placed in a three-dimensional coordinate system as shown in Figure 2.6. The beam is positioned with the longitudinal axis coincident with the $x_1$-axis, here also defined as $x \equiv x_1$. The distributed load $\boldsymbol{q}(x)$ is given by

$$\boldsymbol{q}(x) = \int_{\mathcal{A}} \boldsymbol{b} \, \mathrm{d}A + \int_{\mathcal{S}} \boldsymbol{t}_{\mathcal{S}} \, \mathrm{d}s \tag{2.23}$$

Where $\boldsymbol{b}$ is the body forces, and $\boldsymbol{t}_{\mathcal{S}}$ is the surface forces. To convert the three-dimensional equilibrium equations into one dimension, the traction force on the beam cross-section must be represented by the one-dimensional stress resultants. The resultant force $Q(x)$ and moment $M(x)$ are given by the following integrals over the cross-sectional area $\mathcal{A}$

$$\boldsymbol{Q}(x) \equiv \int_{\mathcal{A}} \boldsymbol{t}_{\mathbf{e_1}} \mathrm{d}A \tag{2.24}$$

$$\boldsymbol{M}(x) \equiv \int_{\mathcal{A}} \boldsymbol{p} \times \boldsymbol{t}_{\mathbf{e_1}} \mathrm{d}A \tag{2.25}$$

where $\boldsymbol{t}_{\mathbf{e_1}}$ is the traction vector acting on a plane with the unit vector $\mathbf{e_1}$ and the position vector $\boldsymbol{p} = x_2\mathbf{e_2} + x_3\mathbf{e_3}$.

The equilibrium equations for the stress resultants are given by

$$\boldsymbol{Q}' + \boldsymbol{q} = 0, \tag{2.26}$$
$$\boldsymbol{M}' + \mathbf{e}_1 \times \boldsymbol{Q} = 0. \tag{2.27}$$

#### 2.3.2.1. The kinematic hypothesis

While the beam is treated as a one-dimensional element, the deformation of the beam is not limited to this dimension. The kinematic hypothesis states that a plane cross-section of the beam remains plane after the deformation. Additionally, it is assumed the plane does not distort in its own plane. For small deformations, the deflection can be expressed as

$$\boldsymbol{u}(\boldsymbol{x}) = \boldsymbol{w}(x) + \boldsymbol{\phi}(x) \times \boldsymbol{p}(x_1,x_2) \tag{2.28}$$

where $\boldsymbol{w}$ is the displacement of the origin of the cross-section plane and $\boldsymbol{\phi}$ is the rotation vector of the cross-section.

#### 2.3.2.2. Timoshenko beam theory

The analysis of the beam is simplified further by considering it as a planar problem (see Figure 2.7). The $x$-axis of the coordinate system is placed at the neutral axis of the beam, and symmetry is assumed for the $x$-$z$ plane. The loading is applied in the plane of symmetry such that no out-of-plane motion occurs, so

$$v(x,z) \equiv u_2 = 0. \tag{2.29}$$

The in-plane deformation is given by (see Eq. (2.28)):

$$u(x,z) \equiv u_1 = u_0 + \phi z, \tag{2.30}$$
$$w(x,z) \equiv u_3 = w_0, \tag{2.31}$$

where $u_0$ is the extension due to tension loading, $w_0$ is the displacement of the neutral axis in the $z$-direction, and $\phi = \phi_2$ is the rotation of the cross-section. The in-plane stress resultants from Eq. (2.24) and (2.25) are defined as

$$N \equiv Q_1 = EAu', \tag{2.32}$$
$$Q \equiv Q_3 = \kappa GA(w' + \phi), \tag{2.33}$$
$$M \equiv M_2 = EI\phi', \tag{2.34}$$

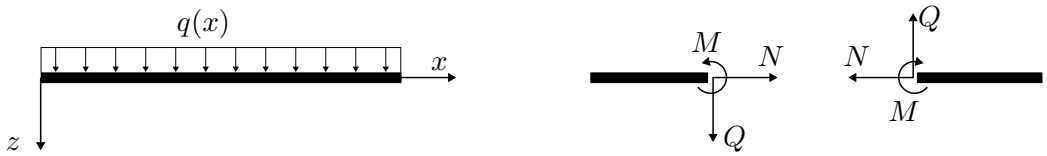


(a) External loading (b) Section forces.

Figure 2.7.: Planar beam.

where $E$ is Young's modulus, $G$ is the shear modulus, $\kappa$ is the shear correction factor, $A$ is the size of the cross-section area, and $I$ is the second moment of area about the neutral axis. From Eq. (2.26) and (2.27) the equilibrium equations are precedence by

$$Q' + q = 0, \tag{2.35}$$
$$N' + n = 0, \tag{2.36}$$
$$M' - Q = 0, \tag{2.37}$$

where $n(x)$ is the axial loading and $q(x)$ is the transverse loading. The equation system of Eq. (2.35) to (2.37) identifies the bending and shear components as a coupled system, uncoupled from the axial components. The governing equations for the shear and bending equations can be written as a fourth-order coupled system

$$-EI\phi'' + \kappa GA(w' + \phi) = 0, \tag{2.38}$$
$$\kappa GA(w' + \phi)' = -q. \tag{2.39}$$

Solving the system for the deformation and rotation, four integration constants are required, which are determined by the boundary conditions.

#### 2.3.2.3. Euler Bernoulli beam theory

The Euler-Bernoulli beam theory expands the assumptions from the Timoshenko beam theory (see section 2.3.2.2), including the kinematic assumptions stating that a planar cross-section remains planar after deformation with no distortion (see section 2.3.2.1), and the assumption of a planar problem (see Figure 2.7), with an additional assumption: normal to the neutral axis remains normal during the deformation. This assumption relates the beam deflection and rotation by the relation

$$w' = -\phi \tag{2.40}$$

neglecting the shear deformation of the beam. The equilibrium equations from Eq. (2.35) to (2.37) remains unchanged, while the stress resultants of Eq. (2.32) to (2.34) are reduced

to

$$N = EAu', \tag{2.41}$$
$$M = -EIw''. \tag{2.42}$$

The governing ordinary differential equation (ODE) for the Euler-Bernoulli beam theory is given by

$$(EIw'')'' = -q. \tag{2.43}$$

### 2.3.3. Energy methods

This section introduces energy-based formulations used throughout this work. The concepts of total potential energy, the principle of minimum potential energy, the principle of virtual work, and the Rayleigh-Ritz method are briefly reviewed.

In this work, the total potential energy $\Pi$ consists of contributions from the elastic strain energy $U$ and the work done by external forces $W_E$, such that

$$\Pi = U - W_E. \tag{2.44}$$

The elastic strain energy stored in a body $\mathcal{B}$ occupying the volume $V$ is given by

$$U = \frac{1}{2}\int_V \sigma_{ij}\varepsilon_{ij}\mathrm{d}V. \tag{2.45}$$

In the special case of a beam, the strain energy can be expressed as

$$U = \frac{1}{2}\int_l \frac{M^2}{EI} + \frac{1}{2}\int_l \frac{Q^2}{\kappa GA}\mathrm{d}x + \frac{1}{2}\int_l \frac{N^2}{EA}\mathrm{d}x. \tag{2.46}$$

According to the principle of minimum potential energy, among all kinematically admissible configurations that satisfy the boundary conditions, the configuration that minimizes the total potential energy corresponds to a state of stable equilibrium. The variation of the potential energy functional at equilibrium can be stated using the directional derivative

$$\delta\Pi = \frac{\partial\Pi}{\partial g_i}\delta g_i = 0 \tag{2.47}$$

for all degrees of freedom. Leaving out the trivial solution, then

$$\frac{\partial\Pi}{\partial g_i} = 0. \tag{2.48}$$

When satisfying this relation, the system is in static equilibrium.

#### 2.3.3.1. The principle of virtual work

The virtual displacement is a fictitious, infinitesimal displacement. A virtual displacement, $\delta u_i$, that satisfies the kinematic boundary conditions is introduced. The corresponding work performed by the external forces, referred to as the virtual work, is given by

$$\delta W_E = \int_S t_i \delta u_i \mathrm{d}S + \int_V b_i \delta u_i \mathrm{d}V, \tag{2.49}$$

where $\boldsymbol{t}$ is the traction forces working on the outer surface $S$, and $\boldsymbol{b}$ are the the body forces. For a system in static equilibrium, the principle of minimum potential energy implies that the total virtual work is zero. To obtain the elastic strain energy introduced by the virtual displacement, the virtual version of the strain is identified

$$\delta\varepsilon_{ij} = \frac{1}{2}(\delta u_{i,j} + \delta u_{j,i}). \tag{2.50}$$

From the principle of minimum potential energy $\delta\Pi = \delta U_E - \delta W_E = 0$. Inserting Eq. (2.50), (2.45) and (2.49) the following relation is obtained

$$\int_V \sigma_{ij}\delta\varepsilon_{ij}\mathrm{d}V = \int_S t_i \delta u_i \mathrm{d}S + \int_V b_i \delta u_i \mathrm{d}V \tag{2.51}$$

which is also stated as the principle of virtual work.

#### 2.3.3.2. Rayleigh-Ritz method

The Rayleigh–Ritz method provides an approximate technique for determining the deflection and stability of structures by minimizing the total potential energy of the system. A trial functions that satisfies the kinematic boundary conditions is chosen for each displacement component:

$$u(x) = \sum_{n=1}^{N} a_n u_n(x), \quad v(x) = \sum_{n=1}^{N} b_n v_n(x), \quad w(x) = \sum_{n=1}^{N} c_n w_n(x), \tag{2.52}$$

where $u_n(x)$, $v_n(x)$, $w_n(x)$ are selected basis functions (e.g., polynomials or trigonometric functions), and $a_n$, $b_n$, $c_n$ are unknown coefficients. Substitution of the assumed displacement fields into the total potential energy functional renders $\Pi$ a function of the unknown coefficients, $\Pi = \Pi(a_n, b_n, c_n)$. The equilibrium configuration is obtained by minimizing the potential energy (see Eq. (2.48)) with respect to the unknown coefficients, leading to the following system of algebraic equations:

$$\frac{\partial\Pi}{\partial a_n} = 0, \quad \frac{\partial\Pi}{\partial b_n} = 0, \quad \frac{\partial\Pi}{\partial c_n} = 0. \tag{2.53}$$

Solving the resulting finite set of algebraic equations yields an approximate continuous displacement field, from which the corresponding strains and stresses can be evaluated. The accuracy of the solution depends on both the choice and the number of trial functions employed. For beam problems, satisfactory results are often obtained using only one or two components.

## 2.4. Stability of elastic structures

Mechanical metamaterials in the form of lattice structures are prone to buckling due to their slender elements. Therefore, a fundamental understanding of the structural stability of lattice elements is required to analyze damage and failure of such mechanical metamaterials. The classical Euler buckling theory is presented for the analysis of buckling in a perfect structure. However, given the inevitable imperfection of physical structures, the introduction of imperfections is necessary for conducting more precise analyses.

### 2.4.1. Classical Euler buckling

The first-order beam theory presented in Section 2.3.2, assumes that the effect of deformations does not affect the actions of the load, for which the stresses and displacement is proportional to the applied load. Slender columns under compression loading are known to buckle, creating a sudden lateral deflection that reduces the stiffness of the element significantly (Timoshenko and Gere, 1961; Bažant and Cedolin, 2010). Evaluating a perfect column subjected to an axial compression load $P$ the system is initially in equilibrium. When the load is increased to a critical load the system reaches a bifurcation point and becomes unstable. Any small disturbance to the unstable perfect system will cause the beam to deflect. Introducing the second order term $Pw$ to Eq. (2.42) and assuming a constant bending rigidity $EI$ and the length $L$, the governing ODE is given by

$$w^{IV} + \mu w'' = 0 \tag{2.54}$$

where $\mu^2 = \frac{P}{EI}$. The general solution

$$w = c_1 \sin(\mu x) + c_2 \cos(\mu x) + c_3 x + c_4 \tag{2.55}$$

where $c_1 - c_4$ are arbitrary constants that can be determined by the boundary conditions. This is an eigenvalue problem for which the buckling shape and critical loading can be determined when evaluating the non-zero solution.

Considering the case of a column pinned at both ends, the boundary condition is $w(0) = w(L)$ and $M(0) = M(L) = 0$, where the moment $M = -EIw''$. The corresponding

buckling shape

$$w = A \sin\left(\frac{m\pi x}{L}\right) \quad \text{for} \quad m = 1,2,3,... \tag{2.56}$$

here $m$ refers to the eigenmode and the amplitude $A$ is arbitrary constant. For a column clamped at both ends ($w(0) = w(L)$ and $w'(0) = w'(L) = 0$), the buckling shape is given by

$$w = A \cos\left(\frac{m\pi x}{L}\right) \quad \text{for} \quad m = 1,2,3,... \tag{2.57}$$

The eigenvalue corresponds to the critical force for which buckling is introduced, and is given by

$$P_{cr} = \frac{m^2\pi^2 EI}{(nL)^2} \quad \text{for} \quad m = 1,2,3,... \tag{2.58}$$

where $n$ is a constant determined by the boundary conditions. For a column pinned at both ends $n = 1$ while for a column fixed at both ends $n = 0.5$.

### 2.4.2. Imperfections

Real-world structures inevitably deviate from idealized configurations due to manufacturing tolerances, material heterogeneity, misaligned loading, etc. The introduction of imperfections transforms the Euler buckling eigenvalue problem into a nonlinear deformation problem, where any axial load immediately induces transverse displacements, reducing the load-bearing capacity of the column (Timoshenko and Gere, 1961; Budiansky, 1974). Good representations of the imperfections are essential, as a poor choice can lead to unrealistic results and significant overestimation of the load-bearing capacity (Klasson et al., 2016).

For geometrical imperfections, the assumption of an idealized column is relaxed, and the column is given an initial non-straight geometry. For analytical convenience, the shape of the first buckling mode is often used (Chan and Gu, 2000; Cai et al., 2019; Ren et al., 2022). But also higher buckling modes, local imperfections, and transverse displacement of the boundaries are considered for geometrical imperfections (Girão Coelho et al., 2013; Klasson et al., 2016; Harvey et al., 2019). Multiple studies evaluate the buckling of pre-stressed stayed columns, including imperfections defined from the first and second mode buckling shapes (Smith, 1985; Chan et al., 2002; Wu et al., 2022). Imperfections can also come from a misalignment of the compression load. By load eccentricity, the initial displacement of the compression load results in a moment at the column boundary (Chan and Gu, 2000; Quek et al., 2006; Mazzilli, 2009; Nie et al., 2017). Harvey and Cain (2020) developed an analytical method to determine the dominant imperfection type, considering a combination of geometric imperfection in the shape of the first eigenmode with the amplitude $a$ and the load eccentricity $e$. The load deflection relations for different imperfection ratios are depicted in Figure 2.8. In the special case of an imperfection ratio of $e/a = -\pi/4$ the imperfections are neutralized, and the response corresponds to

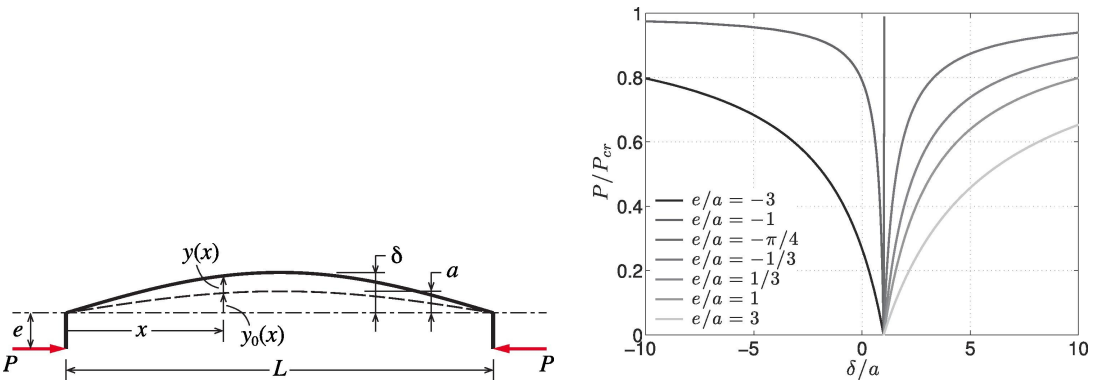


(a) Schematic representation of the column.

(b) Load deflection relations.

Figure 2.8.: Load deflection response of a column with both a geometrical sinus imperfection with the amplitude $a$, and a load eccentricity imperfection of $e$ working in opposite direction. In the special case of $e/a = -\pi/4$ the total imperfection is neutralized. Reprinted from (Harvey and Cain, 2020), with permission from Elsevier.

the classical Euler buckling. Sampaio and Hundhausen (1998) used an initial slope for self-buckling of a column, introducing a small angle the the gravitational load of the column. This consideration of imperfection is later used by Kanahama and Sato (2024) for self-buckling of trees, where imperfections consist of a combination of initial transverse deflection and an initial slope of the geometry.

The maximal load-bearing capacity (Eq. (2.58)) is proportional to the second moment of area of the column. Therefore, profiles, such as the I-profile (Papp, 2016; Yang et al., 2023) and box-section columns (Nie et al., 2017; Radwan and Kövesdi, 2024), become of particular interest due to their high second moment of area in relation to the cross-sectional area. The plate-like nature of these profiles introduces additional complexity to the buckling modes by combining the local buckling of the plates with the global buckling of the column. This behavior also expands the possible geometric imperfection patterns. By the use of optimization Kristanič and Korelc (2008) and Lindgaard et al. (2010) studied the most critical geometric imperfection shapes and imperfection combinations for column cross-section.

### 2.4.3. Buckling of lattice structures

Mechanical metamaterials in the form of lattice structures consist of a network of connected slender elements, where localized compression can lead to buckling failure of the structure (Li et al., 2022). For such structures, buckling can occur both as local buckling of the individual lattices or as global buckling of the structure. The lattice slenderness

is directly linked to the relative density, where low-density lattices are more prone to buckle. Increasing the density, while keeping the lattice length constant (increasing lattice thickness), improves the buckling resistance (see Eq. (2.58)) together with the corresponding load-bearing capacity until the strength failure mode (e.g. yield failure) becomes the critical failure mode (Wang and McDowell, 2004). The buckling strength of low-density lattices is described by the power law relation of Eq. (2.12). Multiple analyses have been performed to evaluate the specific buckling load or periodic lattices using classical beam-column theory (Anderson, 1981; Fan et al., 2009; Haghpanah et al., 2014). Different methods have been considered to increase the critical buckling load of lattice structures, such as introducing fiber reinforcement of the lattice material (Zschernack et al., 2016), altering the cross-section shape of the lattices (Viswanath et al., 2023), using topology optimization for designing the unit cells (Maurizi et al., 2022; Thomsen et al., 2018) or introducing variations to the cross-section area of the lattice by use of machine learning (Lee et al., 2024). For a more stable buckling process, Rosa et al. (2025) proposed the use of a icosahedral quasicrystal dual lattice structure, leading to a more localized damage of the lattices.

In the special case of diamond and cubic lattice structures, the behavior of the material (stretching-dominated or bending-dominated) is determined by the orientation of the lattice in relation to the loading. Zhao et al. (2025) performed an experimental study showing that when a cubic-shaped unit cell is rotated from diamond lattice orientation of 45° (see Figure 2.9a) to cubic lattice orientation of 90° (see Figure 2.9b), the material behavior changes from bending-dominated to stretching-dominated. Both the elastic modulus and strength showed strong angle dependence with maximum values at a rotation of 75°, marking the transition point between bending-dominated and buckling-dominated failure. The transformation between bending and buckling-dominated failure is characterized by going from a more ductile to a brittle failure response, where the response of the stress-strain relation changes from a flat plateau to a sudden load drop (see Figure 2.9c).

For comparison of lattice structures to other materials, not only the strength but also the fracture toughness is needed. In a study by Shenhav and Sherman (2019), they showed that the fracture toughness of stretching-dominated lattice material under local compression is not a material property determined by the base material, but is instead controlled by the resistance to lattice buckling. This is also observed by Shaikeea et al. (2022), who also determines the ratio between the unit cell size and the crack length as a parameter that affects the fracture toughness.

As for column buckling, imperfections can affect the load-bearing capacity of the lattice structures. The imperfections vary strongly with the manufacturing process and include misplaced nodes, cell wall waviness, inclusions, material defects, missing cell edges, nonuniform wall thickness, cell-size variation, strut thickness variation, etc. (Pasini and Guest, 2019). As the column buckles, the imperfections are often implemented as

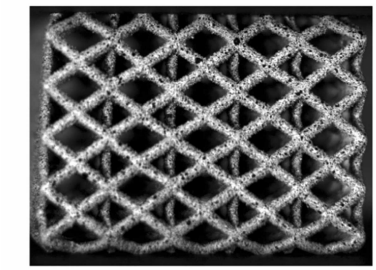

(a) Diamond lattice (orientation 45°)

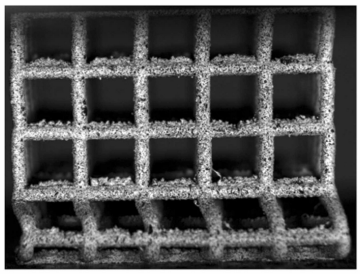

(b) Cubic lattice (orientation 90°)

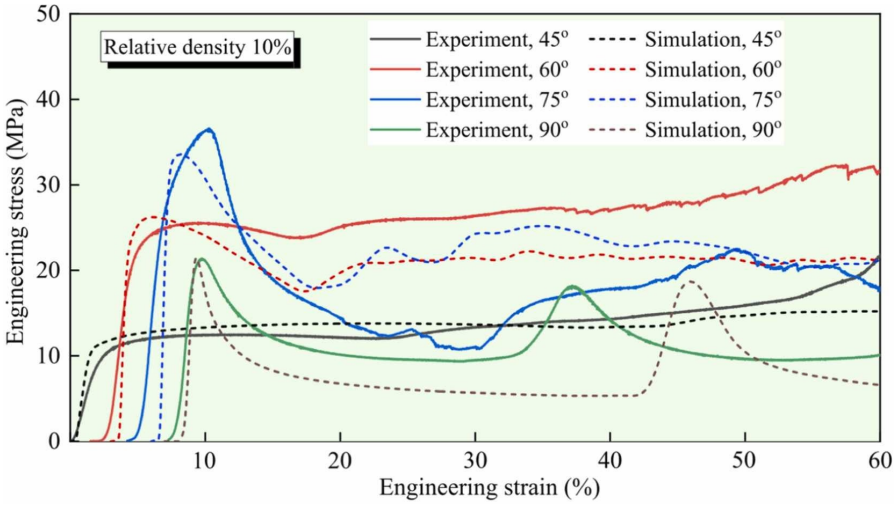


(c) Stress strain relation

Figure 2.9.: Changing the lattice structure orientation from cubic (90°) to diamond (45°) transforms the structural failure mode from a bending response to a buckling response. Reprinted from (Zhao et al., 2025), with permission from Elsevier.

geometrical imperfections represented by the buckling modes of the structure (Parente et al., 2025). Jamshidian et al. (2020) found that the effect of the imperfection converges when including the first 36 buckling modes. Also, errors in the joint coordinates and member misfit (Peek and Triantafyllidis, 1992), plateau borders and wavy cell walls (Zhang et al., 2023) and cutout imperfections (Wang and Xiong, 2025) are studied in literature.

While buckling of lattice materials is in many cases considered a critical failure mode, it is actively used for other applications. The bifurcation introduced at the buckling of elastic materials results in a multi-stable structure. This is a desired feature, e.g., in shock absorbers and dampers, and soft robotics (Vangelatos et al., 2019; Yang and Ma, 2019; Janbaz et al., 2019).

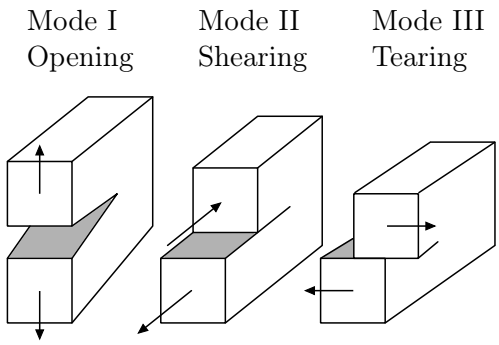


Figure 2.10.: Loading mode I, II and III

## 2.5. Fracture mechanics

To understand the failure process within a material, evaluating local stress values and comparing them to strength-based criteria alone is insufficient. When stress gradients are present, the energy dissipation for the damage formation must also be considered. In the fundamental case of crack propagation in brittle materials, the damage process is governed by energy dissipation. The theory of linear elastic fracture mechanics (LEFM) provides a theoretical framework for describing such energy-driven fracture processes. In this section, the fundamentals of the linear LEFM are established. Further information can be found in standard textbooks such as (Anderson, 2017).

### 2.5.1. Linear elastic fracture mechanics

Considering a material with an infinitely sharp crack, an arbitrary loading will result in a stress singularity at the crack tip. The loading is separated into three modes, opening (mode I), shearing (mode II), and tearing (mode III) as depicted in Figure 2.10. The LEFM takes its onset in the assumption of linear elastic materials and a small process zone at the crack tip. Placing a polar coordinate system ($r$,$\theta$) with the origin at the crack tip, as shown in Figure 2.11, the stress tensor can be given by

$$\sigma_{ij} = \left(\frac{K}{\sqrt{2\pi r}}\right) f_{ij}(\theta) + \sum_{m=0}^{\infty} A_m r^{\frac{m}{2}} g_{ij}(\theta) \tag{2.59}$$

where $K$ is the stress intensity factor and $f_{ij}$ is a dimensionless function of $\theta$, both dependent on the loading mode. For the higher order terms, $A_m$ represents an amplitude and $g_{ij}$ a dimensionless function of $\theta$, both depend on the geometry. In the limit where

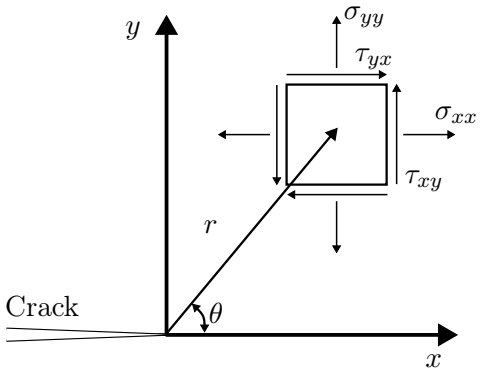


Figure 2.11.: Schematic representation of the stress orientation with respect to the crack tip. Adopted from (Anderson, 2017).

$r \to 0$, the leading term results in a square root singularity, and in the area close to the crack tip, the stresses will decrease with $1/\sqrt{r}$. When loading the structure in pure mode I, II, or III (see Figure 2.10), the stress fields in the vicinity of the crack tip can be described by

$$\begin{aligned}
\lim_{r\to 0} \sigma_{ij}^{(I)} &= \frac{K_I}{\sqrt{2\pi r}} f_{ij}^{(I)}(\theta), \\
\lim_{r\to 0} \sigma_{ij}^{(II)} &= \frac{K_{II}}{\sqrt{2\pi r}} f_{ij}^{(II)}(\theta), \\
\lim_{r\to 0} \sigma_{ij}^{(III)} &= \frac{K_{III}}{\sqrt{2\pi r}} f_{ij}^{(III)}(\theta).
\end{aligned} \tag{2.60}$$

The stress intensity factor takes the form of

$$K_{(I,II,III)} = Y\sigma\sqrt{\pi a} \tag{2.61}$$

where $\sigma$ is the characteristic stress, $a$ is the characteristic crack length, and $Y$ is a dimensionless constant dependent on the geometry and mode of loading. In the classical case of an infinitely large plate with a center crack $Y = 1$. The material resistance to fracture is determined by the material fracture toughness $K_{I_c}$, such that the crack will start to propagate when the stress intensity factor reaches the fracture toughness

$$K_I = K_{\mathrm{Ic}}. \tag{2.62}$$

The Westergaard stress function provides an alternative method to describe the stress field. Introducing the complex function $Z(z)$ where $z = x + iy$, the stress field can be

described by

$$\sigma_{\mathrm{xx}} = \mathrm{Re}Z - y\mathrm{Im}Z', \tag{2.63}$$
$$\sigma_{\mathrm{yy}} = \mathrm{Re}Z + y\mathrm{Im}Z', \tag{2.64}$$
$$\tau_{\mathrm{xy}} = -y\mathrm{Re}Z' \tag{2.65}$$

where Re and Im refer to the real and imaginary parts of the function, respectively. In the special case of an infinite plate with a crack under mode I loading, and assuming the origin of the coordinate system is positioned in the center of the crack, the stress function is given by (Westergaard, 1939)

$$Z = \frac{\sigma}{\sqrt{1 - \frac{a^2}{z^2}}}. \tag{2.66}$$

Analyzing the stress field in the crack plane ($y = 0$), the stresses in the opening direction are given by

$$\sigma_{yy} = \sigma \frac{|x|}{\sqrt{x^2 - a^2}}, \quad |x| < a. \tag{2.67}$$

In the vicinity of the crack tip at the position $x = a + x^*$, where $x^* << a$ describes the distance to the crack tip, the stress field is given by

$$\sigma_{yy} = \frac{K_{\mathrm{I}}}{\sqrt{2\pi x^*}}. \tag{2.68}$$

The same relation between the stress and stress intensity factor in the vicinity of the crack tip is shown by Eq. (2.60).

The fracture process can also be considered from an energy perspective. For an incremental increase in the size of the crack area, $\mathrm{d}A$, Griffith's energy balance states

$$\frac{\mathrm{d}\Pi}{\mathrm{d}A} + \frac{\mathrm{d}\Gamma}{\mathrm{d}A} = 0 \tag{2.69}$$

where $\Pi$ is the potential energy of the system and $\Gamma$ is the work required to create the new surfaces. The term describing the change of the potential energy due to the crack growth $\mathrm{d}A$ is defined as the energy release rate (ERR)

$$\mathcal{G} = -\frac{\mathrm{d}\Pi}{\mathrm{d}A}, \tag{2.70}$$

while the critical limit is defined as the material's fracture toughness

$$\mathcal{G}_{\mathrm{c}} = \frac{\mathrm{d}\Gamma}{\mathrm{d}A}. \tag{2.71}$$

Please note that both the terms of $K_{Ic}$, $K_{IIc}$, $K_{IIc}$, and $G_{\mathrm{c}}$ are all referred to as the material fracture toughness, describing the material's resistance to fracture. However, the

unit between the stress intensity and energy release rate and their critical values differ. The Griffin criterion for infinitesimal growth is given by

$$\mathcal{G} = \mathcal{G}_{\mathrm{c}}. \tag{2.72}$$

For bulk materials, the stress intensity and the ERR are related by

$$\mathcal{G}_I = \frac{K_I^2}{E'}, \quad \mathcal{G}_{II} = \frac{K_{II}^2}{E'}, \quad \mathcal{G}_{III} = \frac{K_{III}^2}{2G} \tag{2.73}$$

where $E' = E$ for plane stress and $E' = E/(1-\nu)$ for plane strain where $E$ is Young's modulus of the materials $\nu$ is Poisson's ratio.

The LEFM is based on the assumption of a perfect elastic-brittle material behavior, letting the stress-strain relation remain linear until failure. However, in reality, the plasticity of the materials introduces a stress reduction to the stress fields, appearing as a plastic zone around the crack tip. For the LEFM to be valid, a small plastic zone in relation to the characteristic crack size is required. The first-order approximation of the plastic zone size under the assumption of plane stress can be estimated by

$$r_p = \frac{1}{2\pi}\left(\frac{K_{\mathrm{I}}}{\sigma_{\mathrm{ys}}}\right)^2, \tag{2.74}$$

where $\sigma_{\mathrm{ys}}$ is the yield strength of the material Anderson (2017).

### 2.5.2. Finite fracture mechanics

The theory of LEFM assumes the presence of an infinitely sharp crack, resulting in an inverse square-root singularity of the stress field next to the crack tip (see Eq. (2.60)). Altering the crack shape, for example, assuming a V-shaped notch or a U-shaped notch, or in the absence of a crack, the theory of LEFM breaks down. Under the assumption of an elastic-brittle material behavior, the theory of finite fracture mechanics (FFM) provides a method for analyzing the crack fracture process in such a situation by assuming a finite crack growth of the area $\Delta A$ (Hashin, 1996). A coupled stress and energy criterion provides two necessary conditions that must be fulfilled simultaneously, giving a sufficient condition for crack growth (Leguillon, 2002). The stress criterion states that stresses (e.g., principal stresses) for all points of the finite crack surface of the crack growth ($\mathcal{S}_{\Delta A}$) must exceed the material strength

$$f(\sigma_{ij}(x)) \geq \sigma_c \quad \forall x \in \mathcal{S}_{\Delta A}. \tag{2.75}$$

This formulation of the stress criterion is also referred to as the point method. The energy criterion is based on Griffith's energy criterion from Eq. (2.72), reformulated to

incorporate the finite size of the crack growth, and is given by

$$-\frac{\Delta\Pi(\Delta A)}{\Delta A} = \mathcal{G} \geq \mathcal{G}_{\mathrm{c}}. \tag{2.76}$$

By restricting the crack growth to 2D, the area of the finite crack growth can be formulated as $\Delta A = b\Delta a$ where $b$ is the width of the specimen and $\Delta a$ is the increase in the crack length due to the crack growth. The energy criterion can be given by

$$\frac{1}{\Delta a}\int_0^{\Delta a} \mathcal{G}(\bar{a})\mathrm{d}\bar{a} \geq \mathcal{G}_{\mathrm{c}}. \tag{2.77}$$

Alternatively, the energy criterion can be formulated by the stress intensity factor. Under the assumption of mode I loading, the energy criterion is given by

$$\frac{1}{\Delta a}\int_0^{\Delta a} K_{\mathrm{I}}(\bar{a})^2\mathrm{d}\bar{a} \geq K_{\mathrm{Ic}}. \tag{2.78}$$

As an alternative to the point method (Eq. (2.75)), the stress criterion can be formulated by the line method, considering the average stress of the crack surface before crack formation

$$\frac{1}{\Delta a}\int_0^{\Delta a} f(\sigma_{ij}(x))\mathrm{d}\bar{x} \geq \sigma_c. \tag{2.79}$$

#### 2.5.2.1. Plate with sharp crack

To highlight the relations between the LEFM and the FFM, a simple example from the work of Weißgraeber et al. (2016) is presented here. Consider the classical problem from LEFM of an infinitely large plate with a crack of length $2a$ under a mode I loading. To analyze this problem using the FFM, the stress in front of the crack tip is considered by Westergaard's stress function given by Eq. (2.67). Using the line method, the coupled criterion of Eq. (2.78) and (2.79) and the stress intensity factor from Eq. (2.61) results in a failure strength and corresponding finite crack growth of

$$\sigma_f = \frac{K_{\mathrm{Ic}}}{\sqrt{\pi a}}\frac{1}{\sqrt{1+2\frac{r_p}{a}}} \tag{2.80}$$

$$\Delta a = 4r_p \tag{2.81}$$

where $r_p$ is the plastic zone size given by Eq. (2.74). In terms of elastic-brittle material behavior, the plastic zone must be small compared to the length scale of the crack. For perfect brittle materials, the ratio $r_p/a \to 0$ for which the solution becomes identical to the one of LEFM (see Eq. (2.61) and (2.62)) with a continuous crack growth.

#### 2.5.2.2. Crack initiation of a bar

In an initially perfect lattice material, no sharp cracks are present for the individual lattices, and a crack initiation is required when assuming brittle failure. Following the example from Leguillon (2002), the failure of a simple bar under tensile loading is evaluated. The bar is assumed to consist of a homogeneous isotropic material. An increasing strain is applied to the bar until the bar fails at the critical strain $\varepsilon_c$, and the bar is separated into two parts. At failure, all potential energy of the bar is released

$$-\Delta\Pi = \frac{\Delta A L \sigma_{\mathrm{c}}^2}{2E}. \tag{2.82}$$

where $\sigma_c = E\varepsilon_c$ is the stress immediately prior to failure, and $L$ is the length of the bar. From the energy criterion (Eq. (2.76)) the following relation is identified

$$\sigma_c \geq \sqrt{\frac{2E\mathcal{G}_{\mathrm{c}}}{L}}. \tag{2.83}$$

When the bar becomes sufficiently long, the energy criterion will be fulfilled for loading below the critical strength of the material, and the fracture onset is determined by the stress criterion (Eq. (2.75)).

## 2.6. Interface modeling

As discussed in Section 2.5, the analysis of damage and failure in materials requires an accurate description of the underlying stress field. When materials are placed in confined configurations, for example, when acting as an interface material in a double cantilever beam (DCB), the boundary conditions and resulting stress distributions are significantly altered. In such cases, the interaction between the confined material and the surrounding structure must be included. This section introduces methods for analyzing the mechanical behavior and failure of confined materials.

### 2.6.1. Double cantilever beam

The double cantilever beam (DCB) is a widely used specimen for the study of fracture, e.g., delamination of composite or adhesive failure, and the corresponding fracture toughness (Chen et al., 2021). The DCB specimen consists of two identical elastic beams, referred to as the adherends, which are bonded together by an interface material. A pre-existing crack separates the two adherends at one end, where the crack length is denoted by $a$ (see Figure 2.12 (a)). The adherends are loaded by equal and opposite forces $F$ applied at the

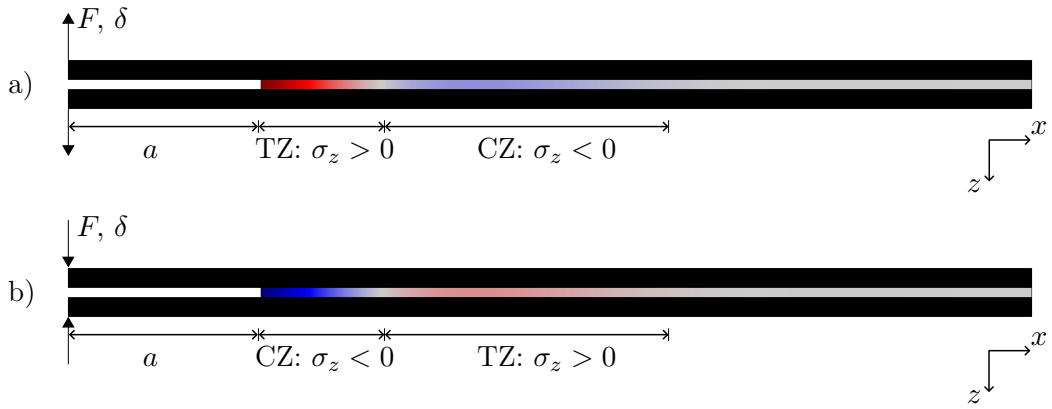


Figure 2.12.: Interface stresses in (a) a DCB (b) and an anti-DCB. The position of the tension zone (TZ) and the compression zone (CZ) is determined by the loading direction.

free boundary of the adherends, generating a Mode I loading condition characterized by crack opening. Applying a mode I loading of the DCB, the interface is locally subjected to tensile and compressive loading, in this work referred to as the local tension zone (TZ) and compression zone (CZ). The tension zone is positioned at the interface front, followed by the compression zone. While damage of bulk material is introduced by tensile stresses at the interface boundary, failure of porous interface materials can also appear in the compression zone. For analysis of thick porous interface materials, the opening mode (mode I) can be replaced by a closing mode (mode I-) as shown in Figure 2.12 (b), thereby switching the position of the tensile and the compression zone. Under mode I- loading, the crack propagation results in closure of the interface, also referred to as an anti crack (Fletcher and Pollard, 1981). The compliance of a system refers to the system's flexibility and is defined for the DCB by

$$c \equiv \frac{\Delta}{F}, \tag{2.84}$$

where $\Delta$ is the displacement between the upper and lower adherend boundaries in line with the applied force $F$. The energy release rate is given by (Anderson, 2017)

$$\mathcal{G} = \frac{F^2}{2b}\frac{\mathrm{d}c}{\mathrm{d}a}, \tag{2.85}$$

where $b$ is the width of the DCB. For a simple estimation of the interface fracture toughness, the free part of the adherends is modeled as two cantilever beams, clamped at the interface boundary, thereby neglecting the stress distribution of the interface. In this case, the compliance $c = 2a^3/(3EI)$ where $I$ is the second moment of area and $E$ is Young's modulus of the adherend (Gere and Goodno, 2013). The corresponding energy release rate

$$\mathcal{G} = \frac{F^2 a^2}{bIE}. \tag{2.86}$$

Under the assumption of a constant fracture toughness of the interface, and using Eq. (2.85) and (2.86), the following relation between the force and displacement can be derived for the crack propagation (Budzik et al., 2012)

$$F \propto \Delta^{-1/2}. \tag{2.87}$$

### 2.6.2. Winkler foundation

The Winkler foundation provides a method for modeling the response of the surrounding structure by representing the confined material by an elastic foundation. Considering a beam on an elastic foundation, the foundation can be represented as a system of independent, linearly elastic springs. The restoring force from the springs is given by

$$q = kw, \tag{2.88}$$

where $k$ is the spring stiffness and $w$ is the beam deflection. Modeling the beam by the Euler-Bernoulli beam theory, the governing ODE is given by

$$\frac{\mathrm{d}^4 w}{\mathrm{d}x^4} + 4\lambda^{-4} w = -\frac{q}{EI}, \tag{2.89}$$

where the characteristic wavelength is given by

$$\lambda = \left(\frac{4EI}{k}\right)^{1/4}. \tag{2.90}$$

The Winker Foundation can be used for the representation of thick interfaces, for which the spring constant is given by

$$k = \frac{bE_\mathrm{i}}{h_\mathrm{i}}, \tag{2.91}$$

where $E_i$ is the elastic modulus of the interface and $h_i$ is the interface thickness. Kanninen (1973) considered the special case of a DCB without an interface. Instead, the adherend itself was used for the foundation, resulting in the characteristic wavelength of

$$\lambda_0 = \frac{h}{6^{1/4}}, \tag{2.92}$$

where $h$ is the adherend thickness.

### 2.6.3. Confined metamaterials

Athanasiadis et al. (2021) proposed a method to analyze confined metamaterials placed between two adherends in a DCB configuration under a mode I loading. Representing the mechanical metamaterial of the interface by a Winkler foundation, the governing ODE of the adherend deflection $w$ is given by

$$\frac{\mathrm{d}w}{\mathrm{d}x} = \frac{4}{\lambda^4} w H(x-a) = 0, \tag{2.93}$$

where $a$ is the initial crack length, $\lambda$ is the characteristic wavelength, and $H$ is the Heaviside step function. The coordinate system is placed so $x = 0$ at the adherend front, where the loading is also applied. The interface appears where $x \geq a$. The characteristic wavelength

$$\lambda = \lambda_0 \left( \frac{\tilde{h}_i}{\tilde{E}_i / \bar{E}} \right)^{1/4}, \tag{2.94}$$

where $\tilde{h}_i \equiv h_i / h_a$ is the ratio between the thickness of the interface $h_i$ and the thickness of the adherend $h_a$. $\tilde{E}_i$ is the relative modulus of the interface material and $\bar{E} \equiv E_a / E_s$ is the ratio between the modulus of the adherend $E_a$ and the modulus of the bulk interface material $E_s$. The critical force is defined as the force at which the damage process of the interface begins. To normalize the force $F$ Athanasiadis et al. (2021) proposed the relation

$$\tilde{F} \equiv \left( \frac{\lambda^3}{E_a I_a h_i} \right) F. \tag{2.95}$$

Considering the appearance of both a tension and compression zone of the interface, combined with a porous interface structure, two potential failure positions need to be considered. In the tension zone, the largest tensile strain appears at the crack front, and failure is assumed when this strain reaches the critical strain of the interface material $\varepsilon_{i,\mathrm{ten}}$. The normalized critical force in tension is given by

$$\tilde{F}_{\mathrm{ten}} = \frac{\varepsilon_{i,\mathrm{ten}}}{1+\tilde{a}}, \tag{2.96}$$

where $\tilde{a} \equiv a/\lambda$. The largest compression strain appears at the position $x$ where $w'(x) = 0$, and when the critical compression strain of the material $\varepsilon_{i,\mathrm{com}}$ is reached, the interface is assumed to fail. The normalized critical force for compression failure

$$\tilde{F}_{\mathrm{com}} = -\frac{\mathrm{e}^{\pi - \arctan(1+2\tilde{a})}}{\sqrt{\frac{1}{2} + \tilde{a}(1+\tilde{a})}} \varepsilon_{i,\mathrm{com}}. \tag{2.97}$$

The normalized critical force is then given by

$$\tilde{F}_{\mathrm{c}} = \min(\tilde{F}_{\mathrm{ten}}, \tilde{F}_{\mathrm{com}}). \tag{2.98}$$

The compliance of the system is given by Eq. (2.84), where $\delta = w(x = 0)$. Normalizing the compliance using (Hedvard et al., 2024)

$$\tilde{c} \equiv \frac{cE_{\mathrm{a}}I_{\mathrm{a}}}{\lambda^3} \tag{2.99}$$

the normalized compliance is given by

$$\tilde{c} = \frac{\tilde{\delta}}{\tilde{F}} = \frac{1}{6}\left(1 + 2(1 + \tilde{a}^3)\right). \tag{2.100}$$

Mechanical metamaterials are typically studied under the assumption of infinite length scales, but when confining the materials, this assumption is no longer valid. The literature for such confined mechanical metamaterials is rather limited. Athanasiadis et al. (2021) proposed to introduce mechanical metamaterials as a replacement for adhesives in thick bondlines, expanding the material range compared to conventional bulk adhesives or the more lightweight foam materials (Athanasiadis et al., 2025). In studies of damage for confined mechanical metamaterials, the lattice structures have indicated a more stable crack growth compared to conventional materials by introducing stick-slip behavior and toughening effects (Heide-Jørgensen et al., 2020; Hedvard et al., 2024). However, the damage process of such confined mechanical metamaterials is rather complex. The porosity of the material leads to the potential of material damage under compression (Adam et al., 2024). Changing the density can change the failure mode, e.g., going from fracture to plastic hinges to buckling as the relative density is decreased (Ye et al., 2021). The topology of the lattice structures can lead to coupling effects (Athanasiadis et al., 2024). Additionally, the introduction of boundary conditions, when confining the metamaterial, can also alter the behavior of the material, the interface stresses, and the corresponding failure modes (de Waal et al., 2025b). However, the geometry-driven properties of mechanical metamaterials also come with new opportunities. Understanding the material behavior, the interface material strength, and toughness can be decoupled (Fulco et al., 2022). Disordering of a lattice can alter the fracture toughness with a minimal loss of strength (Fulco et al., 2025). And a properly designed interface can be used to control the shape and size of the plastic zone. Additionally, the damage pattern can be controlled by a polarization in the interface material (de Waal et al., 2025a).

# 3. Material selection: A reevaluation of brittleness filters

*In this chapter, a physically justified filtering approach for brittle materials is presented, serving as a replacement of the fracture toughness attribute limits (see Section 2.1.2). The chapter begins with a motivation that justifies the need for the reevaluation of the filtering method for brittle materials. Subsequently, an alternative filtering method for brittle materials based on the LEFM theory is presented, and the result is evaluated in detail on the material class level. The proposed filtering method is evaluated against the failure modes of 31 materials covering a wide range of material classes. A case study examining a beam under three different loading conditions is used to evaluate the effect of the presented brittleness filter on the subsequent phases of the material selection process. Additionally, the method is expanded to include defects of various sizes. The results presented here have been published in the peer-reviewed journal paper (Hedvard et al., 2025a), and the peer-reviewed conference proceeding (Hedvard et al., 2025b)[1].*

## 3.1. Motivation for reevaluating the brittleness filter

As stated in Section 2.1.2, in material selection processes, brittle materials are removed in the screening phase using attribute limits on the material fracture toughness. The attribute limit value, when evaluating $K_{\mathrm{Ic}}$ ranges from $5\,\mathrm{MPa}\sqrt{\mathrm{m}}$ to $20\,\mathrm{MPa}\sqrt{\mathrm{m}}$ in the presented literature, while the attribute limit value of $\mathcal{G}_{\mathrm{c}}$ is $1\,\mathrm{kJ/m^2}$ (see Table 2.1). According to Ashby (2016) there exists a rule of thumb among engineers to avoid materials where the fracture toughness

$$K_{\mathrm{Ic}} < 15\,\mathrm{MPa}\sqrt{\mathrm{m}}. \tag{3.1}$$

This rule of thumb significantly reduces the available materials range to metals and some composite materials (see Figure 1.3). Thereby removing ductile materials (e.g., ductile polymers) already in the early design phase, indicating that the chosen attribute limits against brittleness are not performing as intended. Consider the thermoplastic material polypropylene (PP) as an example, with the fracture toughness of $K_{\mathrm{Ic}} = 4.1\,\mathrm{MPa}\sqrt{\mathrm{m}}$ and the yield strength of $\sigma_y = 40\,\mathrm{MPa}$ (Salazar et al., 2014). The material fracture toughness

[1] Recipient of the "Reviewers Choice" award.

is well below the attribute limit of $15\,\mathrm{MPa}\sqrt{\mathrm{m}}$ (see Eq. (3.1)), thereby removing the material under the assumption of a brittle material prone to fracture. However, PP is normally considered a ductile material, which fails by yielding in realistic situations. To determine the correct failure mode of PP, LEFM analysis is considered. The stress intensity factor is given by Eq. (2.61). Assuming an edge crack, the constant $Y = 1.1215$, the defect size is assumed to be $a = 0.5\,\mathrm{mm}$, and the material is loaded to the yield limit, so $\sigma = \sigma_y$. The corresponding stress intensity factor is given by

$$K_{\mathrm{I}} = 1.8\,\mathrm{MPa}\sqrt{\mathrm{m}}. \tag{3.2}$$

As the stress intensity factor is well below the material's fracture toughness ($K_{\mathrm{I}} < K_{\mathrm{Ic}}$), the material is not fracturing at the specified stress state. Increasing the stress level further, the yield strength is exceeded, and the PP is failing by yielding, not fracturing. As shown, the attribute limit of Eq. (3.1) wrongly excludes PP under the assumption of a brittle material.

To evaluate the performance of the fracture toughness attribute limit of Eq. (3.1), currently used against brittle failure, the failure modes of 31 materials listed in Appendix A are evaluated. The selected materials cover a broad range of materials from the material classes metals, composites, polymers, ceramics, and natural materials. Using the setup of a small edge crack of $a = 0.5\mathrm{mm}$, loaded by a uniform stress distribution $\sigma$, the stress intensity factor in mode I is given by Eq (2.61) where $Y = 1.1215$. Brittle materials are prone to fracture-based failure, where the fracture failure mode is assumed to appear when the stress intensity factor exceeds the fracture toughness of the material

$$K_I \geq K_{\mathrm{Ic}}. \tag{3.3}$$

Ductile failure is strength-based failure (e.g., yielding), which is assumed to appear when the stress exceeds the material strength (e.g., yield strength)

$$\sigma > \sigma_{\mathrm{c}}. \tag{3.4}$$

To evaluate whether the materials fail by the fracture-based failure mode of Eq. (3.3) or the strength-based failure mode of Eq. (3.4), the two relations are evaluated for the lowest value of $\sigma$ satisfying one of the conditions. The failure analysis of the 31 materials shows that the attribute limit ($K_{\mathrm{Ic}} < 15\,\mathrm{MPa}\sqrt{\mathrm{m}}$) does not predict the correct failure response (See Figure 3.1). Multiple materials in the material classes of composites, polymers and natural materials, that fail by ductile failure (round) are incorrectly excluded by the attribute limit. At the same time, a brittle metal (8) is incorrectly included for the further ranking phase. This example shows that the currently used fracture toughness attribute limit for screening of brittle materials does not work as intended. Other studies use threshold values in the range of 5–20 $\mathrm{MPa}\sqrt{\mathrm{m}}$ used for the attribute limit (see Table 2.1), moving the screening line in either the positive or negative vertical direction while remaining horizontal (see Figure 1.3). Since the material fracture toughness spans several

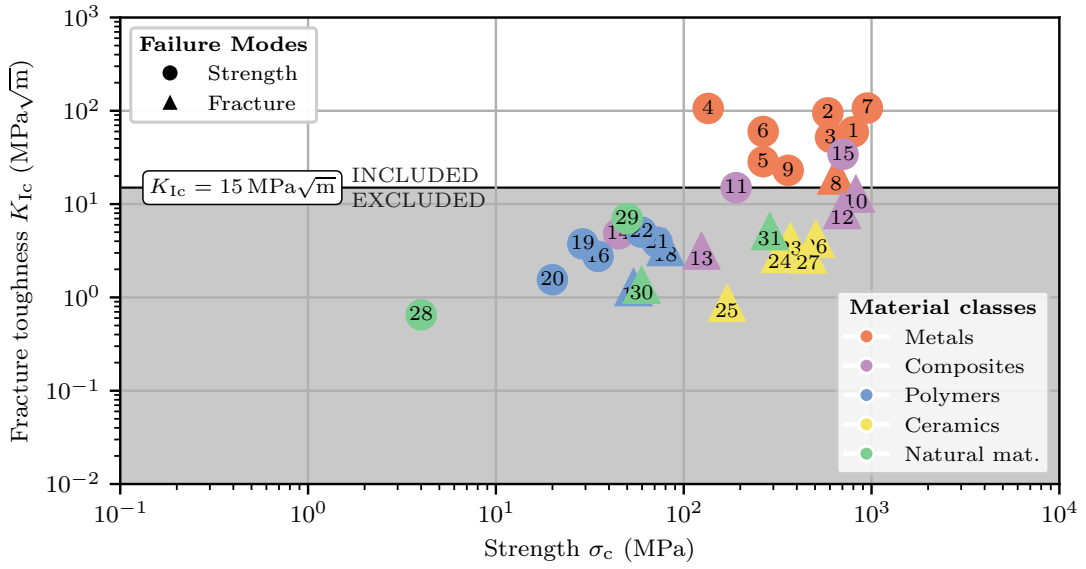


Figure 3.1.: Comparison of the fracture toughness attribute limit of $K_{Ic} > 15\,MPa\sqrt{m}$, and the failure mode of the 31 materials listed in Appendix A. The fracture toughness cannot distinguish between the two material failure modes.

orders of magnitude, ranging from less than $0.01\,MPa\sqrt{m}$ to more than $100\,MPa\sqrt{m}$, the small deviation in the presented fracture toughness limits does not significantly impact the screening process.

For a good material selection process, no material should be removed based on the wrong assumptions:

> "*One should not be too hasty in applying attribute limits; it may be possible to engineer a route around them. A component that gets too hot can be cooled; one that corrodes can be coated with a protective film. Many designers apply attribute limits for fracture toughness, $K_{1c}$, and ductility, $\epsilon_f$, insisting on materials with, as rules of thumb, $K_{1c} > 15 MPa.m^{1/2}$ and $\epsilon_f > 2\%$ in order to guarantee adequate tolerance to stress concentrations. By doing this they eliminate materials that the more innovative designer is able to use to good purpose (the limits just cited for $K_{Ic}$ and $\epsilon_f$ eliminate all polymers and all ceramics, a rash step too early in the design). At this stage, keep as many options open as possible.*" (Ashby, 2016)

This statement coincides with the analysis of the fracture toughness attribute limit, where all the selected polymers, ceramics, and natural materials are removed, independent of the identified material failure mode. However, in some design cases, screening for brittle materials can be a valuable tool. Of course, the filtering method must work as intended by excluding brittle materials while leaving ductile materials. In Figure 3.1, all materials in the upper left corner tend to fail by strength-based failure mode, while the materials

in the lower right corner fail by fracture. The clear distinction between the two failure modes in the figure indicates that a simple filtering method should exist.

## 3.2. Theoretical deviation: LEFM filter

In Section 3.1, it was emphasized that the fracture toughness attribute limits cannot be used as a filter to identify brittle materials. In order to derive a physically justified filtering method for brittle materials, both the fracture-based failure mode from Eq. (3.3) and the strength-based failure mode from Eq. (3.4) must be incorporated in the material failure evaluation to differentiate between ductile and brittle materials. As the filter is intended for brittle materials, the LEFM theory, assuming small process zones compared to the characteristic crack length, is considered for the deviation of the brittleness filter. The stress intensity factor for a mode I loading is given by (see Eq. (2.61))

$$K_I = Y\sigma\sqrt{\pi a}, \tag{3.5}$$

where $Y$ is the shape factor, $\sigma$ is the characteristic stress and $a$ is the characteristic crack length. To avoid fracture of the material, the stress intensity is limited to the fracture toughness of the material

$$K_I < K_{\mathrm{Ic}}. \tag{3.6}$$

From the evaluation of the strength-based failure mode, the maximum stress level on the material is bound to the material strength

$$\sigma = \sigma_{\mathrm{c}}. \tag{3.7}$$

Combining Eq. (3.5) to (3.7) and separating the material and geometrical parameters, the following relation occurs

$$\boxed{\frac{K_{\mathrm{Ic}}}{\sigma_{\mathrm{c}}} > Y\sqrt{\pi a}} \tag{3.8}$$

Satisfying this relation results in a strength-based failure mode, thereby excluding brittle materials that are prone to fracture. Specifying $Y$ and $a$ allows the relation to be evaluated directly from the material properties $K_{\mathrm{Ic}}$ and $\sigma_{\mathrm{c}}$, where the material property ratio $(K_{\mathrm{Ic}}/\sigma_{\mathrm{c}})$ can serve as a filter to identify brittle materials in the screening phase of the material selection. Since the filter is based on the theory of LEFM, it will be referred to as the LEFM filter.

## 3.3. Results and discussion

In the following Section, the proposed LEFM filter is evaluated, and its impact on the material selection is explored. Unless otherwise specified, the LEFM filter limit is based on the conservative choice of an edge crack where $Y = 1.1215$ and using the common definition of a technical defect where $a = 0.5\,\mathrm{mm}$ (Anderson, 2017). This results in a filter limit value of

$$\frac{K_{\mathrm{Ic}}}{\sigma_{\mathrm{c}}} > 1.4\sqrt{\mathrm{mm}} = 0.044\sqrt{\mathrm{m}}. \tag{3.9}$$

This solution can be used as a filter limit to distinguish between brittle and ductile material in the screening phase of the early material selection process. However, the filter limit value depends on the considered defect size. Increasing the defect size increases the filter limit value. The selection of the defect size and its effect on the filtering process will be discussed in more detail below in Section 3.3.5.

### 3.3.1. Evaluation of the LEFM filtering method

In Figure 3.2, the LEFM filter using the filter limit of Eq. (3.9) is compared to the failure mode of the 31 materials from Appendix A. The LEFM filter is depicted as an inclined line with a unit slope, due to the logarithmic scale of the plot. The figure shows that the LEFM filter correctly distinguishes between strength and fracture failure, evaluating that the filter ratio ($K_{\mathrm{Ic}}/\sigma_{\mathrm{c}}$) can differentiate between ductile and brittle materials. Comparing the fracture toughness attribute limit ($K_{\mathrm{Ic}} \geq 15\,\mathrm{MPa}\sqrt{\mathrm{m}}$) and the LEFM filter, the fracture toughness strength diagram is divided into four areas (I to IV). In the area of high strength and low fracture toughness (area II) or low strength and high fracture toughness (area IV), the two filtering methods agree on the exclusion/inclusion of the materials for the further material selection process. However, in the area of low strength and fracture toughness (area I) and the area of high strength and fracture toughness (area III), the two filtering methods differ. In area I, the materials can withstand a high load before strength failure occurs due to their high strength. Therefore, despite their high fracture toughness ($K_{\mathrm{Ic}} \geq 15\,\mathrm{MPa}\sqrt{\mathrm{m}}$), the materials fail by fracture. In area III, the low material strength causes the materials to fail by strength before fracture, despite the low fracture toughness of the materials in this area ($K_{\mathrm{Ic}} < 15\,\mathrm{MPa}\sqrt{\mathrm{m}}$). The LEFM filter correctly captures this behavior, whereas the fracture toughness attribute limit incorrectly classifies the failure mode of the materials in areas I and III.

In a material study by Ashby (1989) of a safe pressure vessel, the aim was to identify the materials capable of withstanding the largest possible defect size. Based on the principle "yield before break", the material index ($K_{\mathrm{Ic}}/\sigma_{\mathrm{c}}$) was derived for the material selection ranking phase. The LEFM filter is based on the same principle, and therefore, it is not surprising that it ends up with the same material relation. To find the best materials

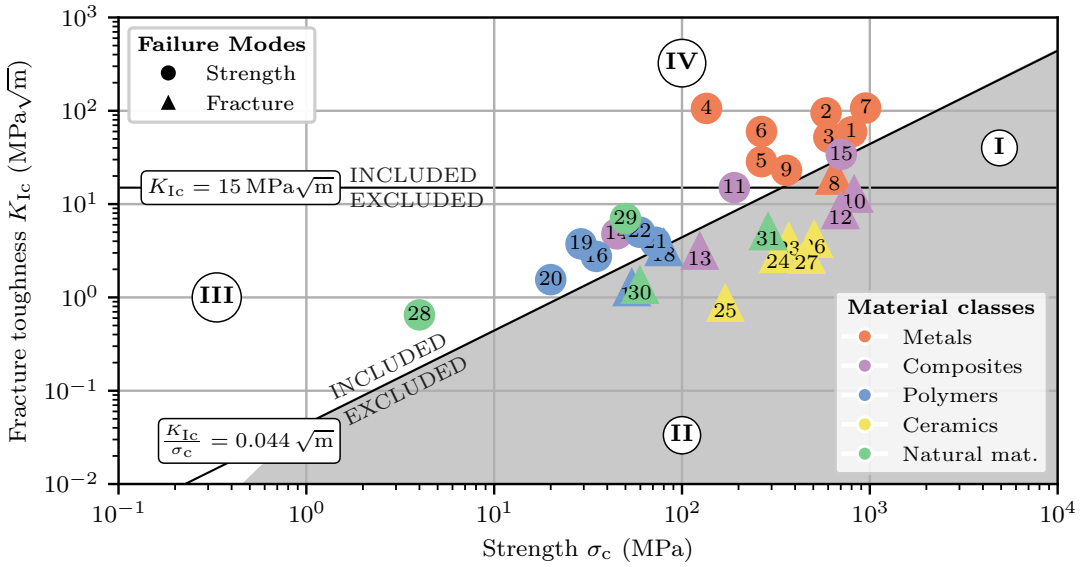


Figure 3.2.: Evaluation of the LEFM filter by comparing the filter to the failure mode of the 31 materials listed in Appendix A, assuming a defect size of 0.5 mm. The fracture toughness attribute limit is shown for reference.

for the safe pressure vessel design, he maximized the ratio of $(K_{Ic}/\sigma_c)$, as this is the way that material indices are used in the ranking phase to quantitatively evaluate materials exhibiting minimal vulnerability to fracture, thereby allowing for substantial defects without compromising structural integrity. However, the LEFM filter aims to exclude materials that are generally prone to fracture by identifying brittle materials under the assumption of small defects.

### 3.3.2. Screening using the LEFM filter

The filter against brittle materials is used in the screening phase in the material selection process, limiting the available materials for the further ranking phase where the material index are used to identify the top-ranked materials (see Section 2.1). Changing the filtering method for screening of brittle materials alters the available materials for the further material selection process. Representing the LEFM filter, along with the fracture toughness attribute limit on the Ashby chart, see Figure 3.3, illustrates the differences in available materials at a material class level. The fracture toughness attribute limit excludes all materials except metals and a few composites, assuming all natural materials, polymers and and ceramics are prone to brittle failure and are therefore excluded from the further material selection. The LEFM relaxes the filtering of materials with low strength and low toughness (area III), allowing polymers and natural materials, as well as some

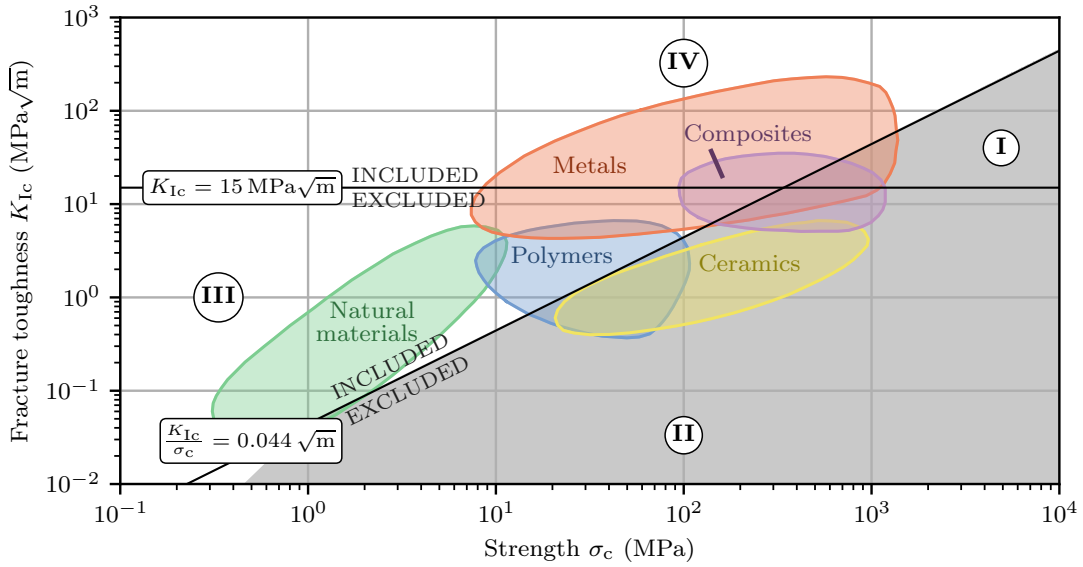


Figure 3.3.: Representation of the LEFM filter on the fracture toughness- strength Ashby chart. The fracture toughness attribute limits are included for reference. As shown, the LEFM includes all material classes except ceramics. The fracture toughness-strength diagram is adapted from (Ashby, 2016).

additional metals and composite materials, to be included in the further material selection. This expands the range of available material classes, broadens the diversity of available materials, thereby expanding the design possibilities and potentially improving the final design. For materials with high strength and high toughness (area I), the LEFM filter excludes a small range of the metals and the composite, originally included by the fracture toughness attribute limit; however, as discussed in Section 3.3.1, those materials are prone to brittle failure and were incorrectly included by the fracture toughness attribute limit, increasing the risk of an unexpected brittle failure.

### 3.3.3. Material fracture toughness considerations

The derived filter is based on the LEFM, assuming the material is linear elastic until fracture occurs. For tough materials where the plasticity cannot be neglected, more advanced methods, e.g., the J-integral, are needed to estimate the fracture toughness of the material(Anderson, 2017). With over 200,000 engineering materials available today (Ashby, 2016), a quick evaluation method based on the material properties is needed to navigate among the significant number of materials available in the early design process. Using the LEFM for the deviation of the filter against brittleness provides a material property ratio ($K_{Ic}/\sigma_c$) valid in the domain of brittle materials for which the filter is

intended. The proposed filter provides a simple method for the filtering of brittle materials in the screening process, but cannot replace a full fracture analysis in the later design process.

In this work, the material fracture toughness is considered by the material property $K_{\mathrm{Ic}}$, defined as the critical stress intensity factor under a mode I loading. The material fracture toughness can also be evaluated under mode II and III loading, where the material resistance against fracture is described by $K_{\mathrm{IIc}}$ and $K_{\mathrm{IIIc}}$, respectively. It has been observed in literature that when a component fails under a mode II loading, the crack forms a kink angle, turning the crack direction such that the mode I loading becomes dominant (Melin, 1986; Lin et al., 2020), while for fracture under mode III the crack surface tends to twist (Shukla et al., 2023). Additionally laboratory testing method in mode III used for determining $K_{\mathrm{IIIc}}$ is challenging, limiting the available data (Aliha et al., 2015). In engineering, $K_{\mathrm{Ic}}$ is often the most relevant parameter to predict the resistance against fracture. Due to the relevance, standardized testing methods, and the amount of available data, $K_{\mathrm{Ic}}$ is here used to describe the fracture toughness of brittle materials. The material fracture toughness can also be defined from the critical energy release rate, $\mathcal{G}_{\mathrm{c}}$, which is related to the stress intensity factor by Eq. (2.73). This material fracture toughness description is, for example, used for adhesive bondlines and interlaminar fracture of composites, where the fracture toughness can be estimated from DCB tests (Kanninen, 1973).

The characteristic fracture length scale can be estimated through various approaches, including the plastic zone size from Eq. (2.74), the cohesive zone modeling (Turon et al., 2007), or considering dimensional analysis (Harder, 1991). In all cases, the length scale is proportional to the size of the plastic zone at the crack tip and is expressed by

$$l \propto \frac{K_{\mathrm{Ic}}^2}{\sigma_{\mathrm{c}}^2}. \tag{3.10}$$

Comparing this length scale with the size of pre-existing defects yields the same relation as the proposed LEFM filter form Eq. (3.8). This interpretation demonstrates that the LEFM-based filtering criterion can be understood as a comparison between the characteristic size of the fracture process zone and the size of the pre-existing defects within a material. The relative magnitude of these two length scales governs the dominant failure mechanism. When the plastic zone at the crack tip is much smaller than the characteristic defect size, unstable crack propagation is more likely, increasing the probability of catastrophic brittle fracture. Conversely, an increasing plastic zone size promotes greater energy dissipation through plastic deformation, stabilizing crack growth and favoring the ductile failure behavior

Table 3.1.: Material selection for a mass minimization of a beam under tension, 3-point-bending or compression. The setup is a deformation constrained limited by the elongation $\delta L_{\max}$, deflection $\delta_{\max}$, and the buckling load $P_{\text{cr}}$.

| **Loading** | **Tension** | **3 point bending** | **Compression** |
|---|---|---|---|
| **Constrains** | $\Delta L = \frac{FL}{a^2 E} \leq L_{\max}$ | $\delta = \frac{FL^3}{4Ea^4} \leq \delta_{\max}$ | $\frac{\pi^2 a^4 E}{12L^2} \leq P_{\text{cr}}$ |
| **Objective function** | Mass minimization: $m = a^2 L\rho$ | | |
| **Free variables** | $a$ | | |
| **Material index** | $M = \frac{E}{\rho}$ | $M = \frac{\sqrt{E}}{\rho}$ | $M = \frac{\sqrt{E}}{\rho}$ |

### 3.3.4. Material selection: mass minimization of deformation-limited design

To explore how the proposed LEFM filter affects the material selection process, a case study for a mass minimization of a beam is considered. The material selection is performed for three different load configurations: Tension loading, 3-point bending, and compression loading. The setup is constrained by the deformation of the beam: the axial elongation $\Delta L_{\max}$ under tensile loading, the deflection $\delta_{\max}$ under bending loading, and the buckling load $P_{\text{cr}}$ under compression loading. The beam cross-sectional area is a square with the side length denoted $a$, and the length of the beam is denoted $L$. The Ashby method (see Section 2.1) is used for each of the three configurations. The objective function, constraints, and free variable for the individual configurations have been determined and are listed in Table 3.1 together with the derived material indices. Note that the beam loaded under bending and compression results in identical material indices. The results of the ranking phase, when considering the 31 materials from Appendix A, covering a broad range of the material spectrum, are presented in Figure 3.4. Prior to the ranking phase, the screening phase has been performed using the proposed LEFM filter, see Figure 3.4a. For comparison, the material selection process is repeated, replacing the LEFM filter with the fracture toughness attribute limit in the screening phase, see Figure 3.4b. Comparing the available materials for the ranking phase, specified by the selected filtering method, a significant difference is observed between the two filtering methods. While the LEFM includes materials from a broad spectrum of material classes, including metals, composites, polymers, and natural materials, the fracture toughness attribute limit only includes metals and composite materials. Comparing the results to Figure 3.2 and 3.3, this is to be expected.

The ranking phase is analyzed for the two material indices $E/\rho$ (tensile loading) and $\sqrt{E}/\rho$ (bending and compression loading) for witch the top 5 materials are listed in Table 3.2, considering either the LEFM filter or the $K_{\text{Ic}}$ filter for the screening of brittle materials prior to the ranking phase. For the material index $E/\rho$, the top 5 materials for the two ranking methods are identical, placing five metals (1,3,4,5,7) as the top-ranked

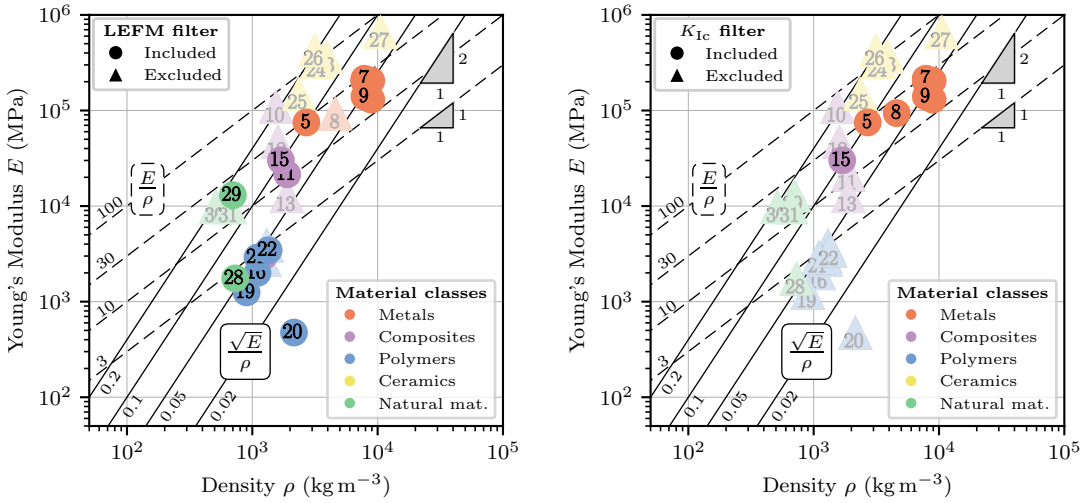


(a) LEFM filtering method

(b) $K_{Ic}$ attribute limit

Figure 3.4.: The results of the ranking phase of the material selection, following the screening phase where either the LEFM filter or the fracture toughness attribute limit is used for filtering of brittle materials.

materials. All the selected top-ranked materials are lying in the area of $E/\rho \approx 30$. By expanding the number of top-ranked materials, the two filtering methods start to differ. For example, the LEFM filtering would then include a natural material (29), which is excluded by the fracture toughness attribute limit. When instead the material index $\sqrt{E}/\rho$ is considered, the difference between the filtering methods is significant already for the top 5-ranked materials. The fracture toughness attribute limit places one composite (15) and five metals (1,5,7,8) as the top-ranked materials, while the LEFM filter places two metals (5,7), two composites (11,15), and one natural material (29) as the top-ranked materials. The LEFM filter provides a broader spectrum of material classes available for the final design choice.

### 3.3.5. Material defect size

Until this point, the size of the material defects has been assumed constant using a value of 0.5 mm. In practice, the material defect size depends on the material type, the production methods, and the quality assurance methods. Take, as an example, the quality assurance of technical ceramics. To control the maximal defect size in components of technical ceramics, proof tests are typically performed (Danzer et al., 2008). The component is exposed to a load, satisfying the crack growth condition for cracks larger than 20 µm (see Eq. (2.61)), so components with too large defects will fracture. For more sensitive

Table 3.2.: Top 5 ranked materials from the materials selection processes. The materials are ordered with respect to their material number. More information about the materials is found in appendix A.

| Material index: $E/\rho$ | | | | | |
|---|---|---|---|---|---|
| LEFM filter | | | $K_{\mathrm{Ic}}$ filter | | |
| No. | Name | Class | No. | Name | Class |
| 1 | High carbon steel | Metal | 1 | High carbon steel | Metal |
| 3 | Medium carbon steel | Metal | 3 | Medium carbon steel | Metal |
| 4 | Stainless steel | Metal | 4 | Stainless steel | Metal |
| 5 | Aluminium alloy | Metal | 5 | Aluminium alloy | Metal |
| 7 | Low alloy steel | Metal | 7 | Low alloy steel | Metal |
| Material index: $\sqrt{E}/\rho$ | | | | | |
| LEFM filter | | | $K_{\mathrm{Ic}}$ filter | | |
| No. | Name | Class | No. | Name | Class |
| 5 | Aluminium alloy | Metal | 1 | High carbon steel | Metal |
| 7 | Low alloy steel | Metal | 5 | Aluminium alloy | Metal |
| 11 | GFRP | Composite | 7 | Low alloy steel | Metal |
| 15 | Glass fiber/ Polyamide | Composite | 8 | Titanium Aluminide alloy | Metal |
| 29 | Wood, along grain | Natural mat. | 15 | Glass fiber /Polyamide | Composite |

applications, such as biomedical implants, the maximal allowed defect size is sometimes decreased to 5 µm (Bermejo and Danzer, 2014).

It is evident that the ratio between the characteristic crack length and the process zone is subjected to alteration when considering different defect sizes. This results in the material exhibiting a greater degree of ductility when the defect size is decreased, and, conversely, becomes more brittle when the defect size is increased. The effect is captured by the LEFM filter, for which the filter limit value is controlled by the defect size (see Eq. (3.8)). In Table 3.3, a set of defect sizes reported in literature for the different material classes is given together with the corresponding LEFM filter limit value. The evaluation of the material failure mode of the 31 materials from Appendix A is repeated using the material class-dependent defect sizes from Table 3.3. The results are shown in Figure 3.5 together with the LEFM filtering lines for the individual material classes. As shown, the variable defect size results in a set of parallel filtering lines, where each shows the transition between the strength-based (round) and fracture-based (triangle) material failure for the corresponding material class. In Figure 3.6, the material class-dependent filtering lines are depicted on a fracture toughness-strength Ashby chart. As shown, the low maximum defect size of 0.02 µm of technical ceramics pushes the material class towards a more ductile behavior compared to the initially assumed defect size of 0.5 mm. The corresponding filtering limit value of $0.009\sqrt{\mathrm{m}}$ allows an area of the material class

Table 3.3.: Estimated initial defect sizes across various material classes with corresponding filter values. The filter limit value are determined from Eq. (3.8) considering the prevented defect size a, and using Y=1.1215.

| Material class | Defect size $a$ [mm] | Filter limit $\frac{K_{\mathrm{Ic}}}{\sigma_f}$ $[\sqrt{m}]$ | Reference |
|---|---|---|---|
| Metals | 0.5 | 0.044 | (Davidson et al., 2003) (Sims, 2012) (Derriso et al., 2016) |
| Composites | 2 | 0.089 | (Hale et al., 1996) (Nsengiyumva et al., 2021) (Guo et al., 2023) |
| Polymers | 2 | 0.089 | (Hale et al., 1996) (Nsengiyumva et al., 2021) (Guo et al., 2023) |
| Ceramics | 0.02 | 0.009 | (Danzer et al., 2007) (Bermejo and Danzer, 2014) |
| Natural materials | 5 | 0.109 | (Thelandersson and Larsen, 2003) |

to be included in further material selection processes. The largest increase in the defect size occurs for natural materials, where the defect size is increased by a factor of 10. The corresponding filtering limit values are increased by a factor of 3, which reduces the ductile area of the material cluster. Despite the increase in the filter limit value for some material classes, the analysis using the material class-dependent filter limits from Table 3.3 allows a range of materials from all material classes to be included after the filtering process. The process here has been performed on the material class level. With additional knowledge, the method can be further expanded to represent the defect on the material level, leading to a material-dependent filtering value.

Considering the defect size as a material property, then the LEFM filter from Eq.(3.8) can be rearranged to

$$\frac{K_{\mathrm{Ic}}}{\sigma_{\mathrm{c}}\sqrt{a}} \geq Y\sqrt{\pi} \tag{3.11}$$

normalizing the filtering approach. The normalized filter limit value is equal for all materials and independent of the defect size. Using the material class-dependent defect size from Table 3.3, the normalized filtering approach is represented on the Ashby chart of Figure 3.7. Be aware that the relation $(K_{\mathrm{Ic}}/\sqrt{a})$ is used on the vertical axis, for which a set of points of the material cluster edges is used to move the material clusters in the vertical direction controlled by the defect size. Decreasing the defect size moves the cluster upwards, while an increase in the defect size moves the cluster downwards. For a full understanding of the material-dependent defect size, considering various materials, production, and quality assessment methods, further research is needed.

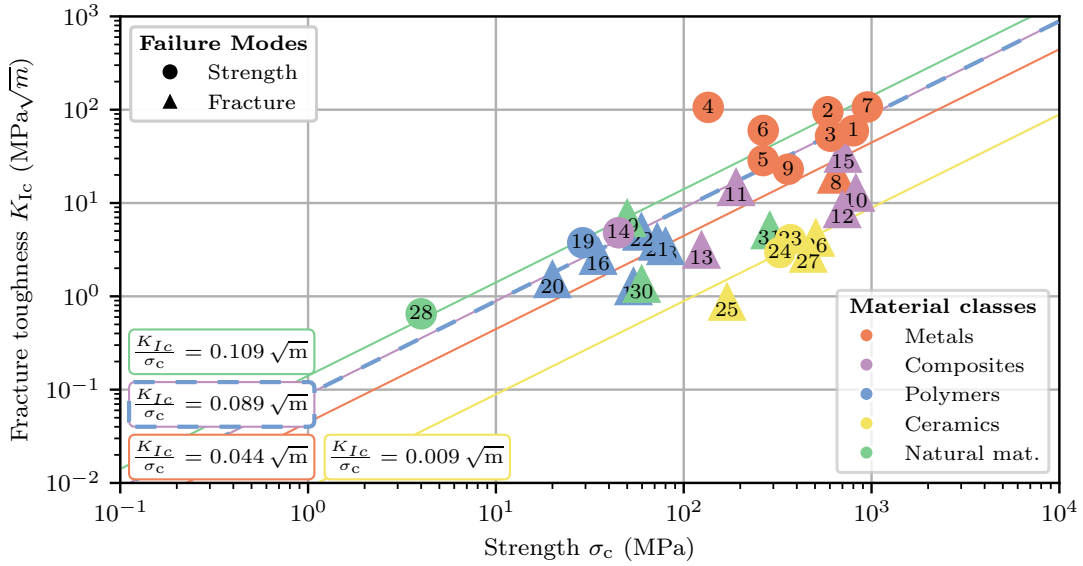


Figure 3.5.: Evaluation of the LEFM filter assuming a material class-dependent defect size. Using the defect size from Table 3.3, all material classes are available after the screening of brittle materials.

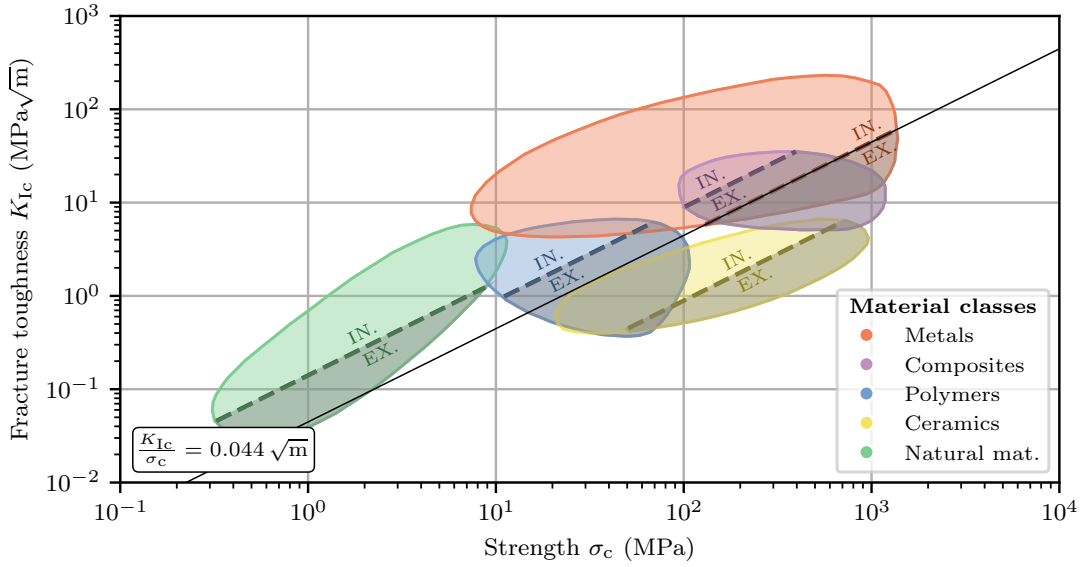


Figure 3.6.: Material class-dependent LEFM filter from Table 3.3 represented on the fracture toughness - strength Ashby chart. For reference, the LEFM filter with a filter limit of $0.044\ \sqrt{\mathrm{m}}$ is depicted corresponding to the defect side of 0.5 mm. The fracture toughness-strength diagram is adapted from (Ashby, 2016).

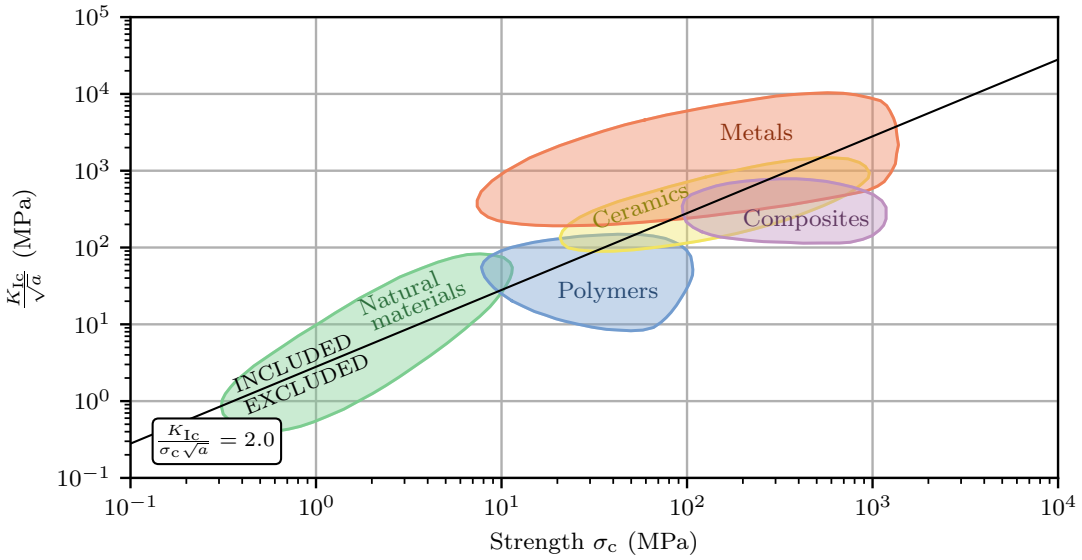


Figure 3.7.: Normalized LEFM filter under the assumption of the material class-dependent defect size from Table 3.3. The fracture toughness-strength diagram is adapted from (Ashby, 2016).

## 3.4. Conclusion

A filtering method evaluating the fracture toughness to strength ratio of the material is proposed as a brittleness filter for the screening phase of the material selection process. The proposed filter for brittle materials can be implemented, representing the material defect on multiple levels. For high precision, the material defect can be specified on the material class or material level, by evaluating the defect size from the material type, the production, and quality assurance methods. However, even a conservative choice of a global defect size provides a more precise filtering method compared to the fracture toughness attribute limits. The proposed brittleness filter allows a broader range of material classes to be available the the further material selection process, improving the material selection process by expanding the design options without compromising on the safety. Additionally, the presented LEFM filter can be normalized, providing a filter limit value independent of the defect size. The proposed LEFM filter provides a physically justified filtering method for the screening of brittle materials in the material selection process.

# 4. Numerical modeling of stretching-dominated architected interfaces

*This chapter presents a numerical analysis of the damage evolution in architected interfaces based on stretching-dominated lattice structures. A finite element model is developed that allows for damage of individual lattice members. Two distinct lattice topologies are investigated to identify the governing damage mechanisms in stretching-dominated architected interfaces. Rotational imperfections originating from the confining adherend are transferred to the interface boundary, introducing bending stresses into the otherwise stretching-dominated mechanical metamaterials. The results demonstrate that the brittle-to-ductile transition of lattice failure is governed by the strength-to-fracture toughness ratio and that the transition point is related to the lattice length. The method has been published in the conference proceedings (Hedvard and Weißgraeber, 2024).*

## 4.1. Introduction

The mechanical metamaterials presented in Section 2.2 represent a promising class of engineered materials capable of significantly extending the range of achievable mechanical properties. Even though the interest in mechanical metamaterials has increased significantly with the development of additive manufacturing, the understanding of their damage processes, especially in confined settings, is still limited (see Section 2.6.3). The porous architected structure of mechanical materials gives rise to complex stress states and damage mechanisms. Depending on the loading and boundary conditions, the interface may experience combined tensile and compressive stresses, leading to competing failure modes such as tensile failure and buckling (Athanasiadis et al., 2021). Focusing on confined, stretching-dominated lattice materials, this chapter aims to improve the understanding of damage and failure processes in architected interfaces. From the finite element analysis (FEA), a numerical framework is developed that allows for damage initiation and progression of the individual lattice members, while both the strength and fracture toughness of the solid material are incorporated in the material damage model. Two stretching-dominated lattice topologies are investigated confined in a DCB configuration

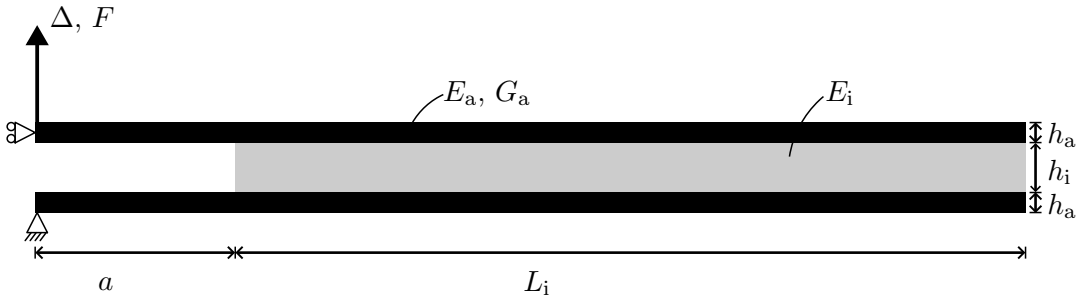


Figure 4.1.: Schematic representation of a DCB with an architected interface positioned in the gray area.

subjected to mode I loading. The resulting damage process is analyzed with particular interest in the boundary-induced effects and the influence of the base material properties.

## 4.2. Numerical framework

This section presents the numerical framework developed to investigate the damage behavior of confined lattice interfaces in a double cantilever beam (DCB) configuration. The considered structural setup, including the geometrical representation of the stretching-dominated lattice topologies, is first introduced. This is followed by the formulation of the material damage model, which captures both tensile failure and buckling-induced failure of individual lattice elements. Analytical estimations are then provided used to implement the model. Finally, the finite element implementation and the underlying modeling assumptions are described.

### 4.2.1. Considered structural situation

A DCB setup was used to confine a stretching-dominated lattice interface material between two carbon fiber reinforced polymer beams used as the adherend, as represented in Figure 4.1. For clarity, the subscript a refers to the adherends, and i refers to the interface. The DCB was loaded in a mode I configuration by introducing a prescribed displacement $\Delta$ at the adherend boundary, where the corresponding reaction force is denoted as $F$. A rectangular cross-section was considered for the adherends, where the height is denoted as $h_\mathrm{a}$, and the width is denoted as $b$. The corresponding second moment of area is $I_\mathrm{a} = bh_\mathrm{a}^3/12$. The initial crack length is denoted as $a$, and the interface height is $h_\mathrm{i}$. The overall interface length is denoted as $L_\mathrm{i}$. Two different topologies, a pillar structure, denoted "|", and a structure of equilateral triangles, denoted "△", were used for the representation of the stretching-dominated lattice interface, as shown

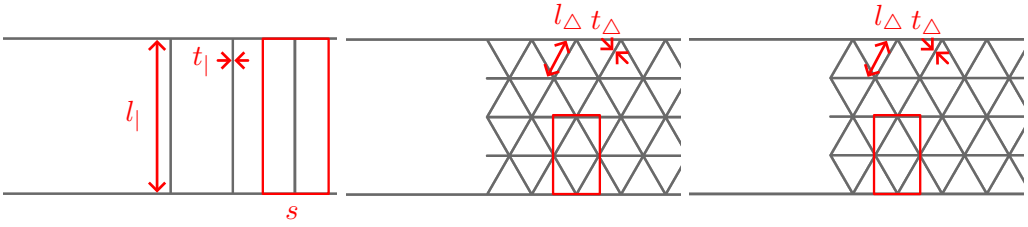


(a) Pillar (P) (b) Triangle 1 (T1) (c) Triangle 2 (T2)

Figure 4.2.: The two interface topologies, pillar and triangular, used for the study. Two interface boundaries are created for the triangular interface. For each interface, the lattice length $l_\mathrm{i}$, lattice thickness $t_\mathrm{i}$, and a unit cell of the material are shown.

in Figure 4.2. The triangular lattice structure was placed in two different positions, altering the boundary of the interface front. The individual lattices have a length $l_\mathrm{i}$, and a rectangular cross-section with a thickness $t_\mathrm{i}$ and a width $b$. For the pillar interface, the lattice length is equal to the interface height ($l_| = h_\mathrm{i}$) and the width of the unit cell, corresponding to the pillar distance is denoted $s_|$. The relative density of the pillar interface

$$\tilde{\rho}_| = \frac{\rho_|}{\rho_s} = \frac{t_|}{s_|}, \tag{4.1}$$

where $\rho_|$ is the density of the pillar interface and $\rho_s$ is the density of the solid material. The triangular interface was created by four rows of equilateral triangles, resulting in the lattice length

$$l_\triangle = h_\mathrm{i}/(2\sqrt{3}). \tag{4.2}$$

The relative density of the triangular interface is given by (Gibson and Ashby, 1997, p. 42)

$$\tilde{\rho}_\triangle = 2\sqrt{3}\tilde{t}_\triangle \left(1 - \frac{\sqrt{3}}{2}\tilde{t}_\triangle\right), \tag{4.3}$$

where $\tilde{t}_\mathrm{i} \equiv t_\mathrm{i}/l_\mathrm{i}$ is the thickness-to-length aspect ratio of the lattice.

### 4.2.2. Material damage model

In order to capture the damage process of the interface material under local tensile loading of a lattice, a material model allowing for complete material softening was implemented. The introduction of a complete softening of a lattice element in the interface corresponds to a failed lattice. Reducing the stiffness of the damaged elements to zero allows the elements to remain after damage, so no re-meshing is needed for the damage process of the interface.

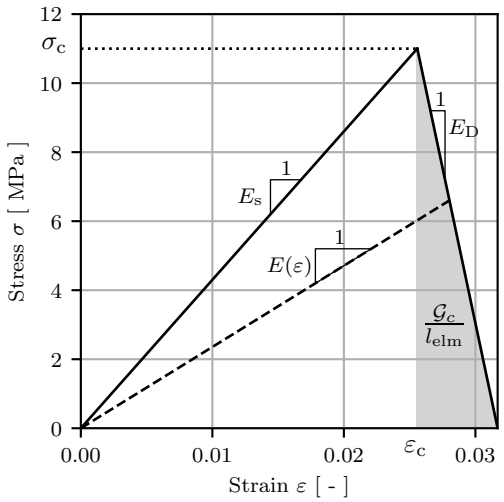


Figure 4.3.: Representation of the material damage model for the bulk interface material. When the critical strain is reached, a linear softening is introduced to the material, controlled by the material's fracture toughness.

The interface material was assumed to be linear elastic until damage. The material damage is introduced when the critical strain $\varepsilon_c = \sigma_c/E_s$ within an element is reached, where $\sigma_c$ is the critical stress and $E_s$ is the Young's modulus of the solid material. After the critical strain is reached, the element starts to soften. Based on the linear traction separation law, the softening tangent modulus for a lattice element is given by (Mangipudi and Onck, 2011)

$$E_D = -\frac{\sigma_c^2 l_{elm}}{2\mathcal{G}_c}. \tag{4.4}$$

where $l_{elm}$ is the element length, determined by the mesh and $\mathcal{G}_c$ is the fracture toughness of the solid material. The stress-strain relationship of the material model is depicted in Figure 4.3. The stress increases linearly until the critical strain is reached and damage is initiated. After the damage initiation, the stress is decreased linearly until a complete softening is achieved. The damage area is represented by the gray area, and corresponds to $\mathcal{G}_c/L_{elm}$ (Tankasala and Fleck, 2020). The material modulus for a specific strain is given by:

$$E(\varepsilon) = \begin{cases} E_s & \text{if } \varepsilon \leq \varepsilon_c \\ \frac{\sigma_c - \varepsilon_c E_D}{\varepsilon} + E_D & \text{if } \varepsilon_c < \varepsilon \leq \varepsilon_u \\ \frac{E_s}{k} \approx 0 & \text{if } \varepsilon > \varepsilon_u \end{cases} \tag{4.5}$$

To implement the material model in the FEA, the material modulus must be strictly positive at all times (Zienkiewicz et al., 2013). Therefore, a lower threshold of the material modulus of $E(\varepsilon_u) = E_S/k$ was implemented, where $k$ is a large positive constant.

When the lattices are loaded in local compression, due to the slender structure, failure is assumed to occur due to buckling. The buckling load $P_c$ is given by Eq. (2.58). The critical buckling load is calculated from the first buckling mode where $m = 1$ and using the correction factor $n_| = 0.5$ for the pillar interface, where the lattices are fixed in both ends and $n_\triangle = 0.7037$ for the triangular interface (Fan et al., 2009). Using the engineering stress and Hooke's law, the corresponding buckling strain $(-P_c/(E_s t_i b))$ is obtained. When reaching the buckling strain, the material modulus is decreased to $E_s/k$ where $k$ is a large positive constant.

### 4.2.3. Analytical estimations

In order to establish an efficient setup for the numerical model, analytical estimations are required for the wavelength and critical displacement at which damage is introduced. In the following section, the material properties for the lattice material are related to the ratio $\tilde{r}_i$, corresponding to the relative density of the lattice materials when neglecting the overlap of the lattices in the joints. This simplification of the relative density is valid for low thickness-to-length ratios of the lattice (low relative densities). For the pillar interface $\tilde{r}_| = \tilde{\rho}$, as no joints appear between the interface lattices, while for the triangular interfaces $\tilde{r}_\triangle = 2\sqrt{3}\tilde{t}$. Under the assumption of a stretching-dominated lattice material, the normalized modulus is given by (see Eq. (2.10))

$$\tilde{E}_i \equiv \frac{E_i}{E_s} = B_i \tilde{r}_i, \tag{4.6}$$

where $B_i$ is a constant dependent on the interface topology. For the pillar interface, $B_| = 1$, while for the triangular structure $B_\triangle = 1/3$ (Wang and McDowell, 2004).

In tensile loading, the damage process of the interface material is assumed to be initiated when the critical stress of the material is reached in one of the lattices (see Figure 4.3). The applied stress at the damage initiation is given by $\sigma_{|,\text{ten}} = \tilde{r}\sigma_c$ for the pillar interface material and $\sigma_{\triangle,\text{ten}} = \tilde{r}\sigma_c/2$ for the triangular interface material (Wang and McDowell, 2004). The corresponding critical strain

$$\varepsilon_{i,\text{ten}} = \frac{\sigma_{i,\text{ten}}}{E_i} = C_i \frac{\sigma_c}{E_s}, \tag{4.7}$$

where $C_i$ is a constant dependent on the topology of the interface material. For the pillar interface $C_| = 1$ and for the triangular interface $C_\triangle = 3/2$. Under compression of the interface, buckling is introduced at the critical strain

$$\varepsilon_{i,\text{com}} = -D_i \frac{\pi^2}{n_i^2} \tilde{t}_i^2 \tag{4.8}$$

where the constant $D_i$ is determined by the topology. For the pillar material $D_| = 1/12$

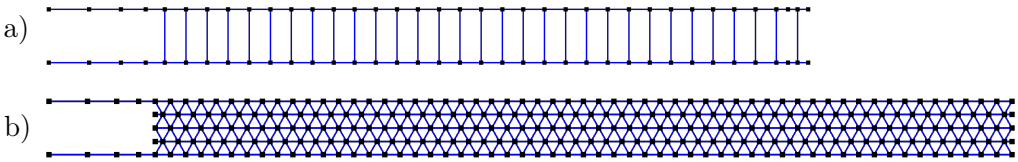


Figure 4.4.: Mesh example for a) the pillar interface, and b) the triangular interface T1.

while for the triangular material $D_{\triangle} = 1/8$ (Fan et al., 2009).

The wavelength for the DCB is determined from Eq. (2.93) using the normalized modulus from Eq. (4.6). The determination of the critical displacement is achieved through the application of Eq. (2.98) for the normalized critical force and Eq. (2.100) for the normalized compliance. The normalized critical force is evaluated based on the critical strain from Eq. (4.7) and Eq. (4.8). The critical displacement is given by

$$\Delta_c = 2\tilde{F}_c\tilde{c}h_{\mathrm{i}}. \tag{4.9}$$

### 4.2.4. Numerical setup

The numerical analysis was performed in COMSOL Multiphysics 6.2, using a quasi-static FEA. The analysis was performed within a 2D environment and included geometric nonlinearity. The elastic-brittle trimethylolpropane triacrylate (TMPTA) was considered for the solid material for the interface, with the properties: Young's modulus $E_{\mathrm{s}} = 430\,\mathrm{MPa}$, material strength $\sigma_{\mathrm{c}} = 11\,\mathrm{MPa}$, Poisson's ratio $\nu = 0.3$, and fracture toughness $\mathcal{G}_{\mathrm{c}} = 837\,\mathrm{J/m^2}$ (Shaikeea et al., 2022). The adherend material was represented by a CFRP UD laminate where the modulus $E_{\mathrm{a}} = E_{11} = 150\,\mathrm{GPa}$ and the shear modulus $G_a = G_{12} = 6\,\mathrm{GPa}$ (de Morais et al., 2002). For the geometry, the adherend cross-section was considered a square where the height and width $h_{\mathrm{a}} = b = 5\,\mathrm{mm}$. The initial crack length was given by $a = 10h_{\mathrm{a}}$, and the interface height was given by $h_{\mathrm{i}} = 25\,\mathrm{mm}$. The distance between the pillars in the pillar interface $s_{|} = 10\,\mathrm{mm}$. The overall interface length was chosen as $L_{\mathrm{i}} = 10\lambda$, where $\lambda$ represents the interface wavelength (see Eq. (2.93)). The selected interface length ensures that the full tensile and compressive zones of the interface were fully developed along the whole damage process. Section 4.2.3 provides the additional information necessary for the estimation of the wavelength. The Timoshenko beam element was utilized for both the adherend and the lattice interface. The free end of the adherend was represented by four elements, while one element was used between each connection point to the interface. Each lattice in the interface was represented by a single element. This is justified by the assumption of a stretching-dominated interface where only limited bending is introduced (Tankasala and Fleck, 2020). The representation of each lattice by a single element guarantees that the failure of the lattice

only occurs at one point along its length. A mesh example for the pillar interface and the triangular interface (T1) is represented in Figure 4.4. The setup was implemented as a displacement-controlled system, governed by a stepwise increase of the displacement $\Delta$ until the maximum displacement $3\Delta_c$ was reached. Subsequent to each step, the material modulus of the interface material was updated by Eq. (4.5). The material modulus was evaluated from the maximum tensile strain over the cross-section, due to the assumption of an elastic-brittle material (Tankasala et al., 2015). However, the material model from Eq. (4.5) is derived from the traction separation law, under the assumption of a constant tensile loading over the cross-section area. Using the maximal tensile strain instead of the average strain results in an overestimation of the released energy during the damage process. But, given the assumption that the interface is dominated by stretching, the effect is presumed to be small. For the material model of Eq. (4.5) a value of $k = 10^9$ is used. A convergence study was performed for the mesh size, the displacement step increase, the interface length, and the constant $k$.

## 4.3. Result and discussion

In the following section, the damage processes of architected interfaces are examined. To facilitate this analysis, an overview of the adherend deformation and its influence on the interface response is provided here. When the loading is applied at the adherend boundary, the DCB undergoes a deformation. The deflection $v$ and rotation $\phi$ of the upper adherend are depicted in Figure 4.5. As described in Section 2.6.1, the adherend deflection of the DCB results in a tension and compression zone of the interface. The tension and compression zone is visualized by the axial stress field of the lattices, see Figure 4.6a. However, as shown for the triangular interface, for horizontal lattices, axial compression appears in the tensile zone, while axial tension appears in the compression zone, due to the local interactions between the lattices of the interface material. The rotation of the adherend introduces a small rotation at the interface boundary, which is transferred to the interface lattices, as shown in Figure 4.6b. As a consequence of this boundary rotation, a small imperfection is introduced into the initially perfect lattice structure.

### 4.3.1. Damage of lattice interfaces

The damage process of the lattice interface can be categorized into two distinct groups, determined by the failure of either the tension or compression zone (see Section 2.6.3). In the case of low relative densities, the material damage occurs in the compression zone, where compression failure (buckling) controls the process. As the density and the corresponding lattice thickness are increased, the resistance against buckling is improved

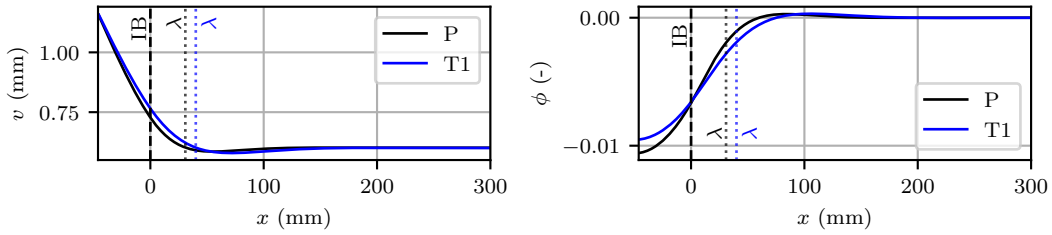


Figure 4.5.: Deflection $v$ and rotation $\phi$ of the upper adherend of the DCB. The results are shown both for the pillar interface (P) and the triangular interface (T1). The results are depicted for the applied displacement $\Delta = 1.2\,\text{mm}$ and the relative density of the interface materials $\tilde{\rho} = 0.2$

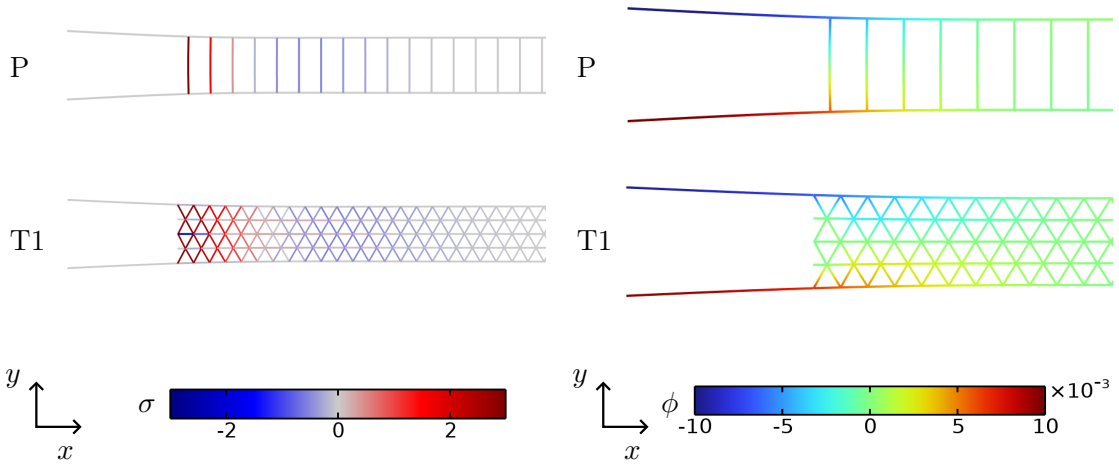


(a) Axial stress field of the latices

(b) Rotation field

Figure 4.6.: Graphical representation of: a) the interface tension and compression zone, and b) the lattice rotations. The results are depicted for the applied displacement $\Delta = 1.2\,\text{mm}$ and the relative density of the interface materials $\tilde{\rho} = 0.2$. The graphical representation of the deformation is scaled by a factor of 5 for better visualization.

(see Eq. (2.58)) and the damage process is moved to the tensile zone. The damage process of the compression zone leads to an unstable damage process where multiple lattices of the interface experience a complete failure, as illustrated in Figure 4.7. In this work, this is considered a complete failure of the interface due to the large area of failed lattices. The corresponding force deflection curve is depicted in Figure 4.8. As shown, the force increases linearly until damage initiation, at which the force shows a sudden drop. In the tension zone, the damage process is dominated by tensile failure of

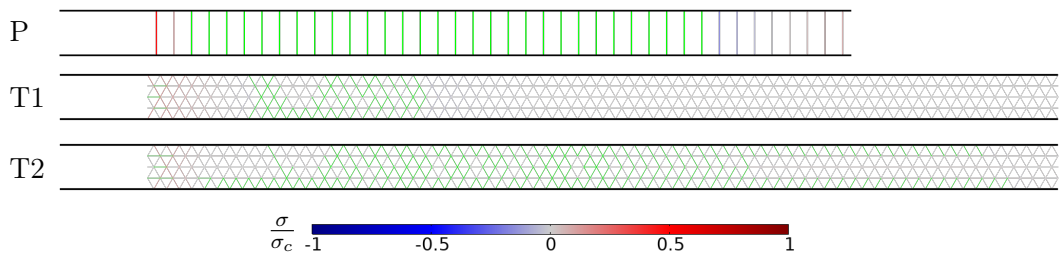


Figure 4.7.: Interface failure of the compression zone for interfaces with a relative density of $\tilde{\rho} = 0.07$. The failed lattices are represented in green. Failure of the compression zone results in unstable crack growth of multiple lattices.

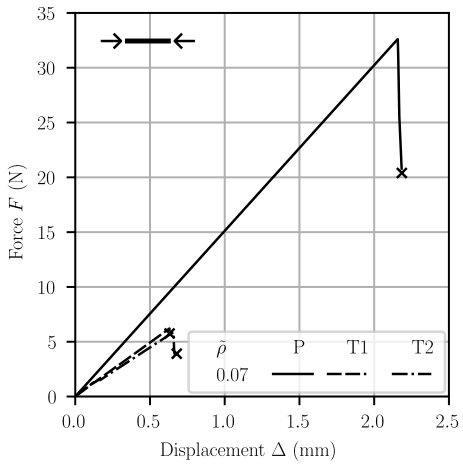


Figure 4.8.: Force displacement relation for the interface density of $\tilde{\rho} = 0.07$ where failure occurs in the compression zone.

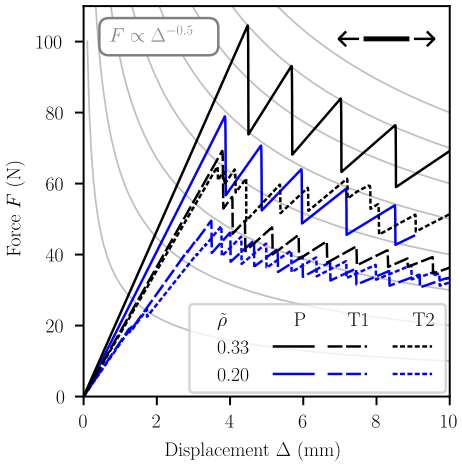


Figure 4.9.: Force displacement relation for the interface densities of $\tilde{\rho} = 0.2$ and $\tilde{\rho} = 0.33$ where failure occurs in the tension zone.

the lattices as illustrated in Figure 4.10. The force-displacement relation follows a linear force increase until damage. A stable damage process is found, where the failure of the individual lattice is detected in the load displacement relation by a sudden force decrease, see Figure 4.9. The damage process of the pillar interface follows the power relation $F \propto \Delta^{-1/2}$ corresponding to the power law relation of continuous interface under the assumption of a constant energy release rate, see Eq. (2.87). For the triangular interfaces (T1 and T2), the force-displacement relations of the damage process differ, depending on both the interface density and the boundary condition. Partly damaged interface areas are found where the adherends are still connected (see Figure 4.10). As an example, consider the interface T2 for the applied displacement $\Delta = 4.4\,\text{mm}$. Next to the interface boundary, there appears an area where every other lattice has failed. The remaining

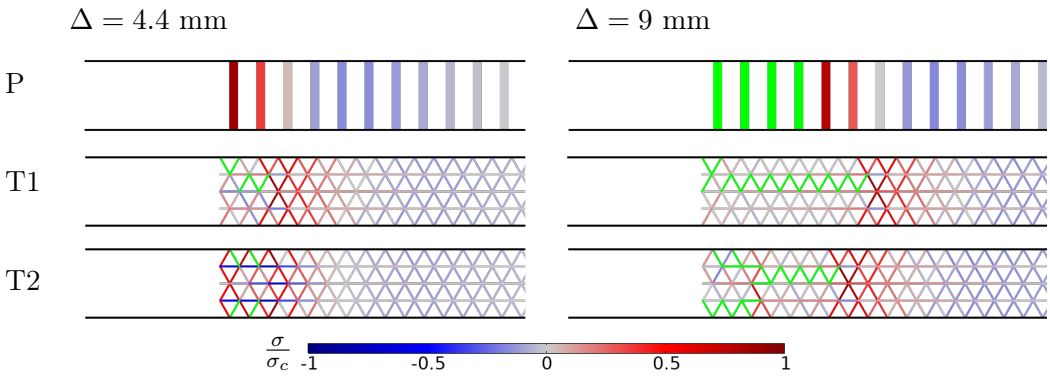


Figure 4.10.: Interface damage of the tension zone represented for the relative density of $\tilde{\rho} = 0.33$. The damage process of the tensile zone provides a stable crack growth. Bridging zones are detected for the triangular lattice interface.

undamaged lattices form bridges between the two adherends. Thereby, providing a closing force that acts as a resistance against the crack growth. For the triangular interfaces, a slower force decrease is detected compared to the power law relation of $F \propto \Delta^{-1/2}$ (see Figure 4.9). Similar bridging effects were observed by Hedvard et al. (2024), considering a simplified version of the numerical model.

The normalized maximal force $\tilde{F}_{max}$ is determined from the maximal reaction force over the full damage process normalized by Eq. (2.95). The result is compared to the analytical estimation of the critical force from Eq. (2.98) in Figure 4.11. The graph is depicted using the logarithmic scale, resulting in a linear representation of the analytical solution. In general, there is a good agreement between the two models regarding the slope and transition point between tension and compression failure. However, the numerical results in general indicate a lower critical load for compression failure (low densities), while a higher critical load appears for the tension failure (high densities). For the triangular interface under tensile-dominated failure, where bridging zones were detected, the force starts to deviate from the linear force decrease. The analytical models differ from the numerical model by assuming small deflections, a specified position interface failure, and neglecting the bending stress and the bridging zones in the evaluation of the interface failure. Those assumptions are relaxed for the numerical model. Consider, as an example, tension failure of the pillar interface. The analytical model assumes the damage initiation of the pillar interface appears at the interface boundary; however, due to the pillar unit cell, the first pillar is placed at a distance $s/2$ from the interface boundary (see Figure 4.2), for which a higher critical force is needed. For the triangular interface where bridging effects appear, the damage processes are in some cases initiated inside the interface material, and not at the interface boundary as assumed by the analytical model (see Figure 4.10). Additionally, the analytical model is derived from the Euler-Bernoulli beam theory, while Timoshenko beam elements are used for the numerical model, thereby including shear

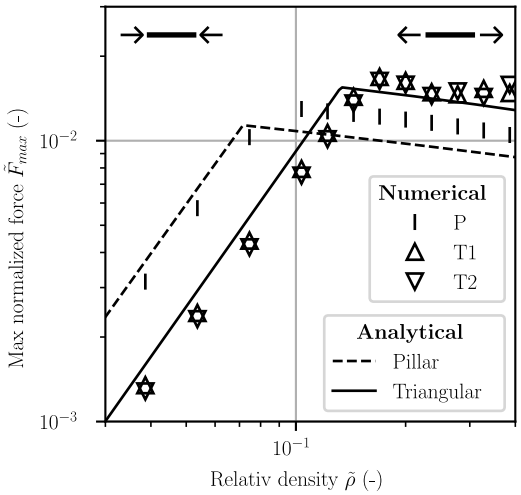


Figure 4.11.: Maximum normalized force for the pillar interface and the two triangular interfaces. For low densities, the interface failure is dominated by buckling of the compression zone. For high relative densities, tensile failure in the tensile zone controls the damage process.

effects.

### 4.3.2. Bending of interface lattices

The mode I loading introduces a small rotation of the lattice interface at the boundary between the interface and the adherend, as illustrated in Figure 4.6b. Considering a lattice under bending, the stiffness is proportional to the second moment of area $I_\mathrm{i}$, and the bending stresses are proportional to the thickness-to-second moment of area ratio $t_\mathrm{i}/I_\mathrm{i}$, controlled by the cross-section geometry. While assuming the interface is purely stretching-dominated, the material properties and introduced stresses are controlled by the cross-sectional area, rendering the specific cross-sectional shape irrelevant.

Considering the DCB with a pillar interface of $\tilde{\rho} = 0.2$, the numerical study is repeated when altering the cross-section geometry of the lattice interface. The aspect ratio of the rectangle cross-section is varied by the constant $z$, such that the width is given by $b/z$, while the lattice thickness is given by $zt_|$. Thereby, the cross-sectional area is kept constant while the second moment of area $I_\mathrm{i} \propto z^2$. The numerical study is repeated for $z$ values of 0.5, 1, and 2. The normalized compliance (normalized by Eq. (2.100)) appears almost independent of the second moment of area, only decreasing by 0.2% when altering $z$ from 0.5 to 2, as shown in Figure 4.12. This change of $z$ corresponds to a 16 times increase in the second moment of area. However, the normalized load-bearing capacity of

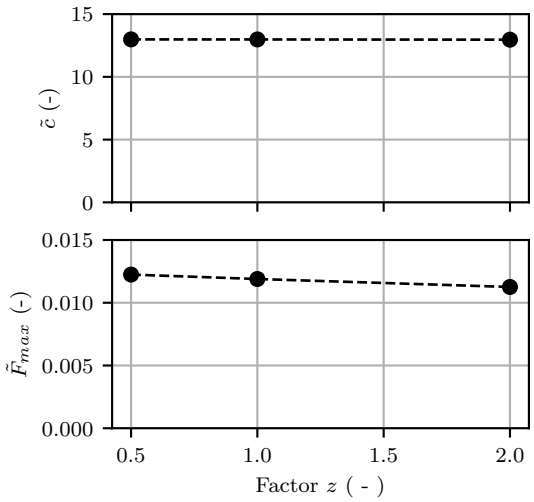


Figure 4.12.: The normalized compliance $\tilde{c}$ and the normalized maximum force $\tilde{F}_{\max}$ are shown for varying lattice thickness, scaled by the factor $z$, while keeping the cross-sectional area constant. The normalized compliance remains constant, whereas the normalized force decreases with increasing lattice thickness.

the structure ($\tilde{F}_{max}$) is significantly affected by the change in the cross-sectional shape, showing a decrease of 8% when the $z$ value is changed from 0.5 to 2. This phenomenon may initially appear counterintuitive; an increase in the second moment of area will, in many structural examples, result in increased stiffness and load-bearing capacity. However, in this specific case, the deformation of the interface is governed by the axial elongation/compression of the lattices, so the increase of $I_{\mathrm{i}}$ only results in a minimal increase in the stiffness. The bending stresses of the lattices are proportional to the thickness of the lattice. As the deformation of the DCB is almost independent of the second moment of area, the beam curvature can be assumed approximately constant with the variation of $z$. So the bending stress becomes proportional to $z$. Xia (2022) made a similar observation for the representation of a beam on a generalized foundation, in which the beam deflection was significantly more sensitive to the stiffness of the Winkler foundation compared to the rotational stiffness. From this analysis, it is shown that under the assumption of failure in the tensile zone, the interface strength can be increased for a specific relative density by decreasing $I_{\mathrm{i}}$. But as the compression failures are governed by the buckling load of Eq. (2.58), the decrease of $I_{\mathrm{i}}$ also decreased the load-bearing capacity in local compression, thereby potentially altering the governing failure mode to compression failure of the compression zone.

### 4.3.3. Material fracture toughness

In this section, the damage initiation is examined with respect to the material's resistance to damage. In the example from Section 2.5.2.2, a lattice under tensile loading was evaluated. For a long lattice, the crack initiation is controlled by the material strength, while for a shorter lattice, the energy criterion controlled by the material fracture toughness must be included in the analysis. In the presented numerical method, both the material strength and fracture toughness are incorporated in the material damage model, shown in Figure 4.3. To study this relation, a parametric study of the material fracture toughness has been performed. The material fracture toughness $\mathcal{G}_c$ was chosen for the study, as changing the geometry or loading leads to coupling effects. A wide span of fracture toughness values ranging from 400 to 4000 $\mathrm{J/m^2}$ was evaluated. This span is not interpreted as a realistic material, considering the other material properties (strength and Young's modulus) and the assumption of the elastic-brittle material, but does only serves as an experiment to understand the interaction between the material strength, fracture toughness, and the interface length. The study is performed for the relative densities of $\tilde{\rho} = 0.1$ and 0.2.

The maximal force from the force-displacement curves is depicted in Figure 4.13. For low values of the fracture toughness $\mathcal{G}_c$, the maximal force is constant, showing the damage process is independent of the material fracture toughness, and the failure of the lattices is governed by the material strength. For high fracture toughness values, above $\mathcal{G}_c \approx 3000\,\mathrm{J/m^2}$, the maximal force starts to increase with an increasing fracture toughness. Figure 4.14 shows force-displacement curves for three representative values of $\mathcal{G}_c$ for the pillar interfaces with $\tilde{\rho} = 0.2$. As illustrated, for all densities the interface failure is initiated at a force of 79 N, when the material strength is reached. For low fracture toughness values ($800\,\mathrm{J/m^2}$), the failure of a pillar results in an abrupt, nearly vertical drop in the force-displacement curve. Increasing the fracture toughness value, the damage process of the individual pillars becomes more gradual, and the slope associated with the failure of the individual pillars increases. At high fracture toughness ($4000\,\mathrm{J/m^2}$), the maximum force exceeds the force of the damage initiation. The two regimes (see Figure 4.13) of low fracture toughness, having constant maximal force, and high fracture toughness with increasing maximal force correspond to a brittle and ductile material behavior. A similar transition between brittle and ductile materials behavior is also found to exist for adhesive joints (Weißgraeber and Becker, 2013). It must be mentioned that the presented numerical model assumes an elastic-brittle behavior of the solid material used for the interface latices, neglecting the plasticity of ductile materials. Therefore, for ductile materials behavior of the solid material, identified by high strength-to-fracture toughness ratios (see Chapter 3), the presented model is invalid, and the result must be used with caution.

Leguillon (2002) suggested that for long bars under axial tension, the damage process is controlled by the material strength. A transition length $L_T$ can be derived from Eq.

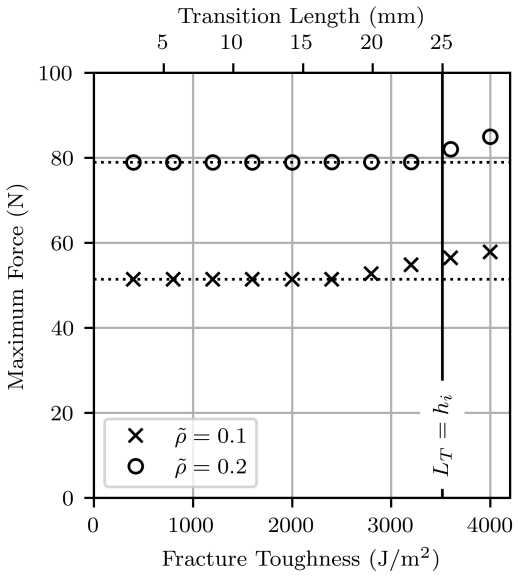


Figure 4.13.: Maximal forces for different fracture toughness values depicted together with the transition length for purely axial loaded bars from Eq. (4.10).

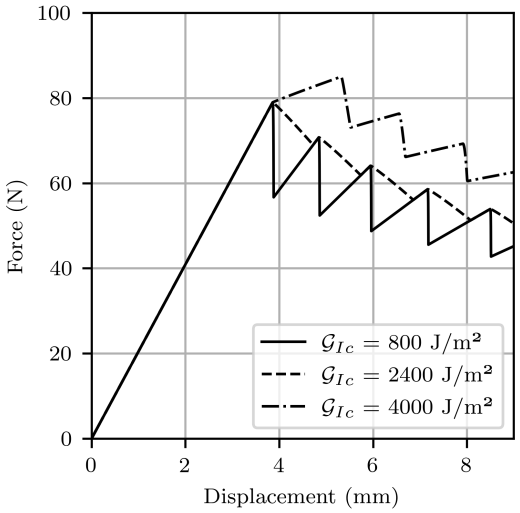


Figure 4.14.: Force displacement plot of a pillar interface with the relative density $\tilde{\rho} = 0.2$. Increasing the fracture toughness results in a more ductile lattice failure process.

(2.83), so

$$L_T = \frac{2E_s\mathcal{G}_c}{\sigma_c^2}. \tag{4.10}$$

For the pillar interface, the length of the bar is defined by the interface height ($L_T = h_i$). From Eq. (4.10), the maximal force should then be constant until the fracture toughness value of $\mathcal{G}_c = 3517\,\mathrm{J/m^2}$ is reached, where after the maximal force is assumed to increase. The numerical results show the material fracture toughness starts to influence the damage process at lower fracture toughness values, down to $\mathcal{G}_c \approx 2800\,\mathrm{J/m^2}$ (see Figure 4.13). The difference is largest for low values of the relative density ($\tilde{\rho} = 0.1$). However, the numerical model also includes boundary rotation of the pillars, so the interface lattices are not purely axially loaded as assumed in Eq. (4.10). In Section 4.3.1 and 4.3.2 a fracture toughness of $G_c = 837\,\mathrm{J/m^2}$ was considered. The corresponding transition length $L_T = 5.9\,\mathrm{mm} < l_\triangle < l_|$. So the damage process is assumed strength-dominated, which is also proven by the nearly vertical load drops shown in Figure 4.9.

The material property ratio ($E_s\mathcal{G}_c/\sigma_c^2$) can be identified from Eq. (4.10), controlling the lattice transition length, between brittle and ductile failure. Using Eq. (2.73), the relation

for the transition length between brittle and ductile lattice failure can be rewritten to

$$L_T = \frac{2K_{\mathrm{Ic}}^2}{\sigma_{\mathrm{c}}^2} \tag{4.11}$$

The material property ratio ($K_{\mathrm{Ic}}^2/\sigma_{\mathrm{c}}^2$) correspond to the filtering ratio of Eq. (3.8), derived in Chapter 3 used to identify brittle materials.

The interface height not only affects the lattice length and the corresponding transition between brittle and ductile lattice failure. The interface height might also influence the effective fracture toughness of the DCB interface. Through an experimental study, Fulco et al. (2022) decoupled the effective strength and toughness of a pillar interface. Increasing the interface height increases the interface compliance and thereby the process zone. For the DCB, the wavelength can be considered as the process zone, determining the characteristic length scale. Increasing the size of the process zone distributes the load over more pillars in the interface, thereby potentially increasing the effective fracture toughness of the interface.

## 4.4. Conclusion

A finite element model for confined stretching-dominated lattice materials was developed, with a material damage model including both the material strength and fracture toughness of the solid material. The lattice is represented by beam elements, enabling the modeling of the damage process of the individual lattices. The results showed a clear distinction between the failure of the compression zone at low relative densities and the failure of the tensile zone at high relative densities. Bridging effects were observed for triangular interfaces when damage appeared in the tensile zone. Two regimes have been identified for the tensile damage process: a brittle regime, where the lattice damage process is controlled by the material strength, and a ductile regime, where the material fracture toughness increases the load-bearing capacity of the lattice interface. A transition between the brittle and ductile behavior is identified, determined by the fracture toughness-to-strength ratio. The same relation was identified for the brittleness filter in Chapter 3. From the interaction between the interface and the confining adherends, small rotation imperfections were introduced at the interface boundary. Assuming a constant relative density, it has been demonstrated that an increase in the second moment of area has a negligible effect on compliance but a decreasing effect on the load-bearing capacity.

# 5. Stability behavior of lattice structures

*This chapter introduces the concept of rotation imperfections, modeling imperfections in slender structures as boundary rotations induced by interactions with connecting elements. Based on Euler–Bernoulli beam theory, a closed-form analytical solution is derived for the load–deflection response of columns undergoing buckling in the presence of rotation imperfections. Both static and kinematically controlled rotation imperfections are considered, and a method for estimating the rotation imperfection due to column shortening effects is proposed. The influence of rotation imperfections is investigated for simple lattice structures under various loading conditions and in combination with geometric imperfections. All analytical predictions are validated against nonlinear numerical reference solutions. The results are under review in the peer-reviewed journal (Hedvard and Weißgraeber, 2026).*

## 5.1. Introduction

From the analysis of the DCB with architected interfaces presented in Chapter 4, it was identified that bending of the adherends induces boundary rotations at the lattice interface (see Figure 4.6b). These boundary rotations disturb the initially perfect geometry of the slender lattice members. It is well established that imperfections for compression-loaded slender structures can significantly reduce the load-bearing capacity, and accurate characterization of imperfections is essential for reliable predictions of the buckling behavior (see Section 2.4.2). Two fundamental types of imperfections commonly considered in the literature are geometric imperfections and load eccentricity (Bažant and Cedolin, 2010). Geometric imperfections introduce an initial curvature to the column, thereby violating the assumption of an initially straight structure. Load eccentricity applies a boundary moment of magnitude $Pe$, where $P$ is the compressive load and $e$ denotes the size of the eccentricity. The load eccentricity imperfection requires the column boundary to be free to rotate, while for clamped column boundaries, such boundary moments are eliminated. Rotation imperfections can be observed for rigidly connected members, for example, as foot-point rotations of the foundation of columns, ceiling bending in civil engineering structures, misalignment of fixtures in mechanical systems, or as demonstrated by boundary rotations of architected interfaces. These imperfections can develop even in initially perfect structures and are therefore not well represented

by geometric imperfections. To improve the buckling analysis of lattice structures and architected interfaces, the concept of rotation imperfections is introduced, capturing the boundary-induced rotations arising from structural interactions. A closed-form analytical solution for the load–deflection response of a column with rotation imperfections is derived and subsequently employed to analyze the buckling behavior of lattice structures.

## 5.2. Modeling approach

This section presents the analytical framework for column buckling with rotation induced boundary imperfections, including both static and kinematic effects. Additionally, a numerical reference model is presented.

### 5.2.1. Column buckling with static rotation imperfections

The analysis of buckling of imperfect columns is often conducted under the assumption of geometrical imperfections where the shape is determined by one or more of the buckling modes (see Section 2.4.2). These assumed geometrical imperfections are designed to align with the established boundary conditions of the structural framework. Introducing a rotation to the clamped column boundary, it becomes evident that the initial boundary condition is violated. In this section, the load-deflection relation for static rotation imperfections of clamped columns is derived. This relation establishes the foundation for subsequent investigation of kinematic-controlled rotation imperfections.

A prismatic column is considered with the rectangular cross-sectional area $A$ and the second moment of area $I$. The column material is assumed linear elastic, where the Young's modulus of the material is denoted by $E$. The deviation is based on an assumption of small deflections and rotations. In Figure 5.1, the column with an initial imperfection of $W_{\mathrm{I}}(X)$ is depicted in black. When applying a compression load $P$ at the column, the deflection of the column is increased by $W_{\mathrm{B}}(X)$ from the buckling response. The total deflection of the beam

$$W(X) = W_{\mathrm{I}}(X) + W_{\mathrm{B}}(X). \tag{5.1}$$

A free body diagram of the lower part of the column is shown in Figure 5.2. Assuming static equilibrium, the sum of the moments must equal zero. Considering the summation of the coordinate origin, the following relation is found

$$M(X) - PW(X) - M_{\mathrm{C}} = 0, \tag{5.2}$$

where $M_C$ is the moment of the clamped boundary. Combining with Eq. (2.42), (5.1)

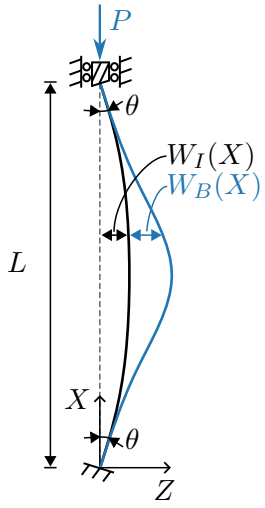


Figure 5.1.: Schematic representation of the deflection from the initial imperfection and the column buckling.

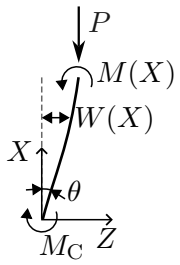


Figure 5.2.: Free body diagram of a column section.

and (5.2) the governing ODE is given by

$$W_B'' + \mu^2 W_B = \mu^2 W_I - \mu^2 \frac{M_C - M_I}{P}, \tag{5.3}$$

where $\mu^2 = P/EI$ and $M_I = -EIW_I''$. The rotation imperfection moment, denoted $M_I$, is the bending moment introduced by the rotation imperfection, which is constant over the length of the column. The reaction moment at the clamped column boundary is equivalent to the sum of the boundary moment introduced by the rotation imperfection and the moment from the buckling process, denoted $M_B$:

$$M_C = M_I + M_B. \tag{5.4}$$

#### 5.2.1.1. Rotation imperfection deflection

The deflection initiated by the rotation imperfection must satisfy the boundary conditions

$$W_I(0) = W_I(L) = 0 \tag{5.5}$$
$$W_I'(L) = -W_I'(0) = \theta. \tag{5.6}$$

Solving Eq. (2.43) using those boundary conditions, the imperfection deflection of the column is given by

$$W_{\mathrm{I,EB}} = \theta X - \frac{\theta}{L} X^2. \tag{5.7}$$

To derive a closed-form solution for the governing ODE from Eq. (5.3), the imperfection deflection of Eq. (5.7) is transformed to a sinus function using a half sinus wave to represent the full column length. The sinus-shaped imperfection is given by

$$W_{\mathrm{I}} = \alpha \sin\left(\frac{\pi X}{L}\right) \tag{5.8}$$

where $\alpha$ is the imperfection amplitude. This sinus representation is selected due to the symmetrical nature around the column center, the alignment with the boundary condition $W_{\mathrm{I,EB}}(0) = W_{\mathrm{I,EB}}(L) = 0$, and the ability to induce a rotation of the boundary. To specify the imperfection amplitude, three methods are considered:
I) The imperfections are controlled by the boundary rotation $\theta$. By matching the boundary rotation such that $W'_{\mathrm{I,EB}} = W'_{\mathrm{I}} = \theta$, the amplitude is given by

$$\alpha_\theta = \frac{\theta L}{\pi}. \tag{5.9}$$

II) In the context of buckling analysis, the second-order term $PW$ is incorporated into the analysis, as discussed in Section 2.4.1. The contribution from the imperfection is determined by the deflections $W_{\mathrm{I}}$. Fixing the maximal deflection before and after the transformation, such

$$W_{\mathrm{I}}(L/2) = W_{\mathrm{I,EB}}(L/2) \tag{5.10}$$

the imperfection amplitude becomes

$$\alpha_{\mathrm{W}} = \frac{\theta L}{4}. \tag{5.11}$$

III) Introducing the boundary rotation $\theta$ at the column boundary, the reaction moment is given by (Gere and Goodno, 2013, p. 1050)

$$M_R = \frac{2EI\theta}{L}. \tag{5.12}$$

Fixing the reaction moment, the amplitude can be derived by the Ritz method (see Section 2.3.3.2), by considering the sinus-shaped imperfection from Eq. (5.8) as the trial function, where $\alpha$ is the unknown constant. The internal strain energy can be expressed by combining Eq. (2.46) and (2.42), such that the strain energy

$$U = \frac{1}{2}\int_0^L EI(W_I'')^2 \mathrm{d}x = \frac{EI\alpha_{\mathrm{M}}^2\pi^4}{4L^3}. \tag{5.13}$$

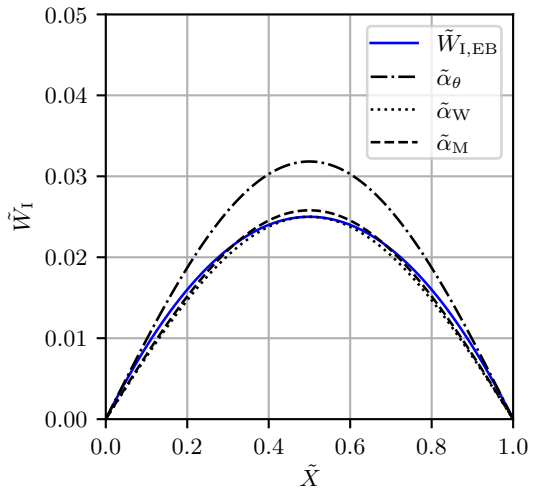


Figure 5.3.: Comparison of the beam deflections from Eq. (5.7) and the sinus-shaped imperfections considering the three imperfection amplitudes from Eq. (5.9) to (5.11). A boundary rotation of $\theta = 0.1$ is used.

The external work is given by

$$W_\mathrm{E} = 2M_R W_I'(X=0) = \frac{4\pi EI\theta\alpha_\mathrm{M}}{L^2}. \tag{5.14}$$

Minimizing the potential energy of Eq. (2.44), the imperfection amplitude is given by

$$\alpha_\mathrm{M} = \frac{8L\theta}{\pi^3}. \tag{5.15}$$

Normalizing the length dimensions by the column height, such that $\tilde{W} \equiv W/L$, $\tilde{\alpha} \equiv \alpha/L$, and $\tilde{X} \equiv X/L$, the normalized sinus-shaped imperfection is given by

$$\tilde{W}_\mathrm{I} = \tilde{\alpha}\sin(\pi\tilde{X}). \tag{5.16}$$

Figure 5.3 represents the normalized sinus-shaped imperfection using the three different amplitude definitions ($\alpha_\theta$, $\alpha_\mathrm{W}$, $\alpha_\mathrm{M}$). For reference, the normalized deflection $\tilde{W}_{\mathrm{I,EB}}$ from Eq. (5.7) is depicted. As shown, using the amplitude $\tilde{\alpha}_\theta$ leads to a significant overestimation of the imperfection deflection, while using either $\tilde{\alpha}_W$ or $\tilde{\alpha}_\mathrm{M}$ as the amplitude results in god results compered to the the reference deflection $\tilde{W}_{\mathrm{I,EB}}$.

#### 5.2.1.2. Column buckling for static rotation imperfections

The following expression for the governing ODE is found by inserting the sinus-shaped imperfection deflection from Eq. (5.8) into the governing ODE from Eq. (5.3):

$$W_{\mathrm{B}}'' + \mu^2 W_{\mathrm{B}} = -\mu^2 \frac{M_{\mathrm{B}}}{P} - \mu^2 \alpha \sin\left(\frac{\pi X}{L}\right). \tag{5.17}$$

The general homogeneous solution is given by

$$W_{\mathrm{B,h}} = c_1 \sin(\mu X) + c_2 \cos(\mu X), \tag{5.18}$$

where $c_1$ and $c_2$ are two arbitrary constants. To find a solution to the non-homogeneous part of the governing ODE, the method of undetermined coefficients is considered, where I assume a solution to the governing ODE in the form of (Kreyszig et al., 2011, p. 81)

$$W_{\mathrm{B,s}} = c_3 + c_4 \sin\left(\frac{\pi X}{L}\right), \tag{5.19}$$

where $c_3$ and $c_4$ are two arbitrary constants. The solution is inserted into Eq. (5.17) resulting in the following expression:

$$c_3\mu^2 - c_4 \frac{\pi^2}{L^2} \sin\left(\frac{\pi X}{L}\right) + c_4 \mu^2 \sin\left(\frac{\pi X}{L}\right) = -\mu^2 \frac{M_{\mathrm{B}}}{P} - \mu^2 \alpha \sin\left(\frac{\pi X}{L}\right). \tag{5.20}$$

Given the necessity of Eq. (5.20) to be valid for all values of $X$, the constant terms (indicated by the blue underline) and the sinus terms (indicated by the red underline) can be evaluated separately:

$$\begin{aligned} & c_3\mu^2 = \frac{\mu^2 M_{\mathrm{B}}}{P} \\ \Rightarrow \quad & c_3 = -\frac{M_{\mathrm{B}}}{P}, \end{aligned} \tag{5.21}$$

$$\begin{aligned} & -c_4 \frac{\pi^2}{L^2} \sin\left(\frac{\pi X}{L}\right) + \mu^2 c_4 \sin\left(\frac{\pi X}{L}\right) = -\mu^2 \alpha \sin\left(\frac{\pi X}{L}\right) \\ \Rightarrow \quad & c_4 = \frac{\alpha}{\frac{\pi}{\mu^2 L^2} - 1}. \end{aligned} \tag{5.22}$$

Inserting Eq. (5.19) in the governing ODE from Eq. (5.17), when specifying $c_3$ and $c_4$ by Eq. (5.21) and (5.22), it can be shown that $W_{\mathrm{B,s}}$ is a valid solution. The general solution

for the governing ODE is given by

$$\begin{aligned} W_{\mathrm{B}} &= W_{\mathrm{B,h}} + W_{\mathrm{B,s}} \\ &= c_1 \sin(\mu X) + c_2 \sin(\mu X) - \frac{M_{\mathrm{C}}}{P} + \frac{\alpha}{\frac{\pi}{\mu^2 L^2} - 1} \sin\left(\frac{\pi X}{L}\right). \end{aligned} \tag{5.23}$$

Using the boundary conditions of no displacement of the endpoints $W_{\mathrm{B}}(0) = W_{\mathrm{B}}(L) = 0$, the arbitrary constants

$$c_1 = \frac{M_{\mathrm{C}}}{P} \tan\left(\frac{\mu L}{2}\right), \tag{5.24}$$

$$c_2 = \frac{M_{\mathrm{C}}}{P}. \tag{5.25}$$

The relationship between the boundary moment and force is determined by the clamped boundary condition $W_{\mathrm{B}}(0)' = 0$, so

$$\frac{M_{\mathrm{B}}}{P} = \frac{\frac{\alpha\pi}{\mu L}}{\left(1 - \frac{\pi^2}{L^2\mu^2}\right) \tan\left(\frac{\mu L}{2}\right)}. \tag{5.26}$$

Inserting Eq. (5.8) and (5.23) in (5.1) using Eq. (5.24) to (5.26) and normalizing the result, the total normalized deflection is given by

$$\tilde{W}(\tilde{X}) = \frac{\tilde{\alpha}}{1 - 4\tilde{P}} \sin\left(\pi\tilde{X}\right) + \frac{2\tilde{\alpha}\sqrt{\tilde{P}}}{1 - 4\tilde{P}} \left( \frac{1 - \cos\left(2\pi\sqrt{\tilde{P}}\tilde{X}\right)}{\tan\left(\pi\sqrt{\tilde{P}}\right)} - \sin\left(2\pi\sqrt{\tilde{P}}\tilde{X}\right) \right), \tag{5.27}$$

where $\tilde{W} \equiv W/L$, $\tilde{X} \equiv X/L$, $\tilde{\alpha} \equiv \alpha/L$ and $\tilde{P} \equiv P/P_{cr}$. The load $P_{cr}$ is the Euler buckling load of a column clamped at both boundaries, given by Eq. (2.58). The maximal deflection of the column is given by the midspan deflection. The normalized midspan deflection is given by:

$$\tilde{\delta} = \frac{\tilde{\alpha}}{1 - 4\tilde{P}} \left( 1 - 2\sqrt{\tilde{P}} \tan\left(\frac{\pi\sqrt{\tilde{P}}}{2}\right) \right). \tag{5.28}$$

Please note that this solution has a singularity and is not defined for values of $\tilde{P} = 1/4$, which correspond to the second (pinned-pinned) Euler buckling case. This issue can be addressed by identifying a solution in the near vicinity of the load in question.

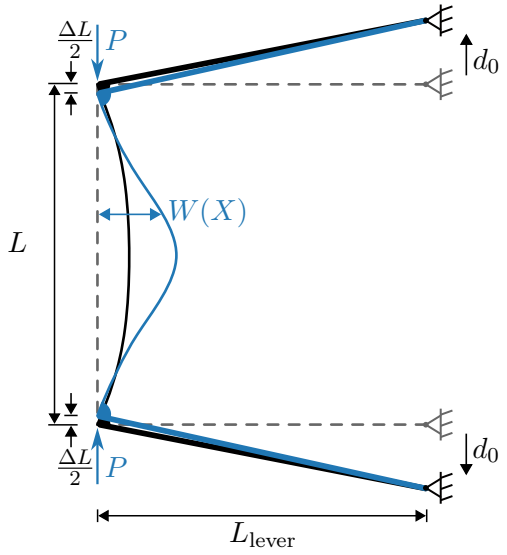


Figure 5.4.: Representation of a column positioned between two lever arms. The displacement $d_0$ of the lever arm introduces an initial imperfection, and the following loading process increases the boundary rotation due to the column shortening $\Delta L$.

### 5.2.2. Kinematic imperfections from column shortening

Until this point, the rotation imperfections have been considered static, assuming the boundary rotation is independent of the loading and buckling response. However, in certain structural scenarios, a coupling exists between the column and the confining elements, such that column deflection and corresponding shortening result in a rotation of the confining element. An example is given in Figure 5.4, where a column is clamped between two rigid levers of the length $L_{\text{lever}}$. To introduce the initial rotation imperfection, the lever ends are moved a distance $d_0$ away from each other, as illustrated in the figure (black lines). When the compression load $P$ is applied on the column, the height of the column is shortened by $\Delta L$. While the columns are shortened, the levers rotate, thereby due to the rigid connection increases the rotation imperfection of the column boundary.

In this scenario, a column with a rectangular cross-section is considered. The cross-sectional area $A = bt$, where $b$ is the width and $t$ is the thickness of the column. The second moment of area $I = bt^3/12$. To evaluate the beam deflection of the shortened column, the column deflection from Eq. (5.27) is modified to account for the column shortening. The normalized position $\tilde{X}$ is replaced with $\tilde{X}/(1 - \Delta\tilde{L})$ where $\Delta\tilde{L} \equiv \Delta L/L$

is the normalized column shortening. The modified column deflection is given by

$$\tilde{W}_{\Delta L}(\tilde{X}) = \frac{\tilde{\alpha}}{1-4\tilde{P}} \sin\left(\frac{\pi\tilde{X}}{1-\Delta L}\right) + \frac{2\tilde{\alpha}\sqrt{\tilde{P}}}{1-4\tilde{P}} \left( \frac{1-\cos\left(\frac{2\pi\sqrt{\tilde{P}}\tilde{X}}{1-\Delta L}\right)}{\tan\left(\pi\sqrt{\tilde{P}}\right)} - \sin\left(\frac{2\pi\sqrt{\tilde{P}}\tilde{X}}{1-\Delta L}\right) \right). \tag{5.29}$$

The total column shortening, $\Delta L$, consists of two contributions: the shortening of the column from the axial compression, $\Delta L_\varepsilon$, and the shortening of the column height due to the deflection of the column. The normalized axial shortening of the column due to elastic compression is given by $\Delta\tilde{L}_\varepsilon = \frac{P}{EA}$, for which the normalized axial shortening

$$\Delta\tilde{L}_\varepsilon = \frac{\pi^2}{3}\tilde{t}^2\tilde{P}, \tag{5.30}$$

where $\tilde{t} \equiv t/L$ is the normalized thickness of the column. The normalized arc length is found by numerical integration of (Kreyszig et al., 2011, p. 391)

$$\tilde{L}_{\text{arc}} = \int_0^{1-\Delta\tilde{L}} \sqrt{1+\left(\tilde{W}'_{\Delta L}\right)^2}\,\mathrm{d}\tilde{X}. \tag{5.31}$$

Following the arc of the column, the column length is only shortened by the axial shortening $\Delta\tilde{L}_\varepsilon$, such:

$$\tilde{L}_{\text{arc}} = 1 - \Delta\tilde{L}_\varepsilon \tag{5.32}$$

Combining Eq. (5.30) to (5.32), the column shortening can be determined. When knowing the column shortening for the specified load case, the boundary rotation angle is given by

$$\theta = \arcsin\left(\tilde{d}_0 + \frac{\Delta\tilde{L}}{2\tilde{L}_{\text{lever}}}\right) \tag{5.33}$$

where the normalized lever length $\tilde{L}_{\text{lever}} \equiv L_{\text{lever}}/L$.

The load deflection relation of a column with kinematic-controlled rotation imperfections due to column shortening is solved by the semi-analytical approach described by the flow chart in Figure 5.5. The analysis is performed for a stepwise increasing normalized load, where $\Delta\tilde{P}$ determines the normalized load increase. To obtain a continuous result, the point of the singularity ($\tilde{P} = 1/4$) of Eq. (5.28) is excluded while values very close to the point are evaluated instead. For each load step, the corresponding column shortening is evaluated by an iterative process. Newton's method is used for the numerical integration of Eq. (5.31) to determine the column shortening, for which the corresponding rotation imperfection angle given by Eq. (5.33) and imperfection amplitude given by Eq. (5.11) are evaluated. The iterative process is continued until the change in column length $|(\Delta L_i - \Delta L_{i-1})/\Delta L_{i-1})|$ is smaller than the threshold $\epsilon$ (e.g., $\epsilon = 10^{-9}$). When the threshold is reached, the normalized load and corresponding normalized midspan

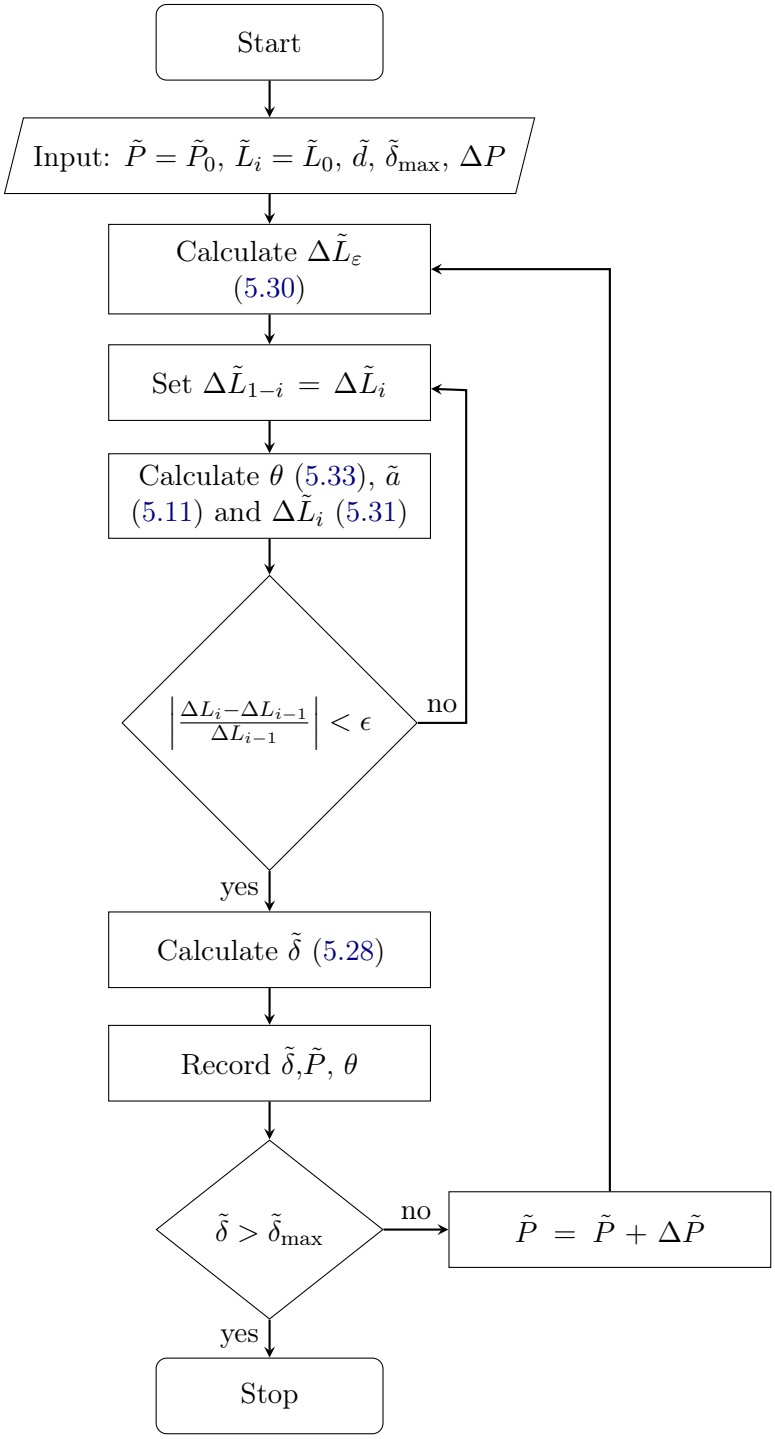


Figure 5.5.: Flow chart for evaluation of the load deflection relations and the boundary rotation for the column buckling with kinematic rotation imperfections due to column shortening.

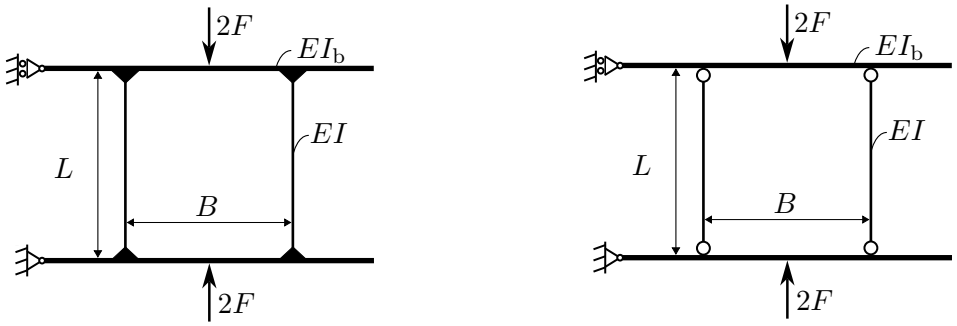


(a) Rigid connection between the elements

(b) Connections allowing for free rotations.

Figure 5.6.: Lattice structures consisting of two vertical columns surrounded by two horizontal beams. A point load $2F$ acts in the center between the columns, so each column is loaded in compression by $F$.

deflection $\delta$ given by Eq. (5.28) are recorded. The process is continued until the normalized maximum midspan deflection $\tilde{\delta}_{\max}$ is reached.

### 5.2.3. Rigidly connected lattice structures

An initially perfect lattice structure can be exposed to kinematic load-dependent rotation imperfections introduced by the deformation of the surrounding elements under the assumption of rigid connections. An example is given by the minimal structural example of two vertical columns connected by two horizontal beams as depicted in Figure 5.6a. The point load $F$ leads to a bending of the two horizontal beams. Under the assumption of rigidly connected elements, the bending of the horizontal beams leads to a boundary rotation of the vertical columns. In contrast, allowing for free rotation in the connection between the elements (see Figure 5.6a), no boundary rotation appears for the vertical columns, preserving their initial perfect structure during the loading process until buckling.

The kinematic load-induced rotation imperfections of the lattice structures can be combined with geometrical imperfections. Considering the geometrical imperfections of a half-sinus wave

$$W_{\mathrm{G}} = A_{\mathrm{G}} \sin\left(\frac{\pi X}{L}\right) \tag{5.34}$$

where $A_{\mathrm{G}}$ is the geometrical imperfection amplitude. As the assumed geometrical imperfection and the rotation imperfections from Eq. (5.8) both take the form of a half sinus wave, the combined imperfection also takes the shape of a half sinus wave, for

which the normalized imperfection amplitude is given by

$$\tilde{\alpha} = \tilde{\alpha}_{\mathrm{W}} + \tilde{A}_{\mathrm{G}}. \tag{5.35}$$

where $\tilde{A}_{\mathrm{G}} \equiv A_{\mathrm{G}}/L$. Even though the two imperfection types can have the same overall shape, their fundamental behavior differs. The geometrical imperfections are a constant imperfection, independent of the boundary condition and the applied load. Such imperfections appear already from the initial configuration as a stress-free deflection. The rotation imperfections are introduced by the connecting elements under the assumption of rigid connections. They can both appear both as a static imperfection or a kinematic load-induced imperfection controlled by the rotation of the confining elements. Such rotation imperfections result in a bending of the column, thereby increasing the bending stresses.

#### 5.2.3.1. Case studies of lattice structures

In Section 4.3, it was shown that boundary rotation imperfections are introduced to the lattice interfaces from the rotation of the surrounding adherend elements, and such rotation imperfections reduce the load-bearing capacity of the interface structure. To further expand the understanding of rotation-induced imperfections, a case study was conducted to evaluate the load-bearing capacity of the lattice structures shown in Figure 5.7. For all analyses, the deformation was limited by a prescribed normalized midspan deflection $|\tilde{\delta}_{\max}|$. The lattice structures are primarily analyzed under the assumption of rigid connections between the individual elements. In addition, initially perfect lattice structures with connections allowing for free rotation where considered (see Figure 5.6). For these pin-jointed configurations, Euler buckling is assumed to define the critical load, as no rotation-induced imperfections are present. Three loading scenarios were investigated: a point-loaded lattice structure (Figure 5.7a), a moment-loaded lattice structure (Figure 5.7b), and a lattice structure subjected to a distributed load (Figure 5.7c). For the point-loaded configuration, an additional geometrical imperfection was introduced, as illustrated in Figure 5.7d. Furthermore, a simple architected interface in the form of a pillar lattice structure was considered (see Figure 5.7e). This architected interface can be analyzed from the lattice structure shown in Figure 5.7c, under the assumption of fixed end rotations of the two horizontal beams.

The solution method for evaluating the critical load under the assumption of rigidly connected elements consists of the following steps:

1. From a free body diagram of the upper beam, the moment resultant $M(x)$ is determined. The origin of the coordinate system is positioned at the connection point to the left column. The contribution from the rigid connection to the vertical columns is given by the sum of the moment required to bend the column according

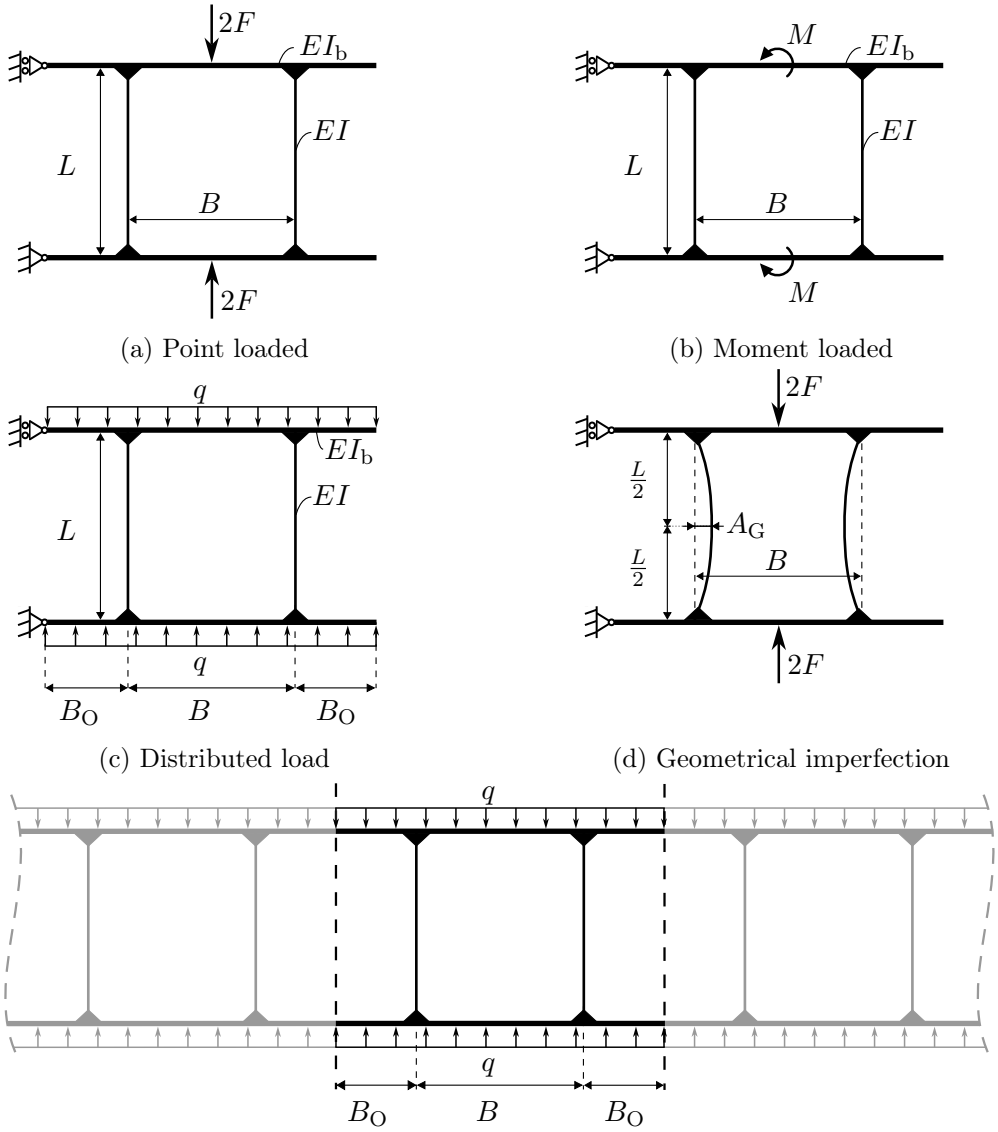


(a) Point loaded

(b) Moment loaded

(c) Distributed load

(d) Geometrical imperfection

(e) Architected interface with distributed load

Figure 5.7.: Overview of the lattice structures considered for the case studies.

to the rotation imperfection (Gere and Goodno, 2013, p. 1050) and the moment introduced by the buckling process $M_\mathrm{B}$ from Eq. (5.26). The sum of moments is given by

$$M_\mathrm{C} = \frac{2\theta EI}{L} + \frac{F\frac{\alpha\pi}{\mu L}}{\left(1-\frac{\pi^2}{L^2\mu^2}\right)\tan\left(\frac{\mu L}{2}\right)} \tag{5.36}$$

2. From the moment resultant $M(x)$, the deflection, $w(x)$, of the upper beam is

Table 5.1.: Overview of the lattice structures with the loading conditions and the corresponding resulting moments and the boundary conditions (BC) and symmetry (SC) conditions used for the analysis.

| Structure | Load | Schematic diagram | $M(x)$ | BC and SC | Compression loading at the columns $F$ |
|---|---|---|---|---|---|
| Point loaded 2 column structure | $2F$ | Figure 5.7a | For $0 < x < \frac{B}{2}$: $Fx + M_\mathrm{C}$ | $w(0) = 0$, $w'(B/2) = 0$ | $F$ |
| Moment loaded 2 column structure | $M$ | Figure 5.7b | For $0 < x < \frac{B}{2}$: $Fx + M_\mathrm{L}$<br>For $\frac{B}{2} < x < B$: $Fx + M_\mathrm{L} + M$ | $w(0) = \frac{F}{k}$, $w(B) = -\frac{F}{k}$ $M_\mathrm{L} = M_\mathrm{C}$ $M_\mathrm{R} = -\frac{2EI}{L} w'(B)$ | $\frac{M - M_\mathrm{R} - M_\mathrm{L}}{B}$ |
| Distributed load 2 column structure | $q$ | Figure 5.7c | $-\frac{q(x+B_\mathrm{O})^2}{2} + \frac{qB_\mathrm{tot}x}{2} + M_\mathrm{C}$ | $w(0) = 0$, $w'(B/2) = 0$ | $\frac{qB_\mathrm{tot}}{2}$ |
| Architected interface | $q$ | Figure 5.7e | For $-B\mathrm{O} < x < 0$: $-\frac{q(x+B_\mathrm{O})^2}{2} + c$<br>For $0 < x < \frac{B}{2}$: $-\frac{q(x+B_\mathrm{O})^2}{2} + \frac{qB_\mathrm{tot}x}{2} + M_\mathrm{C} + c$<br>$c$ is an arbitrary constant | $w(0) = 0$, $w'(B/2) = 0$, $w'(-B_\mathrm{O}) = 0$ | $\frac{qW_\mathrm{tot}}{2}$ |
| Combined rotation and geometrical imperfections | $2F$ | Figure 5.7d | For $0 < x < \frac{B}{2}$: $Fx + M_\mathrm{C}$ | $w(0) = 0$, $w'(B/2) = 0$ | $F$ |

evaluated based on the Euler-Bernoulli beam theory using Eq. (2.42) and the boundary conditions (BC), symmetry conditions (SC), and continuity conditions (CC).

3. The boundary rotation imperfection of the left column boundary is evaluated from the rotation of the connecting beam by $\theta = -w'(0)$. The resulting rotation imperfection is load-dependent and varies as a function of the applied external load.

4. The critical force $F_\mathrm{cr}$ is determined by solving the equation system of Eq. (5.28) and (5.36) while setting the normalized midspan deflection of the column to $\tilde{\delta}_\mathrm{max}$. The imperfection amplitude is given by Eq. (5.35) using the boundary rotation.

The resultant moment for the individual lattice structures and the used boundary and symmetry conditions for solution step 2 are given in Table 5.1. A detailed example is given for the point-loaded lattice structure (see Figure 5.7a). Assuming static equilibrium, no reaction moments are transmitted through the pinned boundaries of the beams, and the system is symmetric with respect to both the horizontal and vertical planes. The vertical displacement of the upper beam does not influence the boundary rotation of the columns and the corresponding midspan deflection, and the beam can be modeled




(a) Schematic representation of the upper beam.

(b) Free body diagram of the upper beam. The reaction forces are depicted in blue.

Figure 5.8.: Representation of the upper beam used for deviation of the critical load under the assumption of a point-loaded structure and rigid connections between the elements.

as a double overhanging beam. The two columns are replaced with a sliding support and a rotational spring at the connection points (see Figure 5.8a). Based on the free body diagram of the upper beam (see Figure 5.8b), the resulting moment at the column boundary is given by

$$M(x) = Fx + M_{\mathrm{C}} \quad \text{for} \quad 0 < x < \frac{W}{2}. \tag{5.37}$$

Using Eq. (2.42), the boundary conditions $w(0) = 0$ and the symmetry condition $w'(W/2) = 0$ the displacement of the upper beam is given by

$$w(x) = \frac{x}{24EI_{\mathrm{b}}} \left(-4Fx^2 + 12M_{\mathrm{C}}x + 3W\left(FW - 4M_{\mathrm{C}}\right)\right), \tag{5.38}$$

where $I_{\mathrm{b}}$ refers to the second moment of area of the beam. The critical loading $F_{\mathrm{cr}}$ is then be determined by combining Eq. (5.28), (5.35), (5.36) and (5.38) and limiting the midspan deflection by $\tilde{\delta}_{\max}$.

For the moment loaded lattice structure (Figure 5.7b), the loading method breaks the symmetry condition. The left column will be exposed to compression loading, while the right column is loaded in tension, so the deflection analysis due to buckling must be performed on the left, compression-loaded column. The elastic shortening/elongation of the column causes the surrounding horizontal beams to rotate. Two axial springs with the spring constant $k = 2EA/L$ (Gere and Goodno, 2013, p.126) are placed at the rigid connection point ($x = 0$, $x = B$) to account for the elastic compression/elongation of the left and right column, respectively. The reaction moment from the left ($M_{\mathrm{L}}$) and right ($M_{\mathrm{R}}$) columns is specified in Table 5.1.

### 5.2.4. Numerical reference model

All analytical results are validated using nonlinear quasi-static finite element analyses performed in COMSOL Multiphysics 6.1. The simulations are conducted in a two-

dimensional space, and geometric nonlinearity is included to capture the buckling process.

The numerical setup depends on the type of imperfection considered. First, the load-deflection response from Eq. (5.28) is analyzed for a compression-loaded column with an initial geometric imperfection in the form of a half sinus wave, as defined in Eq. (5.8). For this case, a stationary study is employed, in which the compressive load is increased incrementally in a stepwise manner. Subsequently, rotation-induced imperfections are investigated. Two configurations are considered: static rotation imperfections applied directly at the column boundaries, as illustrated in Figure 5.2, and kinematic rotation imperfections induced by column shortening, as depicted in Figure 5.4. For both configurations, a pseudo-time parameter is introduced to control the application of both the initial imperfections and loading. First, the initial rotation imperfection ($\theta$ or $d_0$) is applied by a linearly increasing function. Afterwards, the axial load $P$ is increased linearly until a prescribed normalized deflection $\tilde{\delta}$ is reached. For the case studies of the rigidly connected lattice structures from Figure 5.7, a stationary, displacement-controlled analysis is performed. The applied load (point load $F$, moment $M$ or distribute load $q$) is determined implicitly by enforcing the displacement condition

$$\tilde{\delta}(\text{load}) = \tilde{\delta}_{\max}. \tag{5.39}$$

The direction of the imposed displacement is defined based on the analytical predictions, controlled by the direction of the introduced boundary rotation imperfection of the column. To validate the assumed direction, the analysis is repeated by a load-controlled formulation by applying the critical load and comparing the buckling direction of the column.

The dimensions and material properties of the columns are selected according to the study of Harvey and Cain (2020). Each column has a length of $L = 190\,\text{mm}$ and a rectangular cross section with the area $A = t \times b = 2.4\,\text{mm} \times 10\,\text{mm}$, where $t$ denotes the thickness and $b$ the width of the column. Young's modulus of the column material is $E = 3.3\,\text{GPa}$. For each column, 80 beam elements were used for the mesh. A mesh convergence study was conducted to verify the results. The levers shown in Figure 5.4 are modeled as aluminum components with Young's modulus of $E_{\text{lever}} = 70\,\text{GPa}$. A quadratic cross-section of $10 \times 10\,\text{mm}$ is used, resulting in a bending stiffness that is approximately 1500 times higher than that of the column. The length of the lever $L_{\text{lever}} = L$. Each lever is discretized using 14 beam elements. For the case study presented in Figure 5.7, the same material properties and width are used for both the beam and column elements, with $E = 3.3\,\text{GPa}$ and $b = 10\,\text{mm}$. The total beam length is defined as $B_{\text{tot}} = 2L$, and the distance between the columns is set to $B = L$, unless stated otherwise. To vary the stiffness ratio between the beam and columns ($EI_{\text{b}}/EI$), the beam thickness is adjusted while keeping the material properties and all remaining geometric dimensions constant.

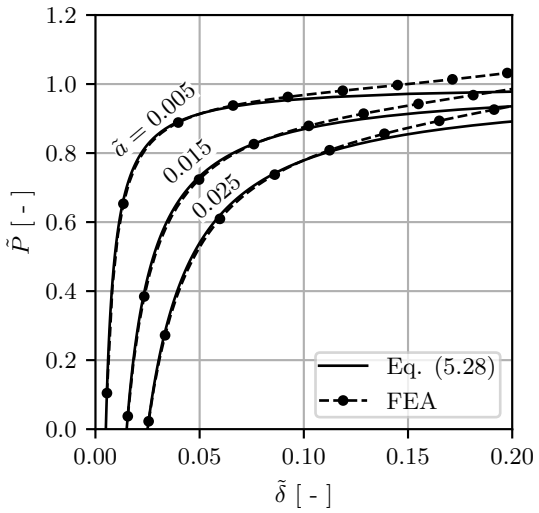


Figure 5.9.: The normalized load-deflection response of the analytical solution of Eq. (5.28) compared to the numerical reference solution. The results are in good agreement for the normalized displacement $\tilde{\delta} < 0.1$

## 5.3. Results and discussion

In the following section, the analytical predictions are evaluated against the numerical reference model.

### 5.3.1. Static imperfections

To evaluate the load-deflection relation of Eq. (5.28), the normalized midspan deflection is compared to the result of the FEA (see Section 5.2.4), considering a geometrical imperfection of a half sinus wave. The relation is evaluated using the normalized amplitudes of $\tilde{a} = 0.005$, 0.015, and 0.025. The results are shown in Figure 5.9. In the range up to $\tilde{\delta} \approx 0.1$, the analytical and numerical solutions are in very good agreement. For example, at $\tilde{\delta} = 0.1$ and $\tilde{a} = 0.005$, the deviation is 1.1 %. As the imperfection amplitude $\tilde{a}$ decreases, the response approaches the solution of the bifurcation problem of the classical Euler buckling with the normalized critical buckling load $\tilde{P} = 1$. This is consistent with established work on buckling behavior for nearly perfect columns (Timoshenko and Gere, 1961; Girão Coelho et al., 2013; Harvey et al., 2019). For larger deflections ($\tilde{\delta} > 0.1$), the numerical solution begins to deviate from the analytical prediction. The nonlinear FEA captures the post-buckling behavior, resembling a pitchfork bifurcation characteristic of the nonlinear buckling responses (Wu et al., 2022). This enables the load $\tilde{P}$ in the numerical model to exceed the Euler buckling load ($\tilde{P} > 1$). For $\tilde{a} = 0.005$

at $\tilde{\delta} = 0.2$, the deviation between the analytical and FEA is increased to 5.4 %. This deviation is expected, as the closed-form solution for the normalized midspan deflection given in Eq. (5.28) is derived under the assumption of small deflections. Nevertheless, the analytical model provides an accuracy within approximately 1% for midspan deflections of up to 10% of the column length ($\tilde{\delta} = 0.1$). This level of accuracy is sufficient for many practical engineering applications.

The static boundary rotation imperfection is evaluated by transforming the boundary rotation into an equivalent imperfection amplitude, using the relations given in Eq. (5.9), (5.11) and (5.15). The normalized midspan deflection considering the three different methods for evaluation of the imperfection amplitude is compared to the numerical reference solution. For the FEA, the boundary imperfection is applied to the column boundary in an initial step prior to the loading step (see Section 5.2.4). The results are shown in Figure 5.10 considering the rotation imperfection values of $\theta = 0.02$, 0.06, and 0.1. The results demonstrate that both the use of $\tilde{\alpha}_{\mathrm{W}}$ (Eq. (5.11)) and $\tilde{\alpha}_{\mathrm{M}}$ (Eq. (5.15)) lead to good agreement between the analytical and numerical solution. Among the two, $\tilde{\alpha}_{\mathrm{W}}$ is in the best agreement with the numerical reference solution. Considering the rotation imperfection of $\theta = 0.02$ at the normalized midspan deflection $\tilde{\delta} = 0.1$ and the transformation method of $\tilde{\alpha}_{\mathrm{W}}$, the deviation between the analytical and numerical result is 1.5 %. Additionally, in the initial state where no load is applied ($\tilde{P} = 0$), representing the imperfection amplitude by $\tilde{\alpha}_{\mathrm{W}}$ leads to an accurate representation of the midspan deflection, as

$$\tilde{\delta}(\tilde{P} = 0) = \tilde{\alpha}_{\mathrm{W}}. \tag{5.40}$$

In contrast, using $\tilde{\alpha}_{\theta}$ as an estimate for the imperfection amplitude results in a significant underestimation of the normalized load. This behavior aligns with the corresponding overestimation of the deflections observed in Figure 5.3.

### 5.3.2. Kinematic imperfections from column shortening

The results for the kinematically controlled rotation imperfections induced by column shortening, described in Section 5.2.2, are presented in this section and compared to the numerical reference solution given by the FEA described in Section 5.2.4. The normalized initial displacements of the lever arms are set to $\tilde{d}_0 = 0.02$, 0.06, and 0.1. The boundary rotation imperfections of the column are shown in Figure 5.11a as a function of the normalized midspan deflection. The analytical prediction of the kinematically induced boundary rotation shows good agreement with the numerical reference solution. The relative error between the analytical and numerical solutions increases with the increasing midspan deflection, as shown in Figure 5.11c. The maximal error is found for $\tilde{d}_0 = 0.02$ at a normalized midspan deflection of $\tilde{\delta} = 0.1$, where the relative error is 1.3 %. The normalized load-deflection relations are presented in Figure 5.11b. For reference, the load-deflection response obtained by neglecting the kinematic effects of column shortening

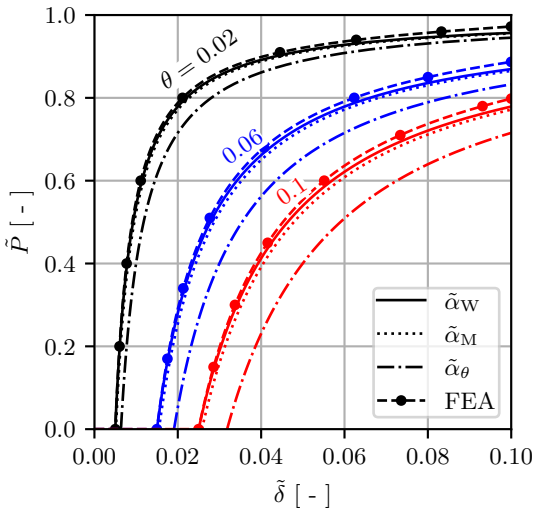


Figure 5.10.: Comparison of the three methods used to transform the boundary rotation imperfection to the imperfection amplitude. The methods are evaluated against the numerical reference solution.

is also shown (dotted line). As expected, the increasing rotation imperfections lead to a reduction in the load-bearing capacity of the structure. Overall, the normalized load-deflection response demonstrates good agreement between the proposed semi-analytical model and the nonlinear numerical reference solution. The relative error between the analytical predictions and the numerical reference results is shown in Figure 5.11d. For small loads, large errors are observed. This is attributed to the steep initial slope of the load–deflection curve, where even a small deviation in the predicted midspan deflection results in large relative errors. In this regime, neglecting column shortening decreases the error. However, as the applied load and corresponding midspan deflection increase, inclusion of the column-shortening-induced rotation imperfection becomes essential for achieving more accurate results. For an initial normalized displacement of $\tilde{d}_0 = 0.02$, the relative deviation at $\tilde{\delta} = 0.1$ is 3.3 % when the kinematic rotation imperfection is included, compared to 6.3 % when the rotation imperfection is neglected.

In the presented structural setup, the initial imperfection and the imperfection due to the column shortening work in the same direction, creating an increasing rotation imperfection throughout the whole loading process. If the direction of either the initial imperfection or the kinematic rotation were reversed, such that the two act in opposition, the column may exhibit snap-through behavior in the process if the imperfection changes direction (Gomez et al., 2017; Radisson and Kanso, 2023).

It should be noted, when applying the initial displacement $d_0$ to the boundary of the lever arm (see Figure 5.4), a reaction force $F$ appears at the other end of the lever, working

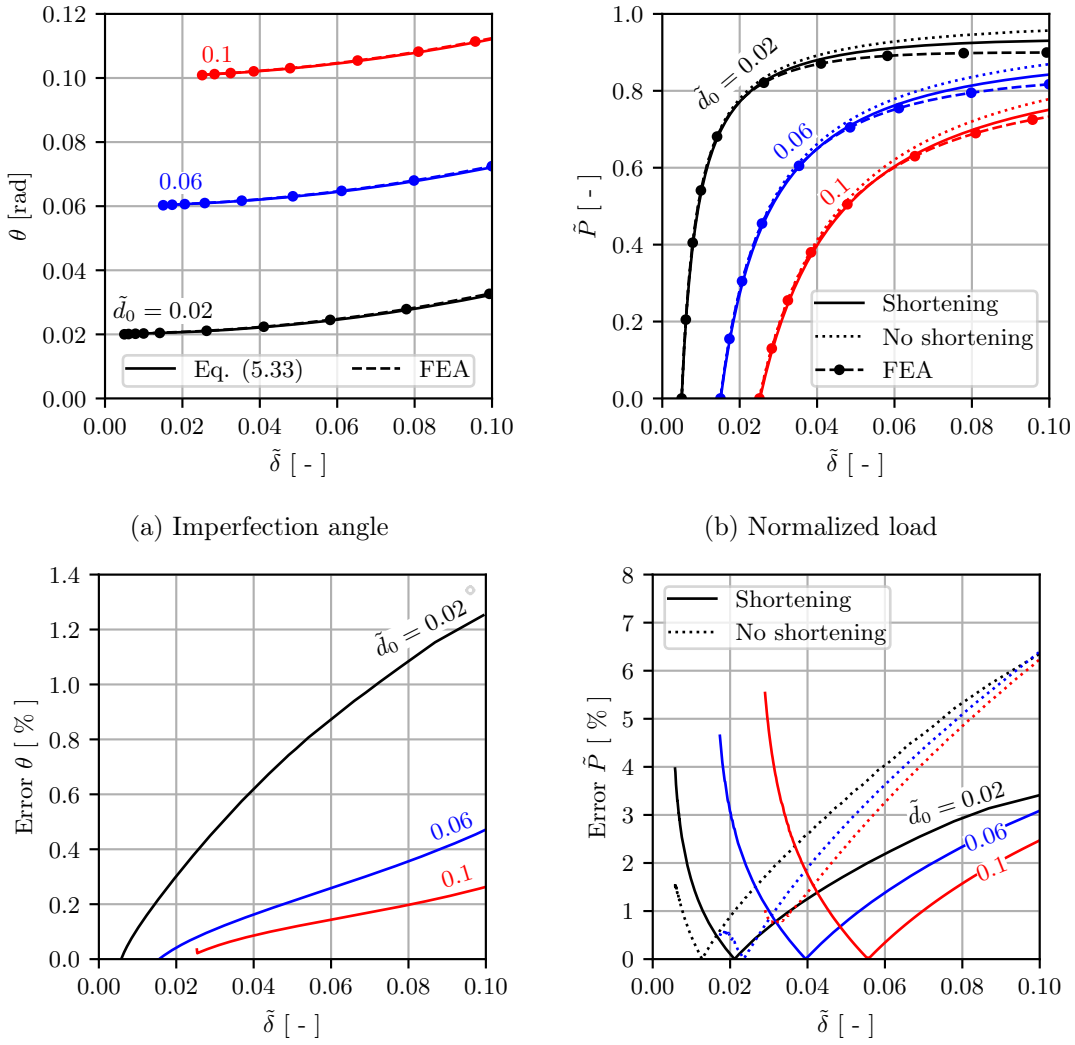


(a) Imperfection angle

(b) Normalized load

(c) Relative error of the boundary rotation

(d) Relative error of the normalized load

Figure 5.11.: Evaluation of (a) the boundary rotation and (b) normalized load-deflection relation of the kinematically controlled rotation imperfection. For reference, the solution neglecting the column shortening is presented for the load-deflection relation. (c) Small relative errors below 1.3% are found for the boundary rotation estimation. (d) Larger errors are obtained for the load-deflection response for small midspan deflection due to the steep load increase. As the midspan deflection is increased, performance using the semi-analytical approach, including the column shortening, is improved.

as a compression force on the column. The column shortening from this reaction force has, in this work, been neglected. To validate this assumption, the magnitude of $F$ is evaluated immediately after the displacement $d_0$ is applied. As the system is in static equilibrium, the moment at the column boundary is given by $M = FL_{\text{lever}}$. Assuming small displacements and neglecting column shortening, the initial boundary rotation of the column is given by (see Eq. (5.12))

$$\theta_{\text{d}} = \frac{FLL_{\text{lever}}}{2EI} \approx \frac{d_0}{L_{\text{lever}}}. \tag{5.41}$$

From this expression, the reaction force can be determined as

$$F \approx \frac{2EId_0}{LL_{\text{lever}}^2}. \tag{5.42}$$

In the presented setup, the lever length is equal to the column height ($L_{\text{lever}} = L$), and a maximum applied displacement of $d_0 = 0.1L_{\text{lever}}$ where considered. This leads to a load ratio of $F/P_{\text{cr}} = 0.005 \ll 1$, for which the force $F$ is significantly smaller than the critical Euler buckling load, so the effect of the reaction force can be neglected. This is in agreement with the relative error approaching zero when the loading is reduced $\tilde{P} \to 0$, and the corresponding midspan deflection approaches the initial imperfection (see Figure 5.11c).

### 5.3.3. Case studies: lattice structures

In the following section, the results for the case study of the rigid connected lattice structures of Figure 5.7 are presented. For the analysis, the maximum midspan deflection $|\tilde{\delta}_{\text{max}}| = 0.04$, for which the corresponding critical loads are evaluated. For reference, the rigid connections between the vertical columns and the horizontal beams were replaced with connections, allowing for free rotations. Under the assumption of such free rotations between the elements, no rotation imperfections are transferred, and the critical load is evaluated from the Euler buckling load of a pinned-pinned column from Eq. (2.58).

#### 5.3.3.1. Point-loaded lattice structure

Figure 5.12 shows the critical load ($F_{\text{cr}}$) of the point-loaded lattice structure with rigid connections (Figure 5.6a). For comparison, the critical load ($F_{\text{Pin}}$) for a system with free-rotating connections (Figure 5.6b) is included. In this latter case, rotation imperfections are eliminated, and the critical load corresponds to the Euler buckling load (see Eq. (2.58)) of a pinned-pinned column, $F_{\text{Pin}} = \pi^2 EI/L^2$. For reference, the Euler buckling load for a clamped-clamped column, $F_{\text{Clamp}} = 4F_{\text{Pin}}$, is also shown. The bending of the

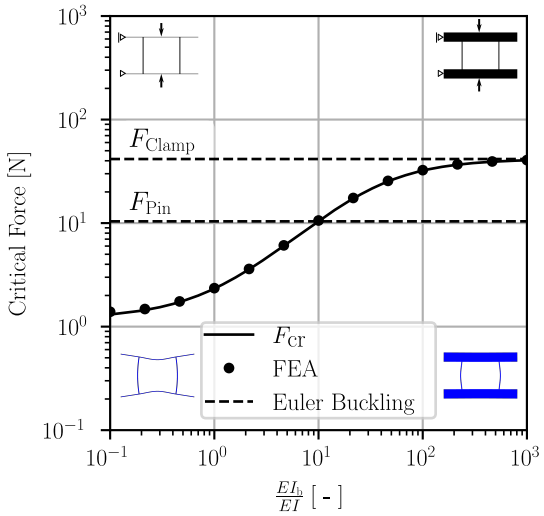


Figure 5.12.: Critical loads for the point-loaded lattice structure. For low stiffness ratios ($EI_b/EI$), the rotation imperfections result in a significant reduction to the load-bearing capacity of the lattice structure under the assumption of rigid connected elements.

horizontal members induces rotations at the connection point between horizontal and vertical elements. In the rigidly connected structure, these rotations are transferred to the columns, introducing kinematic boundary rotation imperfections that reduce the critical load. For low beam-to-column stiffness ratios, these rotation imperfections lead to a significant load reduction, even below the critical load for free-rotating connections when $EI_b/EI < 10$. Take the example of $EI_b/EI = 1$, here the critical load for the rigidly connected structure is $F_{cr} = 2.3\,\text{N}$, which is only 22% of the critical load using free-rotating connections ($F_{\text{Pin}}$). This result is noteworthy, as rigid connections are typically expected to improve structural stability. For the ideal case, the load-bearing capacity is increased by a factor of 4. As the beam-to-column stiffness ratio increases, the deformation of the horizontal members, and thus the induced rotation imperfections, decreases. In the limit of high stiffness ratios ($EI_b/EI \to \infty$), the critical load approaches the ideal value, $F_{cr} \to F_{\text{Clamp}}$.

#### 5.3.3.2. Moment-loaded lattice structure

For the moment-loaded lattice structure (see Figure 5.7b), a similar trend to the point-loaded lattice structure is identified for the critical loading. The critical moments ($M_{cr}$) are plotted in Figure 5.13. In the case of free-rotating connections between the lattices, no moment is transferred to the column boundaries ($M_L = M_R = 0$), and the critical

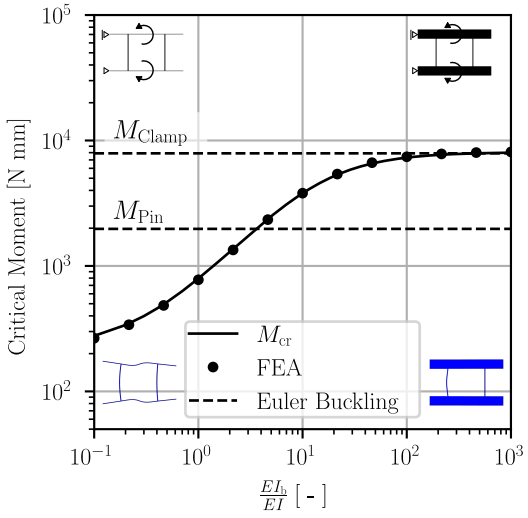


Figure 5.13.: Critical loads for the moment-loaded lattice structure. The induced moment breaks the symmetry of the structure. The boundary rotation imperfections lead to a significant reduction of the critical load for low beam-to-column stiffness ratios.

load is given by $M_{\text{Pin}} = F_{\text{Pin}}B$ (see Table 5.1). For reference, the ideal clamped case $M_{\text{Clamp}} = F_{\text{Clamp}}B$ is also shown. At low beam-to-column stiffness ratios, the rigidly connected system exhibits significantly reduced critical moments compared to the lattice structure with connections allowing for free rotation. However, as the stiffness ratio increases, the induced boundary rotations are diminished, and the critical load of the rigidly connected configuration approaches that of the clamped case ($M_{\text{cr}} \approx M_{\text{Clamp}}$). This behavior is consistent with that observed for the point-loaded lattice structure in Figure 5.12.

Free-rotation connections offer the advantage of eliminating potential rotation imperfections in the lattice structures, thereby simplifying the calculation of the structural load-bearing capacity. However, fixing the rotation at the joints can increase the critical load by up to a factor of four. As demonstrated in the presented case studies, the actual benefit of such rigid connections strongly depends on the interactions between the compression-loaded elements and the surrounding structure. Rigid connections can introduce significant rotation imperfections, which can substantially reduce the load-bearing capacity. This highlights the importance of understanding rotation imperfections in column structures under compressive loading. Even for initially perfect structures, loading can induce rotation imperfections through interaction between the elements. These imperfections are easy to overlook but can have a profound effect on the structural performance of compression-loaded elements. A thorough understanding of these factors is essential for accurately predicting structural behavior and potential failure of lattice structures.

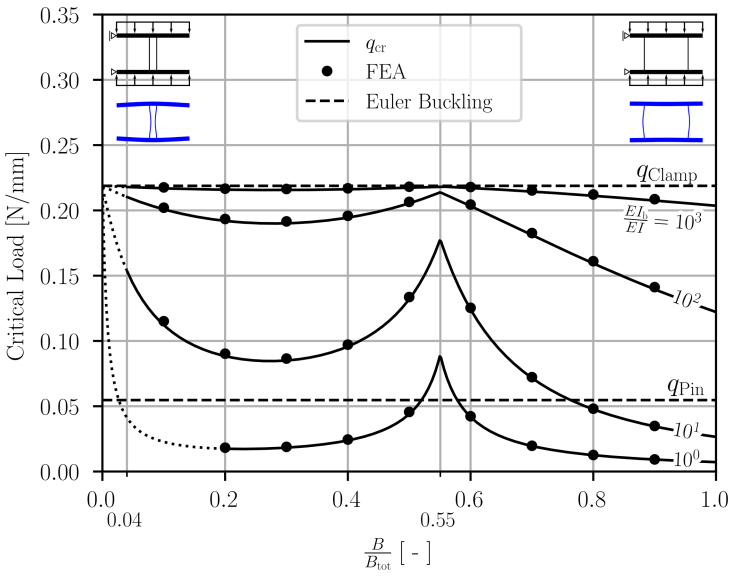


Figure 5.14.: Critical load for lattice structure exposed to a distributed load. The size and direction of the rotation imperfection are dependent on the distance between the vertical columns. A cutoff is introduced at $B/B_{\text{tot}} = 0.04$ due to column overlap.

#### 5.3.3.3. Distributed load on lattice structure

For the lattice structure subjected to a distributed load (see Figure 5.7c), the direction of the rotation imperfection depends on the spacing between the vertical columns ($B$). The corresponding critical load ($q_{\text{cr}}$) is presented in Figure 5.14 for beam-to-column stiffness ratios of $EI_{\text{b}}/EI = \{1, 10, 100, 1000\}$. As for the other presented cases, allowing free rotation at the connections eliminates the boundary rotation imperfections. In this case, the critical load is given by $q_{\text{Pin}} = 2F_{\text{Pin}}/B_{\text{tot}}$, while in the reference case, assuming clamped Euler buckling, the critical loading is given by $q_{\text{Clamp}} = 2F_{\text{Clamp}}/B_{\text{tot}}$. For small values of $B/B_{\text{tot}}$, the vertical columns are located near the center of the structure and deflect toward each other. As $B/B_{\text{tot}} \to 0$, the columns theoretically overlap, and the critical loading converges to that of the ideal clamped–clamped Euler buckling solution, $q_{\text{Clamp}}$. However, an overlap of the columns is not physically possible in the current setup, where the columns must remain separate and free to buckle without contact (Domokos et al., 1997). To enforce this physical constraint, a cut-off is introduced at $B/B_{\text{tot}} = \tilde{\delta}_{\text{max}}$. Note that this cut-off considers only the lateral deflection while neglecting the effect of the column thickness. As $B$ increases, rotation imperfections are introduced to the system, lowering the structure's load-bearing capacity. When $B/B_{\text{tot}} = 0.55$, the imperfection changes sign, leading to a reversal in the buckling direction of the columns. The influence of rotation imperfections is most pronounced for low beam-to-column stiffness ratios. As

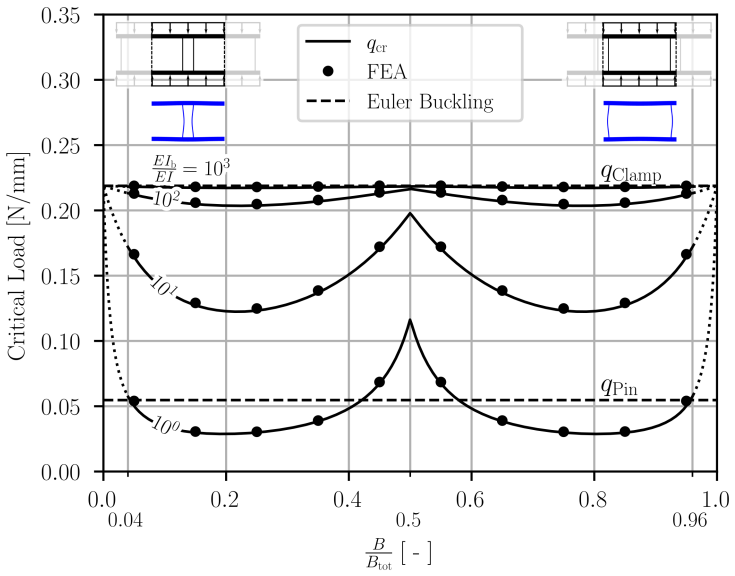


Figure 5.15.: Critical load for the architected interface. The structure shows a symmetric response around $B/B_{\text{tot}} = 0.5$ corresponding to the equally spaced pillar interface. For unequal spacing ($B/B_{\text{tot}} \neq 0.5$), rotation imperfections appear, reducing the load-bearing capacity of the structure.

the stiffness ratio $EI_{\text{b}}/EI$ increases, the deformation of the horizontal elements becomes negligible, and the structural response converges toward the ideal clamped–column case, $q_{\text{Clamp}}$.

#### 5.3.3.4. Distributed load on architected interface

An architected pillar interface was created by repeating the lattice structure exposed to a distributed load, as shown in Figure 5.7e. The critical load of the architected pillar interface is plotted in Figure 5.15 together with the reference values of the critical Euler buckling loading, $q_{\text{Pin}}$ and $q_{\text{Clamp}}$, where the rotation imperfections are excluded. For small values of $B/B_{\text{tot}}$, the behavior resembles that observed for the simple lattice structure exposed to a distributed load (Figure 5.14). In the architected interface, however, the rotation of the representative horizontal beam boundaries is constrained at both ends. As a result, the structural response becomes symmetric around $B/B_{\text{tot}} = 0.5$, where the direction of the buckling deflection reverses. For an equally distributed pillar interface under the defined load case, the rotation imperfections are excluded due to the symmetric loading. But even a small disturbance in the spacing between the pillars results in rotation imperfections and reductions of the load-bearing capacity.

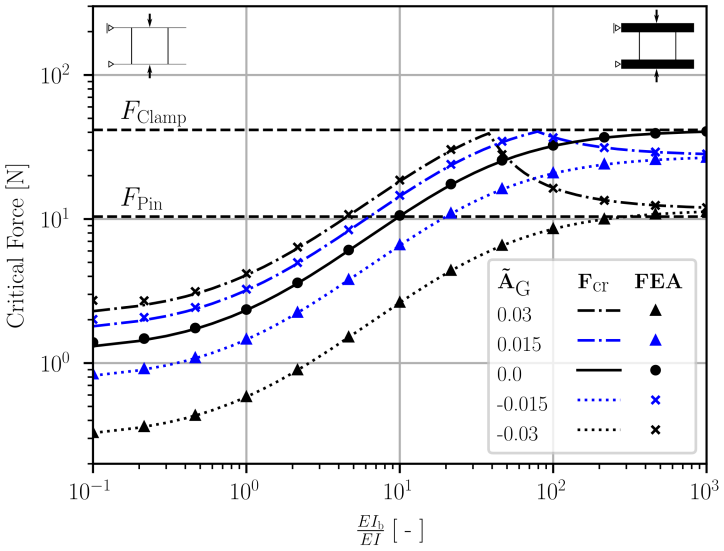


Figure 5.16.: Critical load for the point-loaded lattice structure when including both rotation and geometrical imperfections. The rotation imperfections are dominant for low beam-to-column stiffness ratios. As the stiffness ratio increases, the geometrical imperfections become dominant.

#### 5.3.3.5. Lattice structure with combined geometrical and rotation imperfections

Rotation imperfections can coexist with other types of imperfections. In Figure 5.7d, a geometric imperfection was introduced to the point-loaded lattice structure. The corresponding critical load results are shown in Figure 5.16. For positive values of the geometrical imperfection amplitude $\tilde{A}_G$, the geometric and the rotation imperfections act in opposite directions. At low beam-to-column stiffness ratios, the rotation imperfection dominates, and the column deflection appears in the same direction as the rotation imperfection. As the stiffness ratio increases, the size of the rotation imperfection decreases, and the geometric imperfection becomes dominant, reversing the deflection direction of the column. At a transition point, where the size of the imperfection amplitude of the geometrical and rotation imperfections is equal, the two imperfections cancel out each other, and the critical load approaches the ideal solution of the clamped Euler buckling case ($q_{\text{Clamp}}$). For negative values of $\tilde{A}_G$, the geometrical imperfection works in the same direction as the rotation imperfection, thereby amplifying the total imperfection and further reducing the load-bearing capacity. As the stiffness ratio increases, the influence of the rotation imperfection becomes negligible, and the load-bearing capacities for the positive and negative values of $\tilde{A}_G$ converge.

Geometric imperfections are independent of the surrounding structures and constant throughout the loading process. This is advantageous for analytical calculations, as only

the compression loading is needed for the estimation of the beam deflection, when knowing the initial geometrical imperfection amplitude. For rotation imperfections, the amplitudes are load-dependent and must be evaluated throughout the loading process, when including interactions between the elements. However, as demonstrated in this chapter, neglecting the rotation imperfections can lead to an inaccurate and significant overestimation of the load-bearing capacity. Additionally, rotation imperfections introduced bending to the column and thereby bending stress (see Section 4.3.2), while the geometrical imperfection can be considered an initially stress-free imperfection.

## 5.4. Conclusion

In this chapter, the concept of rotation imperfections was introduced in the form of both static and kinematically load-induced boundary rotation imperfections. By an analytical framework, such rotation imperfections were evaluated for rigid clamped columns and rigid connected lattice structures. Rotation imperfections can lead to a significant decrease in the load-bearing structure. An example was given for a simple, rigidly connected point-loaded lattice structure. Here, the load-bearing capacity was reduced to as low as 22% of the reference structure, allowing for free rotations at the connections between the elements. Rotation imperfections behave fundamentally differently from the often used geometrical imperfections presented in Section 2.4.2. Geometrical imperfections are static imperfections independent of the boundary conditions or loading process. The rotation imperfections can appear as either a static or kinematic load-induced imperfection controlled by the connection elements, requiring the boundary condition to the connecting structure to be rigid. Additionally, the rotation imperfections alter the stress field within the column by increasing the bending stresses. By introducing the concept of rotation imperfections to the confined lattice interfaces presented in Chapter 4, the buckling analysis can be expanded to account for boundary-induced imperfections. Removing the assumption of a perfect buckling response, even under the assumption of initially perfect structures.

# 6. Compression failure of stretching-dominated architected interfaces

*In this chapter, an analytical method for the analysis of buckling in architected lattice interfaces is presented. The model incorporates the concept of imperfections into the evaluation of buckling failure in compression-loaded lattices. Four evaluation points were identified for potential failure onsets, whereas the analysis is reduced to two evaluation points under the assumption of initially perfect structures. For the classical Euler buckling, neglecting all imperfections requires only one evaluation to determine failure of the compression-loaded lattices. While rotation imperfections have the highest impact for high relative densities of the interface, the geometrical imperfections result in a decrease in the load-bearing capacity for all relative densities.*

## 6.1. Introduction

Lattice interfaces are not only relevant in the field of architected interfaces. Foam materials (Gibson and Ashby, 1997), or weak layers in snow (Jamieson and Schweizer, 2000), see Figure 6.1, can also appear as lattice interface materials. In the context of a weak interface in snow, failure can be particularly dangerous when the fast fracture process results in large avalanches (Rosendahl and Weißgraeber, 2020). For both engineered and natural materials, imperfections are inevitable and, under the assumption of slender lattice members, must be incorporated into the damage modes associated with buckling failure (see Section 2.4.2). Athanasiadis et al. (2021) proposed an analytical model to evaluate the failure of architected interfaces using Winkler springs to represent the interface material, and Euler-Bernoulli beam theory for representation of the adherends, see Section 2.6.3 for further details. In this model, compressive failure is assumed to be initiated by Euler buckling, for which all imperfections in the lattice structure are neglected. To extend the understanding of failure mechanisms in architected interfaces, the concept of rotational imperfections introduced in Chapter 5 and geometrical imperfections are incorporated into the analysis of buckling failure. In addition, shear deformation of the adherend material is accounted for by employing Timoshenko beam theory for better representation of adherend material, such as CFRP used for lightweight structures.



Figure 6.1.: Weak interface in snow. The weak layer is less dense, so more light shines through it (Photo: Jakob Schöttner).

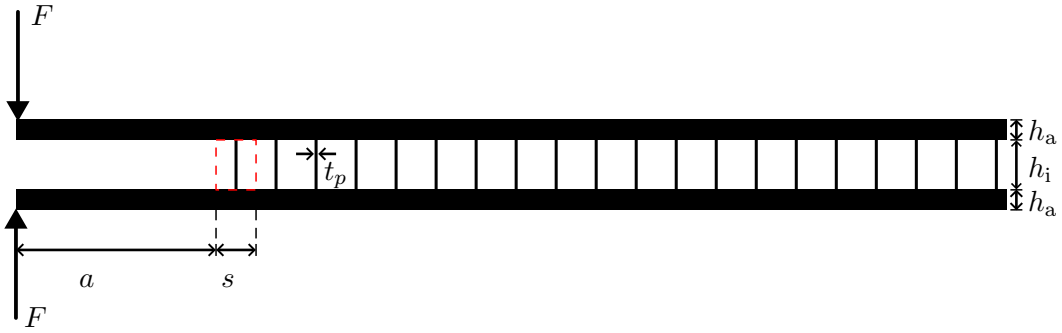


Figure 6.2.: Schematic representation of a DCB with a pillar interface.

## 6.2. Modeling approach

In the present study, a DCB with a pillar interface, represented in Figure 6.2 is investigated. The DCB is loaded by a compression load $F$ on the adherend boundary, corresponding to a mode I- loading. Hence, the interface material experiences a compression zone at the interface front, followed by a tensile zone further along the interface (see Figure 2.12).

### 6.2.1. Adherend deflection and rotation

The adherend material is represented by a Timoshenko beam formulation that includes potential shear effects present in the adherend material (see Section 2.3.2.2). To model the response of the adherends, the pillar interface is represented by a Winkler foundation (see Section 2.6.2). The corresponding spring constant is given by Eq. (2.91), where the material modulus of the pillar interface is given by Eq. (4.6). Furthermore, the symmetry in the $x$-$y$ plane is utilized, for which only the upper adherend is considered. Figure 6.3 provides a representation of the upper adherend. The adherend is separated into two parts:

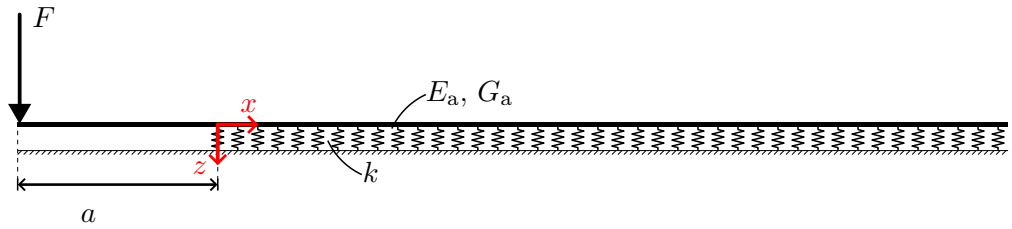


Figure 6.3.: Representation of the adherend resting on the Winkler foundation. Due to symmetry, only the upper half of the DCB is modeled.

the free part of the adherend ($-a \leq x \leq 0$) and the adherend resting on the Winkler foundation ($x > 0$). Assuming the interface section is sufficiently long, the deflection and rotations of the right-most end ($x \to \infty$) are assumed to be zero.

First, the deflection and rotation of the free part of the adherend ($-a \leq x \leq 0$) are evaluated. From the Timoshenko beam theory, the stress resultants are given by Eq. (2.35) to (2.37). As the axial loading is zero, only the stress resultants for the shear force and bending moment are relevant. Using the boundary conditions at $x = -a$ where the shear force $Q(-a) = -F$ and moment $M(-a) = 0$, the stress resultants is given by

$$Q = -F \qquad \text{if } -a \leq x \leq 0, \tag{6.1}$$

$$M = -F(x + a) \qquad \text{if } -a \leq x \leq 0. \tag{6.2}$$

From the coupled system of the governing ODEs given by Eq. (2.38) and (2.39), the rotation and deflection of the free part of the adherend are derived

$$\phi = -\frac{Fx^2}{2D_a} - \frac{Fax}{D_a} + c_1 \qquad \text{if } -a \leq x \leq 0, \tag{6.3}$$

$$w = \frac{Fx^3}{6D_a} + \frac{Fax^2}{2D_a} - x\left(\frac{F}{C_a} + c_1\right) + c_2 \qquad \text{if } -a \leq x \leq 0, \tag{6.4}$$

where $D_a = E_a I_a$ and $C_a = \kappa G_a A_a$ is the bending stiffness and shear stiffness of the adherend, while $c_1$ and $c_2$ are two arbitrary constants.

Secondly, the bending and rotation of the adherend resting on the Winkler foundation ($x > 0$) is considered. The coupled system of governing ODEs for a Timoshenko beam given by (Xia, 2022)

$$-D_a\phi'' + C_a(w' + \phi) = 0 \qquad \text{if } x > 0, \tag{6.5}$$

$$C_a(w' + \phi)' - kw = -q \qquad \text{if } x > 0. \tag{6.6}$$

Since no external loading is present in this section ($q = 0$), the governing ODEs can be

rewritten as

$$w'''' - \frac{k}{C_\mathrm{a}} w'' + \frac{k}{D_\mathrm{a}} w = 0 \qquad \text{if } x > 0, \tag{6.7}$$

$$\phi = -\frac{D_\mathrm{a}}{C_\mathrm{a}} w''' + \frac{D_\mathrm{a} k - C_\mathrm{a}^2}{C_\mathrm{a}^2} w' \qquad \text{if } x > 0. \tag{6.8}$$

To solve the fourth-order homogeneous differential equation of Eq. (6.7), the characteristic equation is established

$$m^4 - \frac{k}{C_\mathrm{a}} m^2 + \frac{k}{D_\mathrm{a}} = 0 \tag{6.9}$$

with the four solutions

$$m = \pm\sqrt{\frac{k}{2C_\mathrm{a}} \pm \sqrt{\frac{k^2}{4C_\mathrm{a}^2} - \frac{k}{D_\mathrm{a}}}}, \quad m = \pm\sqrt{\frac{k}{2C_\mathrm{a}} \mp \sqrt{\frac{k^2}{4C_\mathrm{a}^2} - \frac{k}{D_\mathrm{a}}}}. \tag{6.10}$$

Specifying the characteristic parameter

$$\Omega = \frac{k^2}{4C_\mathrm{a}^2} - \frac{k}{D_\mathrm{a}} < 0, \tag{6.11}$$

then, the deformation of the adherend is assumed to be dominated by bending. Under this condition, the solutions of the characteristic equation can be rewritten as

$$m = \pm\alpha \pm i\beta, \quad m = \pm\alpha \mp i\beta, \tag{6.12}$$

where

$$\alpha = \sqrt{\sqrt{\frac{k}{4D_\mathrm{a}}} + \frac{k}{4C_\mathrm{a}}}, \quad \beta = \sqrt{\sqrt{\frac{k}{4D_\mathrm{a}}} - \frac{k}{4C_\mathrm{a}}}. \tag{6.13}$$

And the general solution of Eq. (6.7) are then given by (Kreyszig et al., 2011, p. 115):

$$w(x) = e^{-\alpha x}\left(C_3 \cos\beta x + C_4 \sin\beta x\right) + e^{\alpha x}\left(C_5 \cos\beta x + C_6 \sin\beta x\right) \quad \text{if } x > 0, \tag{6.14}$$

where $c_3$ to $c_6$ are arbitrary constants. To fulfill the boundary conditions $w(x \to \infty) = 0$ and $\phi(x \to \infty) = 0$ the constant $c_5 = c_6 = 0$.

The four remaining undefined constants in Eq. (6.4) and (6.14) are determined from the continuity condition at $x = 0$, considering the deflection, bending rotation, bending moment, and shear force. The deflections are evaluated using Eq. (6.4) and (6.14) and the bending rotation is evaluated using Eq. (6.3) and (6.8). The corresponding bending moment at shear force is given by Eq. (2.34) and Eq. (2.33) respectively. The results are normalized by the following relations $\tilde{F} \equiv (F\lambda^3)/(D_\mathrm{a} h_\mathrm{i})$ from Eq. (2.95), $\tilde{a} \equiv a/\lambda$, $\tilde{w} \equiv w/h_\mathrm{i}$, $\tilde{h}_\mathrm{i} \equiv h_\mathrm{i}/\lambda$ and $\tilde{x} \equiv x/\lambda$, where $\lambda = (4D_\mathrm{a}/k)^{1/4}$ is the characteristic wavelength

from Eq. (2.90). Separating the adherend in the free section ($-\tilde{a} \leq \tilde{x} \leq 0$) a the section resting on the Winkler foundation ($\tilde{x} > 0$), the normalized adherend deflection

$$\tilde{w}(\tilde{x}) = \frac{\tilde{F}}{2} \times \begin{cases} \text{if } -\tilde{a} \leq \tilde{x} \leq 0\text{:} \\ \tilde{a} + \sqrt{1+\gamma} + \tilde{a}\tilde{x}^2 - \tilde{x}\left(2\tilde{a}\sqrt{1+\gamma} + 2\gamma + 1\right) + \frac{\tilde{x}^3}{3}, \\ \\ \text{if } \tilde{x} > 0\text{:} \\ e^{-\tilde{x}\sqrt{1+\gamma}}\left(\left(\tilde{a} + \sqrt{1+\gamma}\right)\cos\left(\tilde{x}\sqrt{1-\gamma}\right) - \frac{\tilde{a}\sqrt{1+\gamma}+\gamma}{\sqrt{1-\gamma}}\sin\left(\tilde{x}\sqrt{1-\gamma}\right)\right), \end{cases} \tag{6.15}$$

and the rotation

$$\phi(\tilde{x}) = \frac{\tilde{F}\tilde{h}_{\mathrm{i}}}{2} \times \begin{cases} \text{if } -\tilde{a} \leq \tilde{x} \leq 0\text{:} \\ 2\tilde{a}\sqrt{1+\gamma} + 1 - \tilde{x}(2\tilde{a} + \tilde{x}), \\ \\ \text{if } \tilde{x} > 0\text{:} \\ e^{-\tilde{x}\sqrt{1+\gamma}}\left(\left(2\tilde{a}\sqrt{\gamma+1} + 1\right)\cos\left(\tilde{x}\sqrt{1-\gamma}\right) - \frac{\left(2\tilde{a}\gamma+\sqrt{\gamma+1}\right)\sin\left(\tilde{x}\sqrt{1-\gamma}\right)}{\sqrt{1-\gamma}}\right). \end{cases} \tag{6.16}$$

where the parameter $\gamma$ determines the effect due to the shear in the adherend, and is given by

$$\gamma = \frac{\sqrt{kD_{\mathrm{a}}}}{2C_{\mathrm{a}}}. \tag{6.17}$$

The limit $\Omega < 0$ can be rewritten to $\gamma < 1$. When the shear deformation of the beam is neglected ($C_{\mathrm{a}} \to \infty$), then $\gamma \to 0$ and the solution is reduced to the Euler–Bernoulli beam solution for the adherend.

### 6.2.2. Failure of the pillar interface

The failure of the interface can occur within either the compression or tension zone. The critical normalized force is defined as the minimum normalized force that result in failure of the interface, in either the compression zone ($\tilde{F}_{\mathrm{CT}}$) or tension zone ($\tilde{F}_{\mathrm{TZ}}$), such that the normalized critical force

$$\tilde{F}_{\mathrm{c}} = \min\left(\tilde{F}_{\mathrm{TZ}}, \tilde{F}_{\mathrm{com}}\right). \tag{6.18}$$

In Figure 6.4, an example of the normalized rotation and deflection of the adherend is given. Be aware that the positive direction of the vertical axis is downwards. The compression zone appears in the area where deflection is positive ($\tilde{w} > 0$), while the tensile zone is determined by the negative deflection ($\tilde{w} < 0$). The transition point between the compression and tensile zones is found by setting $\tilde{w} > 0$ (see Eq. (6.15)), for the deflection

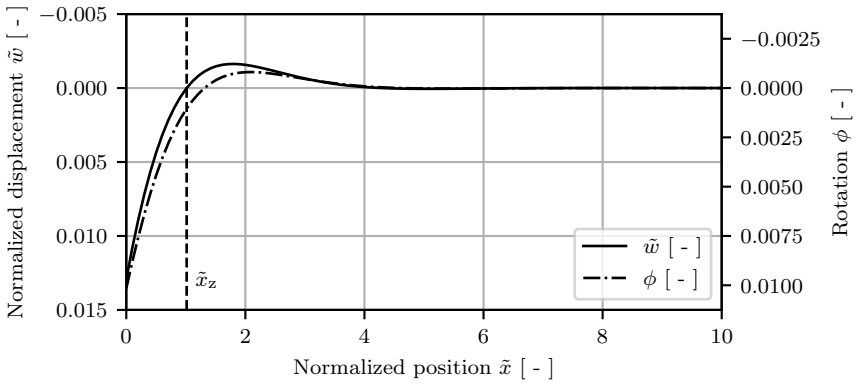


Figure 6.4.: Deflection and rotation example of the adherend for $\tilde{F} = 0.01$, $\tilde{a} = 1.54$, $\tilde{h}_\mathrm{i} = 0.48$ and $\gamma = 0.09$ .

at the interface section where $\tilde{w} > 0$. The transition point is given by

$$\tilde{x}_\mathrm{Z} = \frac{\arctan\left(\frac{(\tilde{a}+\sqrt{1+\gamma})\sqrt{1-\gamma}}{\tilde{a}\sqrt{1+\gamma}+\gamma}\right)}{\sqrt{1-\gamma}}. \tag{6.19}$$

While neglecting the shear effect ($\gamma = 0$) the transition point is limited to the area of $\pi/4 < \tilde{x} < \pi/2$, so the compression zone size ($0 \leq x < x_Z$) is in the order of the wavelength $\lambda$. When including the shear effect, the zone sizes are increased.

#### 6.2.2.1. Failure of the compression zone

For the pillars placed in the compression zone ($\tilde{x} < \tilde{x}_\mathrm{Z}$), each pillar of the interface is exposed to a compression load and a boundary rotation (see Figure 6.4). From the evaluation of $\tilde{w}$ and $\phi$, the largest value of both the compression load and boundary rotation is found at the first pillar of the interface placed at $x_p = s/2$. The corresponding adherend deflection and rotation of this pillar are given by $w_p = w(x_p)$ and $\phi_p = \phi(x_p)$, respectively. When evaluating the compression load of the pillars, the load corresponds to the compression load on the Winkler foundation. As only one pillar is positioned at each unit cell of the interface, the compression load on the pillar

$$P \approx 2ksw_p. \tag{6.20}$$

Inserting the spring constant for the interface (Eq. (2.91)), using the material modulus for a pillar interface (Eq. (2.91)) and normalizing the load by the critical Euler buckling

load (Eq. (2.58)), the normalized load on the pillar is given by

$$\tilde{P} = \frac{P}{P_{cr}} = \frac{6}{\pi^2}\frac{\tilde{w}_p}{\tilde{t}_p^2} \tag{6.21}$$

where $\tilde{t}_p \equiv \frac{t_p}{h_\mathrm{i}}$ is the normalized pillar thickness.

The rotation imperfections consist of two parts. From the assumption of a fixed connection between the adherend and the pillar boundary, the bending rotation of the adherend, $\phi_p$, is transferred to the pillar boundary, introducing a rotation imperfection to the pillar. The corresponding normalized imperfection amplitude, using the transformation of Eq. (5.11) is given by

$$\tilde{\Theta}_F = \frac{\phi_p}{4}. \tag{6.22}$$

The imperfection amplitude is proportional to the applied load ($\tilde{\Theta}_F \propto F$), increasing the imperfection during the loading process. From a manufacturing perspective, perfect structures never exist, and imperfections will be present already from the initial state. Here, the initial imperfection of the pillar interface is assumed to take the form of a half sinus wave (see Eq. (5.34)) with the amplitude $\Theta_G$. The geometrical imperfection is present in the initial state and remains constant during the loading process. The total normalized imperfection is given by

$$\tilde{\Theta} = \tilde{\Theta}_F(F) + \tilde{\Theta}_G. \tag{6.23}$$

The normalized deflection $\tilde{W}$ of the pillar in relation to the perfect straight structure is given by Eq. (5.27), considering $\tilde{\Theta}$ for the normalized imperfection amplitude. For which the deformation of the pillar from the applied load $F$ is given by

$$\tilde{W}_F = \tilde{W} - \tilde{\Theta}_G \sin\left(\pi\tilde{X}\right). \tag{6.24}$$

The pillar is assumed to fail when the strain at any point within the pillar exceeds the critical value of the material. As the interface pillars are exposed to bending, the strain varies over the cross-section. Under the assumption of an elastic-brittle material, the failure is evaluated both from the maximal tension and compression strain over the cross-section (Gibson and Ashby, 1997). To evaluate the strain, the strain is separated into the contribution of the axial strain $\varepsilon_\mathrm{a}$ and the maximal bending strain on the pillar edge $\varepsilon_b$. From the symmetric cross-section around the bending axis, the absolute value of the tension and compression strain is equal. Combining the bending and axial strain, the maximum and minimum strain over the cross-section is given by

$$\varepsilon_\mathrm{min} = \varepsilon_\mathrm{a} - \varepsilon_b \tag{6.25}$$

$$\varepsilon_\mathrm{max} = \varepsilon_\mathrm{a} + \varepsilon_b. \tag{6.26}$$

The pillar is assumed to fail when the critical value of the material strain in either tension or compression is reached, such that failure occurs when

$$\varepsilon_{\min} \leq \varepsilon_{\text{com}}, \tag{6.27}$$

$$\varepsilon_{\max} \geq \varepsilon_{\text{ten}}. \tag{6.28}$$

The compression strength of brittle materials is about ten times larger than the tensile strength (Gibson and Ashby, 1997, p. 70), so in many structural cases, the failure is limited by the tensile strength. In this specific case of compression loading of a pillar, tension stresses are introduced from the bending of the pillar due to buckling, while the loading of the pillar is compression. Therefore, the possibility of compression failure can not be neglected.

The axial strain from the compression of the pillar is given by

$$\varepsilon_{\text{a}} = -\frac{2w_p}{h_{\text{i}}} = -\frac{\pi^2}{3}\tilde{P}\tilde{t}_p^2 \tag{6.29}$$

and the maximal bending strain over the cross-section is given by

$$\varepsilon_b = \frac{t_p}{2}\left|\frac{\mathrm{d}^2 W_F}{\mathrm{d}X^2}\right|. \tag{6.30}$$

Three local maxima exist for $\varepsilon_b$ over the pillar length: at $\tilde{X} = 0$, $\tilde{X} = 1/2$, and $\tilde{X} = 1$. However, due to symmetry, the absolute strain at the two boundary points is equal, so only the strain values at $\tilde{X} = 0$, $\tilde{X} = 1/2$ need to be evaluated. The bending strain values at the pillar boundary and midpoint are, respectively, given by

$$\varepsilon_{\text{b},0} = \frac{\pi^2 \tilde{t}_p}{2(1-4\tilde{P})} \frac{8\tilde{P}^{3/2}|\tilde{\Theta}|}{\tan\left(\pi\sqrt{\tilde{P}}\right)}, \tag{6.31}$$

$$\varepsilon_{\text{b},1/2} = \frac{\pi^2 \tilde{t}_p}{2(1-4\tilde{P})} \left|\tilde{\Theta} - \tilde{\Theta}_G(1-4\tilde{P}) - \frac{8\tilde{\Theta}\tilde{P}^{3/2}}{\sin\left(\pi\sqrt{\tilde{P}}\right)}\right|. \tag{6.32}$$

To evaluate the position of failure at the pillar, a bending strain ratio is defined by

$$\bar{\varepsilon}_{\text{b}} \equiv \frac{\varepsilon_{\text{b},1/2}}{\varepsilon_{\text{b},0}} = \frac{(1+g(4\tilde{P}-1))\tan\left(\pi\sqrt{\tilde{P}}\right)}{8\tilde{P}^{3/2}} - \frac{1}{\cos\left(\pi\sqrt{\tilde{P}}\right)}. \tag{6.33}$$

where $g = \tilde{\Theta}_G/\tilde{\Theta}$ represents the fraction of the total imperfection associated with the geometrical imperfection.

The critical load of the compression zone $F_{\text{CZ}}$ is defined as the minimum applied load,

leading to failure initiation in the compression zone, satisfying either Eq. (6.27) or Eq. (6.28). The equations are solved in Wolfram Mathematica using the root-finding method based on Newton's method (Wolfram Research), with an initial guess of $0.9F_{\mathrm{E}}$ and the solution is limited to the solution range $[0,F_{\mathrm{E}}]$, where $F_{\mathrm{E}}$ is the loading introducing the Euler buckling load to the pillar under the assumption of no imperfections. It is given by Eq. (6.21), when letting $\tilde{P} = 1$.

#### 6.2.2.2. Failure of the tension zone

The failure of the tension zone is evaluated based on the maximal axial tensile strain in the pillar. The position of the maximal axial tensile strain $\tilde{x}_{\mathrm{TZ}}$ is found by minimizing the beam deflection by evaluating $\mathrm{d}\tilde{w}/\mathrm{d}\tilde{x} = 0$. The critical strain is reached when

$$-2\tilde{w}(\tilde{x}_{\mathrm{TZ}}) = \varepsilon_{\mathrm{ten}}, \tag{6.34}$$

resulting in a normalized critical force of

$$\tilde{F}_{\mathrm{TZ}} = \frac{\varepsilon_{\mathrm{ten}} \mathrm{e}^{\tilde{x}_{\mathrm{TZ}}\sqrt{\gamma+1}}}{\frac{\tilde{a}\sqrt{\gamma+1}+\gamma}{\sqrt{1-\gamma}} \sin\left(\sqrt{1-\gamma}\tilde{x}_{\mathrm{TZ}}\right) - \left(\tilde{a}+\sqrt{\gamma+1}\right)\cos\left(\sqrt{1-\gamma}\tilde{x}_{\mathrm{TZ}}\right)}. \tag{6.35}$$

### 6.2.3. Numerical reference model

A numerical reference model was set up in COMSOL Multiphysics 6.2 by a finite element analysis in a 2D environment, including geometric nonlinearity. The model is represented in Figure 6.5. Both the adherend and the interface are represented using Timoshenko beam elements. Three elements were used to represent the free beam of the adherend, and for the rest of the adherend, one element was used between each connection point to the interface. For each pillar lattice, 80 elements were used to capture the response of the buckling deformation. The dimensions of the DCB (see Figure 6.2) are given by the adherend height $h_{\mathrm{a}} = 5\,\mathrm{mm}$, the interface height $h_{\mathrm{i}} = 12.5\,\mathrm{mm}$ and the width of the DCB is 5 mm. The initial crack length $a = 8h_{\mathrm{a}}$, the length of the interface section $L_{\mathrm{i}} = 10\lambda$. The pillars were placed at a distance $s = 10\,\mathrm{mm}$. For the adherend material, a CFRP UD laminate is considered with Young's modulus $E_{\mathrm{a}} = 150\,\mathrm{GPa}$ and the shear modulus $G_{\mathrm{a}} = 6\,\mathrm{GPa}$ (de Morais et al., 2002). For the solid material of the interface, TMPTA was considered where the material modulus $E_s = 430\,\mathrm{MPa}$, the Poisson's ratio $\nu_s = 0.3$, and strength $\sigma_{\mathrm{c}} = 11\,\mathrm{MPa}$ (Shaikeea et al., 2022). The critical strain in tension $\varepsilon_{\mathrm{ten}} = \sigma_{\mathrm{c}}/E_{\mathrm{s}}$ and in compression $\varepsilon_{\mathrm{com}} = -10\varepsilon_{\mathrm{ten}}$ (Gibson and Ashby, 1997). The left boundary of the lower adherend was fixed in the displacement directions, and a displacement $\Delta$ was applied on the boundary of the upper adherend, for which the reaction force corresponds to $F$. To evaluate the interface damage, the displacement $\Delta$ was increased in steps, with

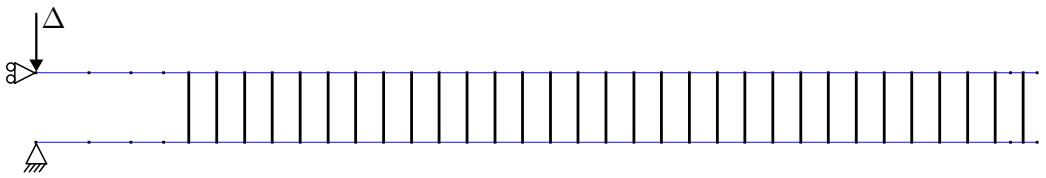


Figure 6.5.: Mesh and boundary conditions for the numerical setup. 80 elements are used for each interface lattice.

the damage of the interface evaluated at each step. The displacement was increased until a maximum displacement of $3\Delta_c$ where $\Delta_c$ is given by Eq. (4.9), or until the solution becomes unstable due to small gaps between the adherend boundaries at displacement values of 10.7 mm. When the critical strain of an interface element was reached, the modulus was reduced by the factor $k = 10^9$. The critical force is defined as the load at damage initiation of the interface material, and is determined by the maximum force. The convergence was checked for the mesh size and the step size of the displacement increase.

## 6.3. Results and discussion

The results presented here are based on a DCB setup using the geometry and material parameters described in Section 6.2.3. A parametric study is performed for the density range of $\tilde{\rho} \in (0.5,2.5)$. The corresponding shear factor $\gamma$ is between 0.046 and 0.10, which satisfies the condition $\gamma < 1$ for which the presented analytical solution is valid. The characteristic wavelength $\lambda$ is between 24.5 mm to 36.7 mm. As the distance between the pillars $s = 10$ mm, a minimum of two pillars are positioned in the compression zone.

### 6.3.1. Critical strain position

In Figure 6.6, the bending strain ratio from Eq. (6.33) is depicted for different fractions of the geometrical imperfections. The bending strain ratio determines the location at which the maximum bending strain occurs. When this ratio exceeds unity, the maximum strain is governed by $\varepsilon_{b,1/2}$, whereas for ratios below unity the critical strain is given by $\varepsilon_{b,0}$. The bending strain ratio decreases with increasing values of the geometrical imperfection fraction $g$, leading to a shift in the location of the maximum bending strain. The lower reference curve, corresponding to $g = 1$, is only valid in the absence of external loading ($\tilde{P} = 0$) and therefore serves as a cutoff. The boundary rotation imperfection $\tilde{\Theta}_F \propto F$, letting the total imperfection $\tilde{\Theta}$ increase during the loading process (see Eq. (6.23)). As $\tilde{\Theta}_G$ remains constant, the value of $g$ is decreasing during the loading process. In the

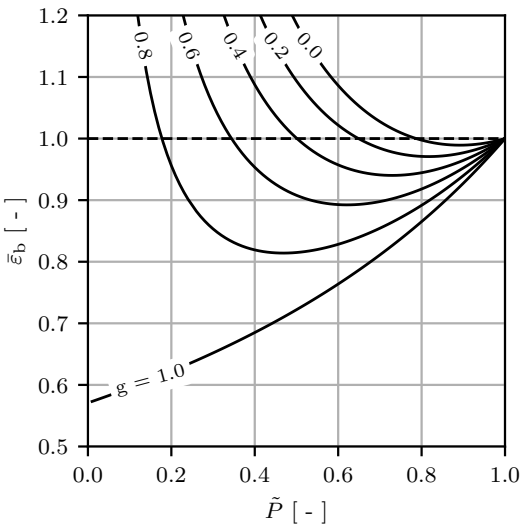


Figure 6.6.: Bending strain for different values of $g$

special case of no geometrical imperfection ($g = 0$), the bending strain $\varepsilon_{b,1/2}$ is dominant up to the transition point of $\tilde{P} = 0.79$, where afterwards the bending strain ratio $\bar{\varepsilon}_b \approx 1$. In this case ($g = 0$), evaluating the bending strain by $\varepsilon_{b,1/2}$ for all values of $\tilde{P}$ gives a maximal error of $\approx 1\%$ and will in many cases be sufficient. However, when a geometrical imperfection is present, the potential failure in both evaluation points must be considered.

### 6.3.2. Critical load for initially perfect interfaces

In Figure 6.7, the normalized critical loads of both tension and compression failure are represented for an initial perfect interface structure ($g = 0$). As shown for the present setup, the normalized critical force of the compression zone ($\tilde{F}_{CZ}$) is, for the full relative density range, lower than that of the tensile zone ($\tilde{F}_{TZ}$), whereas the failure process appears in the compression zone of the interface. From the assumption of an initially perfect structure, the damage position in the compression zone is assumed at $\tilde{X} = 1/2$ (see Section 6.3.1) where the bending strain is given by Eq. (6.32). The damage of the compression zone is reached when either the maximum strain (Eq. (6.26)) or the minimum strain (Eq. (6.25)) reaches the critical strain. For the present setup, the damage is initiated by the maximum strain with the corresponding critical load $\tilde{F}_{CZ}(\varepsilon_{max})$ for the selected range of relative densities.

For comparison of the different failure modes in compression, the ratio $\tilde{F}/\tilde{F}_{CZ}(\varepsilon_{max})$ is depicted in Figure 6.8, where $\tilde{F}$ corresponds to the critical force of the failure mode. The

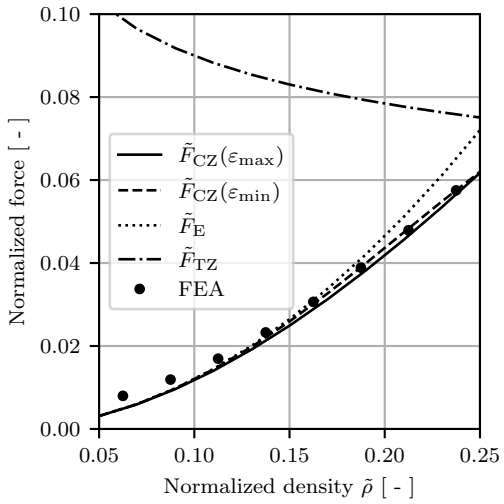


Figure 6.7.: Normalized critical force for different failure modes and the numerical results.

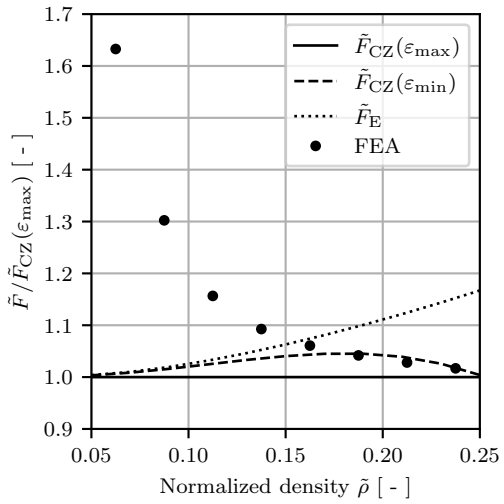


Figure 6.8.: Load ratio, comparing the critical load of the failure modes to the critical load of the DCB.

normalized critical load is validated by the numerical reference model. For higher relative densities, the models are in good agreement with a relative error of 1.7% of $\tilde{F}/\tilde{F}_{\mathrm{CZ}}(\varepsilon_{\max})$ compared to the numerical reference solution for $\tilde{\rho} = 0.24$. However, for low values of $\tilde{\rho}$, the models start to deviate (see Figure 6.8). With a decreasing density, the lattice becomes more slender, decreasing the bending stresses in the lattice (Eq. (6.30)). For these low relative density interfaces, larger deflections are required for crack initiation, and significant buckling deflections are observed for multiple lattices of the interface front, an example is given in Figure 6.9. The large deflections due to buckling result in a softening of the interface (Ye et al., 2021), which appears on the load-deflection plot as an increase in the compliance when reaching $\tilde{F}/\tilde{F}_{\mathrm{CZ}}(\varepsilon_{\max}) \approx 1$. The softening of the interface results in a significant increase in the load-bearing capacity before failure of the first lattice appears (see Figure 6.10). As the analytical models are built on a linear relation of the Winkler foundation, the softening of the interface is not captured by this model, leading to an underestimation of the critical force $\tilde{F}_{\mathrm{CZ}}(\varepsilon_{\max})$ for low relative densities of the interface.

For reference, the critical load $\tilde{F}_{\mathrm{E}}$ due to Euler buckling is depicted, neglecting both rotation and geometrical imperfections, so the interface is assumed to be pure stretching-dominated. Comparing the critical load due to Euler buckling to the critical load $\tilde{F}_{\mathrm{CZ}}(\varepsilon_{\max})$, it is shown that the difference between the two solutions increases with an increasing relative density of the interface (see Figure 6.8). For a relative density of $\tilde{\rho} = 0.25$, assuming failure governed by classical Euler buckling results in an overestimation of the critical load by 17% for the present study. In literature (Gibson and Ashby,

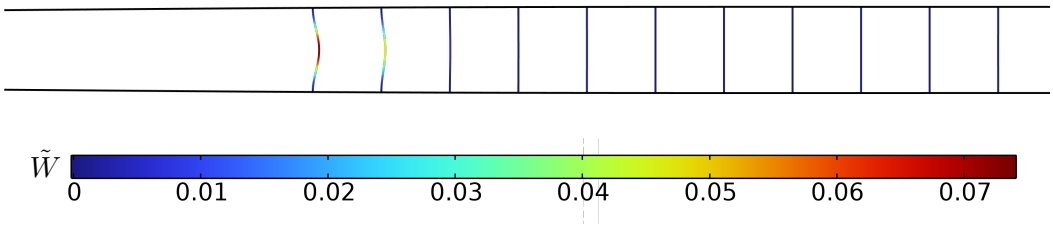


Figure 6.9.: Interface buckling for $\tilde{\rho} = 0.06$ at the critical loading just before damage is introduced to the interface. The large pillar deformations result in a softening of the interface.

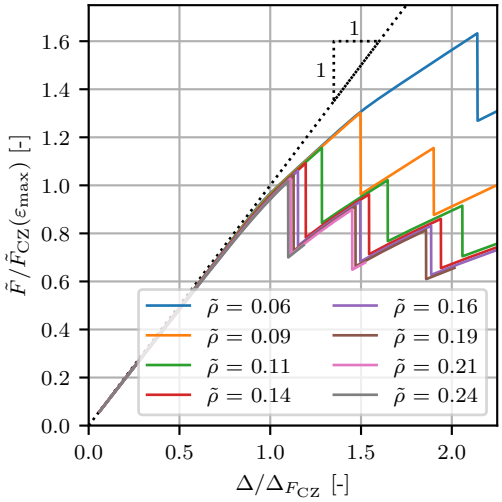


Figure 6.10.: Normalized load-deflection relation from the analytical reference model. For comparison of the models, the results are plotted with respect to the analytical critical loading $\tilde{F}_{\mathrm{CZ}}(\varepsilon_{\max})$ and the corresponding critical deflection $\Delta_{F_{CZ}} = 2h_{\mathrm{i}}\tilde{w}(\tilde{x} = -\tilde{a},\ \tilde{F} = \tilde{F}_{\mathrm{CZ}}(\varepsilon_{\max}))$.

1997; Shenhav and Sherman, 2019; Shaikeea et al., 2022; Athanasiadis et al., 2021) of architected materials, the classical Euler buckling load is often used for the assumption of the critical failure load in compression. However, the presented results show that neglecting the rotation imperfection from the surrounding structures can lead to a significant overestimation of the load-bearing capacity for high values of $\tilde{\rho}$. In contrast, for low values of $\tilde{\rho}$ the numerical reference model shows that large deflections are introduced, softening the interface material. Simplifying the damage initiation by considering the Euler buckling load should be done with care, even for initially perfect structures.

In the present study, bending stresses are found to be most relevant for interfaces with high relative density. This observation contrasts with the findings of de Waal et al. (2025b), who reported that bending stresses dominate the mechanical response at low relative densities. The differing trends can be explained by the boundary conditions imposed at the interface between the lattice and the surrounding structure. In the work of de Waal et al. (2025b), the lattice elements were connected to the interface boundary through connections that allowed for free rotation. Under such conditions, the increase in the bending stiffness limits the lattice bending deformations and reduces the associated bending stresses. Consequently, bending effects were more pronounced at lower relative densities, where the lattice elements remained more compliant. In contrast, the present analysis assumes rigid connections between the lattice and the adherends at the interface boundary, suppressing rotational freedom. As the structural responses are only limitedly influenced by the bending stiffness of the interface lattices (see Section 4.3.2), the contribution of bending stresses becomes increasingly more relevant at higher relative densities as the lattice thickness increases.

### 6.3.3. Geometrical imperfection

Introducing a positive geometric imperfection to the pillar interface increases the total imperfection, moving the failure criterion of the compression zone toward the tension failure criterion ($\varepsilon_{\max} \geq \varepsilon_{\text{ten}}$). Since this failure condition is already fulfilled, when assuming an initial perfect structure (see Section 6.3.2), only this failure criterion is considered in this section. Based on the discussion in Section 6.3.1, the critical force is evaluated in both $\tilde{X} = 0$ and $\tilde{X} = 1/2$. The results are depicted in Figure 6.11. As shown, the normalized critical force is found at the center of the pillar ($\tilde{X} = 1/2$). Figure 6.12 compares the load-bearing capacity with and without geometrical imperfections to that of an initial perfect structure. The geometrical imperfection results in a clear reduction of the load-bearing capacity of up to 11% and 21% for geometrical imperfections of 0.03 and 0.06, respectively. Compared to the Euler buckling case, it appears that geometrical imperfection significantly reduces the load-bearing capacity at all relative densities, whereas rotational imperfection only becomes important at higher relative densities for the present setup.

In the present analysis, the buckling behavior is examined for a simple pillar interface where the individual lattices of the interface are connected by the adherends. In more complex topologies, such as the triangular material, the connections between the lattice elements lead to both tensile and compressive stress states for the lattices in the same area, e.g., the tensile zone (see Section 4.3.1). Wang et al. (2025) demonstrated through compact tension tests of triangular mechanical metamaterials that the fracture toughness can be enhanced through buckling deformations of the compression-loaded lattice members, thereby expanding the process zone. They improved the fracture toughness further by differentiating the lattice thickness of the tensile and compression-loaded elements. An

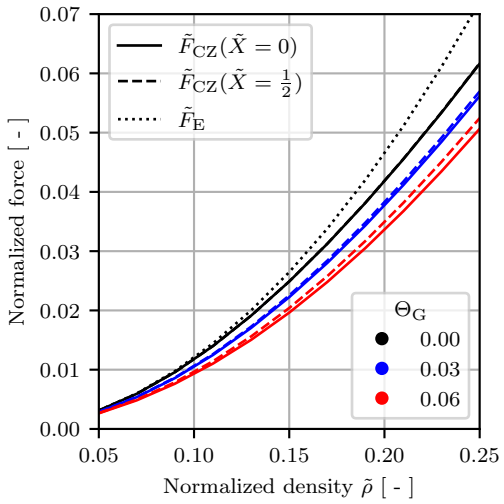


Figure 6.11.: Critical force for varying geometrical imperfections.

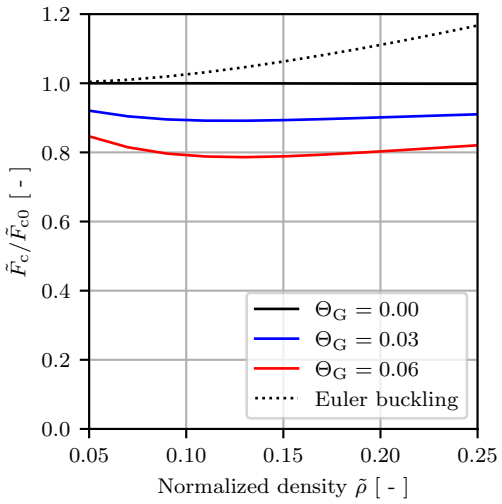


Figure 6.12.: Load ratio with respect to the initial perfect structure.

alternative approach to force such buckling deformation is the introduction of geometric imperfections in the lattice members prone to buckling. This strategy may enable buckling deformations to occur at higher relative densities, providing an additional design parameter for tailoring the failure behavior of mechanical metamaterials and architected interfaces.

## 6.4. Conclusion

In this chapter, the buckling behavior of stretching-dominated architected interfaces was investigated with a focus on imperfections induced by the rotation of the adherend boundaries as identified in Chapter 4. An analytical framework was developed that incorporates the concept of rotation imperfections introduced in Chapter 5, together with geometric imperfections. The inclusion of imperfections expands the failure analysis of compression-loaded lattice elements, requiring up to four distinct evaluation points to determine the critical load. For initially perfect structures, the analysis reduces to two evaluation points, while classical Euler buckling, which neglects all imperfections, requires only a single evaluation. The influence of rotation imperfections is most pronounced at high relative densities, where bending stresses become more significant due to the increased lattice thickness. Geometric imperfections lead to a reduction in the load-bearing capacity across all investigated configurations. At low relative densities, a softening behavior of the interface is observed in the numerical reference model, which is not captured by the present analytical formulation.

# 7. Conclusion and outlook

The present work aimed to improve material selection for mechanical engineering design. In the context of material failure, the material selection process was enhanced through the development of a more accurate filtering method for brittle materials. In addition, the damage behavior of the promising material class of mechanical metamaterials was investigated under confined conditions. By advancing both the understanding of material failure and the methods used to navigate the wide range of available materials, this work contributes to better material choices for engineering design.

A physically justified filtering method for brittle materials for the screening phase of the material selection process was presented in Chapter 3. Based on the principles of linear elastic fracture mechanics, the ratio of fracture toughness to strength was identified as an appropriate brittleness indicator, with the corresponding filter limit determined by the maximum admissible defect size. The proposed filtering method was evaluated through a failure analysis of 31 materials spanning a broad range of material classes. The materials were clearly separated into two groups according to their dominant failure mode: strength-controlled failure and fracture-controlled failure, corresponding to ductile and brittle behavior, respectively. Compared to a simple fracture toughness attribute limit, the proposed brittleness filter provides a more accurate classification of failure modes and, consequently, a more reliable identification of brittle materials. This outcome aligns with the primary objective of the material selection screening process, retaining all material candidates that satisfy the imposed design constraints while excluding materials that are unsuitable for the intended application. By enabling the inclusion of a broader spectrum of material classes in the subsequent ranking stage, the proposed method avoids the unjustified exclusion of non-metallic materials, as it happens, using the fracture toughness-based limits. The findings support replacing the conventional fracture toughness attribute limit with the fracture toughness-to-strength ratio as a more precise and physically motivated brittleness filter that can be evaluated directly from material properties in the early stage of the design process.

To analyze damage processes in confined mechanical metamaterials, a numerical framework was developed, as presented in Chapter 4. An architected interface in a double cantilever beam configuration was investigated to evaluate the damage process within the lattice interface. For the individual lattice elements, both the material strength and fracture toughness of the base material were incorporated into the damage model. Consistent with the proposed brittleness filter, the fracture toughness-to-strength ratio was identified as a

key parameter for distinguishing between brittle and ductile failure modes of tensile-loaded lattice elements. The transition between these failure regimes is governed by the lattice length. For long lattice elements, damage is dominated by material strength, leading to rapid fracture. As the lattice length decreases, the damage process becomes more gradual, resulting in an increasingly ductile response. The adherends confining the interface material transfer small rotations to the lattice boundaries, which induce bending stresses in the otherwise stretching-dominated lattice elements. The global structural response remains governed by axial deformation, such that variations in bending stiffness while maintaining constant axial stiffness lead to only minor changes in overall compliance. In contrast, an increase in rotational stiffness amplifies bending stresses within the lattice elements, thereby reducing the load-bearing capacity of the interface.

The boundary rotations transmitted to the interface from the adherends break the initially perfect geometry of the lattice, transforming the buckling of compressed lattice elements into a deformation problem. In Chapter 5, the concept of rotation imperfections for buckling analysis was introduced, and an analytical framework was developed to study the buckling behavior of confined lattice structures subjected to either static or kinematic boundary rotation imperfections. A case study of simple lattice structures highlighted the critical role of rotation imperfections. For rigidly connected lattice elements, the load-bearing capacity was reduced by 22% compared to structures assembled by connections allowing for free rotations. This reduction is notable when compared to classical Euler buckling predictions, where rigid connections increase the critical load by a factor of four relative to pinned conditions. To investigate the influence of imperfections in architected interfaces under compressive loading, both rotation and geometric imperfections were incorporated into an analytical framework for evaluation of the damage initiation in confined pillar interfaces (see Chapter 6). For compression-loaded lattice elements, two critical evaluation positions along the lattice length were identified: one at the lattice midspan and one at the boundary. Due to symmetry, only one of the boundaries needs to be considered. At each evaluation position, failure may be initiated by either the maximum or minimum strain across the cross-section, resulting in four potential failure points there need to be evaluated. In contrast, for initially perfect lattice structures, the analysis reduces to two evaluation points located at the lattice midspan cross-section. When all imperfections are neglected, as in classical Euler buckling theory, only a single evaluation is required to predict damage initiation. For initially perfect structures, the only imperfections present in the interface arise from boundary rotations transferred from the adherends. The influence of rotation imperfections is most pronounced at high relative densities, where bending stresses become significant, while geometric imperfections affect the load-bearing capacity across the entire range of relative densities. At low relative densities, numerical reference simulations reveal that buckling induces a softening response of the interface, a behavior that is not captured by the proposed analytical framework.

This work provides deeper insight into the damage mechanisms of confined mechanical metamaterials. While intrinsic material properties offer a general description of the

mechanical response and failure of solid materials, the introduction of a topology that defines the mechanical metamaterials fundamentally alters the material behavior and associated damage processes. For lattice interfaces, the failure onset in either the tension or compression zone is determined by the relative density of the lattice interface. For lattice elements subjected to local tensile loading, the damage response is controlled by the lattice length. Longer lattice elements tend to fail in a brittle manner, whereas shorter elements show an increasingly ductile response. However, as reported by Fulco et al. (2022), increasing the interface height corresponding to an increased lattice length in pillar-based interfaces can also enlarge the plastic zone associated with fracture, thereby promoting a more ductile failure behavior of the interface. In addition, toughening mechanisms in the form of bridging-like structures were identified, contributing to an enhanced resistance against damage progression. Whereas in compression, failure is introduced by the buckling response, where low relative densities can result in a softening of the interface materials, thereby extending the process zone for a more ductile failure response. Overall, the results presented here extend the current understanding of damage in confined metamaterials while highlighting the inherent complexity of their analysis. Topology, relative density, imperfections, global geometry, boundary conditions, loading configuration, and the material properties of the base material all interact to govern the damage process. At the same time, this broad design space provides substantial flexibility for tailoring the mechanical performance of architected interfaces.

The results are validated by agreement between the numerical and the analytical work. However, the validation is limited by the lack of experimental work. Experimental studies on the damage of confined metamaterials are also limited in the literature. There is, therefore, for further work a definite need for experimental research on confined metamaterials.

The findings are limited to the assumption of elastic-brittle materials. For the brittleness filter of the material selection screening process, this assumption seems valid, as the filter is meant to serve in the area of brittle materials under the assumption of small material defects. The filtering method does not serve as a replacement for a full fracture analysis. For the study of confined mechanical metamaterials, the assumptions of elastic-brittle materials limit the proposed models to a limited range of base materials. A natural progression of this work is to expand the material damage model for the numerical analysis to include plasticity of the materials.

The buckling analysis, including rotational imperfections, is limited to the shape of a half sinus wave. For more complex interface geometries, an assumption of equal rotation of the interface boundary breaks down. Further research is required to expand the method for more complex imperfection shapes. Additionally, the Winkler foundation assumes a linear elastic response of the interface, which was shown to be an invalid assumption for low relative densities of the interface material, where large deflection due to buckling of multiple lattices leads to a softening of the interface.

Further research could explore the size effect of the lattice structures. Both in the form of the Weibull statistical size effect and from the fields of finite fracture mechanics related to the crack initiation of the lattice due to bending. For comparison of confined mechanical metamaterials to other conventional interface materials, it is advantageous to evaluate the fracture toughness of the lattice interface materials and introduce R-curves for structures where bridging effects are present. A reasonable approach to tackle this could be to adopt already well-established methods, such as the compact tension test or the double cantilever beam test, evaluating the fracture toughness at the interface boundary. Extensive studies are required due to the large variety of design possibilities. Additionally, detailed studies and methods for the evaluation of material properties inside the interface are needed, considering the porous structure of the lattice interfaces.

# Bibliography

V. Adam, B. Bergfeld, P. Weißgraeber, A. van Herwijnen, and P. L. Rosendahl. Fracture toughness of mixed-mode anticracks in highly porous materials. *Nature Communications*, 15(1):7379, 2024. doi: 10.1038/s41467-024-51491-7.

M. Aliha, A. Bahmani, and S. Akhondi. Determination of mode III fracture toughness for different materials using a new designed test configuration. *Materials & Design*, 86: 863–871, 2015. doi: 10.1016/j.matdes.2015.08.033.

M. S. Anderson. Buckling of periodic lattice structures. *AIAA Journal*, 19(6):782–788, 1981. doi: 10.2514/3.51003.

T. L. Anderson. *Fracture Mechanics*. CRC Press, 2017. ISBN 9781315370293. doi: 10.1201/9781315370293.

M. F. Ashby. Materials selection in conceptual design. *Materials Science and Technology*, 5(6):517–525, 1989. doi: 10.1179/mst.1989.5.6.517.

M. F. Ashby. *Materials Selection in Mechanical Design*. Butterworth-Heinemann, 5th. edition edition, 2016. ISBN 9780081005996.

A. E. Athanasiadis, M. K. Budzik, D. Fernando, and M. A. Dias. On micropolar elastic foundations. *European Journal of Mechanics - A/Solids*, 105:105277, 2024. doi: 10.1016/j.euromechsol.2024.105277.

A. E. F. Athanasiadis, M. A. Dias, and M. K. Budzik. Can confined mechanical metamaterials replace adhesives? *Extreme Mechanics Letters*, 48:101411, 2021. doi: 10.1016/j.eml.2021.101411.

A. E. F. Athanasiadis, O. Duncan, M. K. Budzik, and M. A. Dias. Toughness of confined auxetic foams. *Advanced Engineering Materials*, 27(17), 2025. doi: 10.1002/adem.202500626.

Z. P. Bažant and L. Cedolin. *Stability of Structures*. WORLD SCIENTIFIC, 2010. ISBN 978-981-4317-02-3. doi: 10.1142/7828.

B. Bender and K. Gericke. *Pahl/Beitz Konstruktionslehre*. Springer Berlin Heidelberg, Berlin, Heidelberg, 2021. ISBN 978-3-662-57302-0. doi: 10.1007/978-3-662-57303-7.

J. B. Berger, H. N. G. Wadley, and R. M. McMeeking. Mechanical metamaterials at the theoretical limit of isotropic elastic stiffness. *Nature*, 543(7646):533–537, 2017. doi: 10.1038/nature21075.

R. Bermejo and R. Danzer. Mechanical characterization of ceramics. In V. K. Sarin, D. Mari, L. Llanes, and C. E. Nebel, editors, *Comprehensive hard materials / editor-in-chief, Vinod K. Sarin*, pages 285–298. Elsevier, Amsterdam, 2014. ISBN 978-0-08-096528-4. doi: 10.1016/B978-0-08-096527-7.00028-3.

E. T. Bird, A. E. Bowden, M. K. Seeley, and D. T. Fullwood. Materials selection of flexible open-cell foams in energy absorption applications. *Materials & Design*, 137: 414–421, 2018. doi: 10.1016/j.matdes.2017.10.054.

R. R. Boyer, J. D. Cotton, M. Mohaghegh, and R. E. Schafrik. Materials considerations for aerospace applications. *MRS Bulletin*, 40(12):1055–1066, 2015. doi: 10.1557/mrs.2015.278.

W. Brostow, H. E. Hagg Lobland, and M. Narkis. Sliding wear, viscoelasticity, and brittleness of polymers. *Journal of Materials Research*, 21(09):2422–2428, 2006. doi: 10.1557/jmr.2006.0300.

B. Budiansky. Theory of buckling and post-buckling behavior of elastic structures. *Advances in Applied Mechanics*, 14:1–65, 1974. doi: 10.1016/S0065-2156(08)70030-9.

M. K. Budzik, J. Jumel, and M. E. R. Shanahan. Impact of interface heterogeneity on joint fracture. *The Journal of Adhesion*, 88(11-12):885–902, 2012. doi: 10.1080/00218464.2012.725604.

J. Cai, R. Yang, X. Wang, and J. Feng. Effect of initial imperfections of struts on the mechanical behavior of tensegrity structures. *Composite Structures*, 207:871–876, 2019. doi: 10.1016/j.compstruct.2018.09.018.

C. Calladine. Buckminster fuller's "tensegrity" structures and clerk maxwell's rules for the construction of stiff frames. *International Journal of Solids and Structures*, 14(2): 161–172, 1978. doi: 10.1016/0020-7683(78)90052-5.

J. J. Carruthers, M. Calomfirescu, P. Ghys, and J. Prockat. The application of a systematic approach to material selection for the lightweighting of metro vehicles. *Proceedings of the Institution of Mechanical Engineers, Part F: Journal of Rail and Rapid Transit*, 223 (5):427–437, 2009. doi: 10.1243/09544097JRRT279.

K. S. Chan. Fracture and toughening mechanisms in an $\alpha$ 2 titanium aluminide alloy. *Metallurgical Transactions A*, 21(10):2687–2699, 1990. doi: 10.1007/BF02646064.

S.-L. Chan and J.-X. Gu. Exact tangent stiffness for imperfect beam-column members. *Journal of Structural Engineering*, 126(9):1094–1102, 2000. doi: 10.1061/(ASCE) 0733-9445(2000)126:9(1094).

S.-L. Chan, G. ping Shu, and Z. tao Lü. Stability analysis and parametric study of pre-stressed stayed columns. *Engineering Structures*, 24(1):115–124, 2002. doi: 10.1016/ S0141-0296(01)00026-8.

E. Chen, S. Luan, and S. Gaitanaros. On the compressive strength of brittle lattice metamaterials. *International Journal of Solids and Structures*, 257:111871, 2022. doi: 10.1016/j.ijsolstr.2022.111871.

T. Chen, C. M. Harvey, S. Wang, and V. V. Silberschmidt. Analytical corrections for double-cantilever beam tests. *International Journal of Fracture*, 229(2):269–276, 2021. doi: 10.1007/s10704-021-00556-5.

J. Choi. Material selection method using tangible and intangible material properties: A case study of travel luggage. *Metals and Materials International*, 29(7):1961–1967, 2023. doi: 10.1007/s12540-022-01358-7.

P. da Silva, R. Campilho, A. Vieira, A. Faria, K. Madani, A. Houari, and M. Bellali. Characterization of the mechanical properties and fracture toughness of sheet molding compound. *Procedia Structural Integrity*, 72:69–76, 2025. doi: 10.1016/j.prostr.2025.08. 075.

R. Danzer, P. Supancic, J. Pascual, and T. Lube. Fracture statistics of ceramics – weibull statistics and deviations from weibull statistics. *Engineering Fracture Mechanics*, 74 (18):2919–2932, 2007. doi: 10.1016/j.engfracmech.2006.05.028.

R. Danzer, T. Lube, P. Supancic, and R. Damani. Fracture of ceramics. *Advanced Engineering Materials*, 10(4):275–298, 2008. doi: 10.1002/adem.200700347.

D. Davidson, K. Chan, R. McClung, and S. Hudak. Small fatigue cracks. In I. Milne, R. O. Ritchie, and B. L. Karihaloo, editors, *Comprehensive structural integrity*, pages 129–164. Elsevier/Pergamon, Amsterdam and Boston, 2003. ISBN 978-0-08-043749-1. doi: 10.1016/B0-08-043749-4/04073-8.

A. de Morais, M. de Moura, A. Marques, and P. de Castro. Mode-I interlaminar fracture of carbon/epoxy cross-ply composites. *Composites Science and Technology*, 62(5):679–686, 2002. doi: 10.1016/S0266-3538(01)00223-8.

L. de Waal, M. Chouzouris, and M. A. Dias. Cracking down on fracture to functionalize damage. *Physical Review Letters*, 135(14):148202, 2025a. doi: 10.1103/s28l-zbpz.

L. de Waal, M. Chouzouris, and M. A. Dias. Architecting mechanisms of damage in topological metamaterials. *Physical Review Research*, 7(3), 2025b. doi: 10.1103/ckmq-tf86.

M. Derriso, C. McCurry, and C. Schubert Kabban. A novel approach for implementing structural health monitoring systems for erospace structures. In F.-G. Yuan, editor, *Structural Health Monitoring (SHM) in Aerospace Structures*, pages 33–56. Woodhead Publishing, 2016. ISBN 978-0-08-100148-6. doi: 10.1016/B978-0-08-100148-6.00002-0.

V. Deshpande, M. Ashby, and N. Fleck. Foam topology: bending versus stretching dominated architectures. *Acta Materialia*, 49(6):1035–1040, 2001. doi: 10.1016/S1359-6454(00)00379-7.

G. Domokos, P. Holmes, and B. Royce. Constrained euler buckling. *Journal of Nonlinear Science*, 7(3):281–314, 1997. doi: 10.1007/BF02678090.

A. V. Eremin, M. V. Burkov, A. A. Bogdanov, A. A. Kononova, and P. S. Lyubutin. Impact behavior and residual strength of peek/cf-laminated composites with various stacking sequences. *Polymers*, 16(5), 2024. doi: 10.3390/polym16050717.

H. Fan, F. Jin, and D. Fang. Uniaxial local buckling strength of periodic lattice composites. *Materials & Design*, 30(10):4136–4145, 2009. doi: 10.1016/j.matdes.2009.04.034.

J. Fan, L. Zhang, S. Wei, Z. Zhang, S.-K. Choi, B. Song, and Y. Shi. A review of additive manufacturing of metamaterials and developing trends. *Materials Today*, 50:303–328, 2021. doi: 10.1016/j.mattod.2021.04.019.

P. Ferro and F. Bonollo. Materials selection in a critical raw materials perspective. *Materials & Design*, 177:107848, 2019. doi: 10.1016/j.matdes.2019.107848.

R. C. Fletcher and D. D. Pollard. Anticrack model for pressure solution surfaces. *Geology*, 9(9):419–424, 09 1981. doi: 10.1130/0091-7613(1981)9<419:AMFPSS>2.0.CO;2.

Forest Products Laboratory. *Wood handbook: wood as an engineering material*. U.S. Department of Agriculture, Forest Service, Forest Products Laboratory, Madison, WI, 1999. doi: 10.2737/FPL-GTR-113.

S. Fulco, M. K. Budzik, E. D. Bain, and K. T. Turner. Decoupling toughness and strength through architected plasticity. *Extreme Mechanics Letters*, 57:101912, 2022. doi: 10.1016/j.eml.2022.101912.

S. Fulco, M. K. Budzik, H. Xiao, D. J. Durian, and K. T. Turner. Disorder enhances the fracture toughness of 2d mechanical metamaterials. *PNAS Nexus*, 4(2):pgaf023, 2025. doi: 10.1093/pnasnexus/pgaf023.

J. M. Gere and B. J. Goodno. *Mechanics of materials*. Cengage Learning, Stamford, Conn., 8th ed., si edition, 2013. ISBN 1-111-57774-9.

L. J. Gibson and M. F. Ashby. *Cellular solids : structure and properties*. Cambridge solid state science series. Cambridge University Press, Cambridge, second edition edition, 1997. ISBN 9781139878326. doi: 10.1017/CBO9781139878326.

A. M. Girão Coelho, P. D. Simão, and M. A. Wadee. Imperfection sensitivity of column instability revisited. *Journal of Constructional Steel Research*, 90:265–282, 2013. doi: 10.1016/j.jcsr.2013.08.006.

M. Gomez, D. E. Moulton, and D. Vella. Critical slowing down in purely elastic 'snap-through' instabilities. *Nature Physics*, 13(2):142–145, 2017. doi: 10.1038/nphys3915.

H. Gu, M. Pavier, and A. Shterenlikht. Experimental study of modulus, strength and toughness of 2d triangular lattices. *International Journal of Solids and Structures*, 152-153:207–216, 2018. doi: 10.1016/j.ijsolstr.2018.06.028.

B. Guo, X. Zheng, M. Gerini-Romagnoli, and L. Yang. Digital shearography for ndt: Determination and demonstration of the size and the depth of the smallest detectable defect. *NDT & E International*, 139:102927, 2023. doi: 10.1016/j.ndteint.2023.102927.

B. Haghpanah, J. Papadopoulos, D. Mousanezhad, H. Nayeb-Hashemi, and A. Vaziri. Buckling of regular, chiral and hierarchical honeycombs under a general macroscopic stress state. *Proceedings. Mathematical, physical, and engineering sciences*, 470(2167): 20130856, 2014. doi: 10.1098/rspa.2013.0856.

R. D. Hale, D. K. Hsu, and D. O. Adams. Ultrasonic nde techniques and the effects of flaws on mechanical performance in multi-directionally reinforced textile composites. In D. O. Thompson and D. E. Chimenti, editors, *Review of Progress in Quantitative Nondestructive Evaluation: Volume 15A*, pages 1247–1254. Springer US, Boston, MA, 1996. ISBN 978-1-4613-8027-6. doi: 10.1007/978-1-4613-0383-1_162.

B. Hanks, J. Berthel, M. Frecker, and T. W. Simpson. Mechanical properties of additively manufactured metal lattice structures: Data review and design interface. *Additive Manufacturing*, 35:101301, 2020. doi: 10.1016/j.addma.2020.101301.

N. A. Harder. Dimensional analysis for concrete in fracture. *Materials and Structures*, 24 (3):202–209, 1991. doi: 10.1007/BF02472986.

P. S. Harvey and T. Cain. Buckling of elastic columns with initial imperfections and load eccentricity. *Structures*, 23:660–664, 2020. doi: 10.1016/j.istruc.2019.09.021.

P. S. Harvey, L. N. Virgin, and M. H. Tehrani. Buckling of elastic columns with second-mode imperfections. *Meccanica*, 54(8):1245–1255, 2019. doi: 10.1007/s11012-019-01025-z.

Z. Hashin. Finite thermoelastic fracture criterion with application to laminate cracking analysis. *Journal of the Mechanics and Physics of Solids*, 44(7):1129–1145, 1996.

M. Hedvard and P. Weißgraeber. Numerical method for fracture modelling of lattice interface materials in composite structures. In C. Binetruy and F. Jacquemin, editors, *Proceedings of the 21st European Conference on Composite Materials: Nantes Université*, volume Vol. 3, pages 226–231, 2024.

M. Hedvard and P. Weißgraeber. Buckling of fully-connected lattices with load-induced boundary rotation imperfections. *International Journal of Solids and Structures*, 334: 113961, 2026. ISSN 0020-7683. doi: 10.1016/j.ijsolstr.2026.113961. URL https://www.sciencedirect.com/science/article/pii/S0020768326001332.

M. Hedvard, M. Eichler, and P. Weißgraeber. Reevaluating brittleness in material selection: Why fracture toughness alone is insufficient. *Materials & Design*, 254:114109, 2025a. doi: 10.1016/j.matdes.2025.114109.

M. Hedvard, I. Jonuschies, M. Eichler, and P. Weißgraeber. Material selection methods: brittleness filter are often too strict. *Proceedings of the Design Society*, 5:2373–2380, 2025b. doi: 10.1017/pds.2025.10251.

M. L. Hedvard, M. A. Dias, and M. K. Budzik. Toughening mechanisms and damage propagation in architected-interfaces. *International Journal of Solids and Structures*, 288:112600, 2024. doi: 10.1016/j.ijsolstr.2023.112600.

S. Heide-Jørgensen, M. K. Budzik, and K. T. Turner. Mechanics and fracture of structured pillar interfaces. *Journal of the Mechanics and Physics of Solids*, 137:103825, 2020. doi: 10.1016/j.jmps.2019.103825.

K. D. Hjelmstad. *Fundamentals of Structural Mechanics*. Springer US, Boston, MA, second edition edition, 2005. ISBN 978-0-387-23330-7. doi: 10.1007/b101129.

M.-T. Hsieh, C. S. Ha, Z. Xu, S. Kim, H. F. Wu, V. Kunc, and X. Zheng. Stiff and strong, lightweight bi-material sandwich plate-lattices with enhanced energy absorption. *Journal of Materials Research*, 36(18):3628–3641, 2021. doi: 10.1557/s43578-021-00322-2.

W. Hua, J. Li, Z. Zhu, A. Li, J. Huang, Z. Gan, and S. Dong. A review of mixed mode I-II fracture criteria and their applications in brittle or quasi-brittle fracture analysis. *Theoretical and Applied Fracture Mechanics*, 124:103741, 2023. doi: 10.1016/j.tafmec.2022.103741.

Husaini, N. Ali, R. Riantoni, T. E. Putra, and H. Husin. Study of leaf spring fracture behavior used in the suspension systems in the diesel truck vehicles. *IOP Conference Series: Materials Science and Engineering*, 541(1):012046, 2019. doi: 10.1088/1757-899X/541/1/012046.

A. Jahan, M. Y. Ismail, S. M. Sapuan, and F. Mustapha. Material screening and choosing methods – a review. *Materials & Design*, 31(2):696–705, 2010. doi: 10.1016/j.matdes.2009.08.013.

J. B. Jamieson and J. Schweizer. Texture and strength changes of buried surface-hoar layers with implications for dry snow-slab avalanche release. *Journal of Glaciology*, 46 (152):151–160, 2000. doi: 10.3189/172756500781833278.

M. Jamshidian, N. Boddeti, D. W. Rosen, and O. Weeger. Multiscale modelling of soft lattice metamaterials: Micromechanical nonlinear buckling analysis, experimental verification, and macroscale constitutive behaviour. *International Journal of Mechanical Sciences*, 188:105956, 2020. doi: 10.1016/j.ijmecsci.2020.105956.

S. Janbaz, F. S. L. Bobbert, M. J. Mirzaali, and A. A. Zadpoor. Ultra-programmable buckling-driven soft cellular mechanisms. *Materials Horizons*, 6(6):1138–1147, 2019. doi: 10.1039/c9mh00125e.

H.-M. Ji, X.-N. Liu, and X.-W. Li. Study on the fracture toughness of softwood and hardwood estimated by boundary effect model. *Materials (Basel)*, 15(11), 2022. doi: 10.3390/ma15114039.

T. Kanahama and M. Sato. Self-buckling with initial imperfections: Application to trees. *International Journal of Engineering Science*, 194:103972, 2024. doi: 10.1016/j.ijengsci.2023.103972.

M. F. Kanninen. An augmented double cantilever beam model for studying crack propagation and arrest. *International Journal of Fracture*, 9:83–92, 1973. doi: 10.1007/BF00035958.

A. Klasson, R. Crocetti, and E. F. Hansson. Slender steel columns: How they are affected by imperfections and bracing stiffness. *Structures*, 8:35–43, 2016. doi: 10.1016/j.istruc.2016.08.004.

H. M. A. Kolken, S. Janbaz, S. M. A. Leeflang, K. Lietaert, H. H. Weinans, and A. A. Zadpoor. Rationally designed meta-implants: a combination of auxetic and conventional meta-biomaterials. *Materials Horizons*, 5:28–35, 2018. doi: 10.1039/C7MH00699C.

E. Konofalska, P. Kozakiewicz, W. Buraczyk, H. Szeligowski, and H. Lachowicz. The technical quality of the wood of scots pine (pinus sylvestris l.) of diverse genetic origin. *Forests*, 12(5):619, 2021. doi: 10.3390/f12050619.

E. Kreyszig, H. Kreyszig, and E. J. Norminton. *Advanced engineering mathematics / Erwin Kreyszig ; in collaboration with Herbert Kreyszig, Edward J. Norminton.* John Wiley & Sons, Inc, Hoboken, N.J., 10th edition edition, 2011. ISBN 978-0-470-64613-7.

N. Kristanič and J. Korelc. Optimization method for the determination of the most unfavorable imperfection of structures. *Computational Mechanics*, 42(6):859–872, 2008. doi: 10.1007/s00466-008-0288-9.

B. R. Lawn and D. B. Marshall. Hardness, toughness, and brittleness: An indentation analysis. *Journal of the American Ceramic Society*, 62(7-8):347–350, 1979. doi: 10.1111/j.1151-2916.1979.tb19075.x.

S. Lee, J. Kwon, H. Kim, R. O. Ritchie, and G. X. Gu. Advancing programmable metamaterials through machine learning-driven buckling strength optimization. *Current Opinion in Solid State and Materials Science*, 31:101161, 2024. doi: 10.1016/j.cossms.2024.101161.

D. Leguillon. Strength or toughness? a criterion for crack onset at a notch. *European Journal of Mechanics - A/Solids*, 21(1):61–72, 2002. doi: 10.1016/S0997-7538(01)01184-6.

P. Li, Y. E. Ma, W. Sun, X. Qian, W. Zhang, and Z. Wang. Mechanical behaviors and failure modes of additive manufactured ti6al4v lattice structures under compressive load. *Thin-Walled Structures*, 180:109778, 2022. doi: 10.1016/j.tws.2022.109778.

G. Lin, J. Li, P. Chen, W. Sun, S. A. Chizhik, A. A. Makhaniok, G. B. Melnikova, and T. A. Kuznetsova. Buckling of lattice columns made from three-dimensional chiral mechanical metamaterials. *International Journal of Mechanical Sciences*, 194:106208, 2021. doi: 10.1016/j.ijmecsci.2020.106208.

Q. Lin, S. Wang, P.-Z. Pan, W.-W. Ji, and Y. Lu. Fracture initiation under pure shear revisited: Remarks on the mode II fracture in quasi-brittle materials. *Theoretical and Applied Fracture Mechanics*, 109:102700, 2020. doi: 10.1016/j.tafmec.2020.102700.

E. Lindgaard, E. Lund, and K. Rasmussen. Nonlinear buckling optimization of composite

structures considering "worst" shape imperfections. *International Journal of Solids and Structures*, 47(22-23):3186–3202, 2010. doi: 10.1016/j.ijsolstr.2010.07.020.

C. Liu, Z. Gao, J. Chang, J. Zhao, S. Qiu, P. Yu, and X. Zhang. A lattice-mechanical metamaterial with tunable two-step deformation, tunable stiffness, tunable energy absorption and programmable properties. *Materials Research Express*, 11(12):125801, 2024. doi: 10.1088/2053-1591/ad9b72.

C. Lu, M. Hsieh, Z. Huang, C. Zhang, Y. Lin, Q. Shen, F. Chen, and L. Zhang. Architectural design and additive manufacturing of mechanical metamaterials: A review. *Engineering*, 17:44–63, 2022. doi: 10.1016/j.eng.2021.12.023.

K. Mangipudi and P. Onck. Multiscale modelling of damage and failure in two-dimensional metallic foams. *Journal of the Mechanics and Physics of Solids*, 59(7):1437–1461, 2011. doi: 10.1016/j.jmps.2011.02.008.

I. Maskery, L. Sturm, A. O. Aremu, A. Panesar, C. B. Williams, C. J. Tuck, R. D. Wildman, I. A. Ashcroft, and R. Hague. Insights into the mechanical properties of several triply periodic minimal surface lattice structures made by polymer additive manufacturing. *Polymer*, 152:62–71, 2018. doi: 10.1016/j.polymer.2017.11.049.

M. Maurizi, C. Gao, and F. Berto. Inverse design of truss lattice materials with superior buckling resistance. *npj Computational Materials*, 8, 2022. doi: 10.1038/s41524-022-00938-w.

J. C. Maxwell. L. On the calculation of the equilibrium and stiffness of frames. *The London, Edinburgh, and Dublin Philosophical Magazine and Journal of Science*, 27 (182):294–299, 1864. doi: 10.1080/14786446408643668.

C. E. Mazzilli. Buckling and post-buckling of extensible rods revisited: A multiple-scale solution. *International Journal of Non-Linear Mechanics*, 44(2):200–208, 2009. doi: 10.1016/j.ijnonlinmec.2008.11.005.

Z. Mehmood, I. Haneef, and F. Udrea. Material selection for micro-electro-mechanical-systems (MEMS) using Ashby's approach. *Materials & Design*, 157:412–430, 2018. doi: 10.1016/j.matdes.2018.07.058.

S. Melin. When does a crack grow under mode II conditions? *International Journal of Fracture*, 30(2):103–114, 1986. doi: 10.1007/BF00034020.

G. Molnár, A. Doitrand, R. Estevez, and A. Gravouil. A review of characteristic lengths in the coupled criterion framework and advanced fracture models. *Comptes Rendus. Mécanique*, 353(G1):91–111, 2025. doi: 10.5802/crmeca.280.

S.-D. Nie, S.-B. Kang, L. Shen, and B. Yang. Experimental and numerical study on global buckling of q460gj steel box columns under eccentric compression. *Engineering Structures*, 142:211–222, 2017. doi: 10.1016/j.engstruct.2017.03.064.

W. Nsengiyumva, S. Zhong, J. Lin, Q. Zhang, J. Zhong, and Y. Huang. Advances, limitations and prospects of nondestructive testing and evaluation of thick composites and sandwich structures: A state-of-the-art review. *Composite Structures*, 256:112951, 2021. doi: 10.1016/j.compstruct.2020.112951.

M. Omidi and L. St-Pierre. Fracture toughness of semi-regular lattices. *International Journal of Solids and Structures*, 270:112233, 2023. doi: 10.1016/j.ijsolstr.2023.112233.

F. Papp. Buckling assessment of steel members through overall imperfection method. *Engineering Structures*, 106:124–136, 2016. doi: 10.1016/j.engstruct.2015.10.021.

O. Parate and N. Gupta. Material selection for electrostatic microactuators using Ashby approach. *Materials & Design*, 32(3):1577–1581, 2011. doi: 10.1016/j.matdes.2010.09.012.

L. Parente, D. Addessi, P. Di Re, C. Gatta, and E. Sacco. Micromechanical buckling analysis of soft lattice metamaterials accounting for randomly distributed imperfections. *Mechanics Research Communications*, 148:104450, 2025.

D. Pasini and J. K. Guest. Imperfect architected materials: Mechanics and topology optimization. *MRS Bulletin*, 44(10):766–772, 2019. doi: 10.1557/mrs.2019.231.

R. Peek and N. Triantafyllidis. Worst shapes of imperfections for space trusses with many simultaneously buckling members. *0020-7683*, 29(19):2385–2402, 1992. doi: 10.1016/0020-7683(92)90222-F.

S. C. Quek, A. M. Waas, K. W. Shahwan, and V. Agaram. Failure mechanics of triaxially braided carbon composites under combined bending–compression loading. *Composites Science and Technology*, 66(14):2548–2556, 2006. doi: 10.1016/j.compscitech.2006.01.022.

B. Radisson and E. Kanso. Elastic snap-through instabilities are governed by geometric symmetries. *Physical Review Letters*, 130(23):236102, 2023. doi: 10.1103/physrevlett.130.236102.

M. Radwan and B. Kövesdi. Equivalent geometric imperfection for interaction buckling of welded box-section columns - stochastic analysis. *Journal of Constructional Steel Research*, 213:108374, 2024. doi: 10.1016/j.jcsr.2023.108374.

A. A. Rahim, S. N. Musa, S. Ramesh, and M. K. Lim. A systematic review on material selection methods. *Proceedings of the Institution of Mechanical Engineers, Part L: Journal of Materials: Design and Applications*, 234, 2020. doi: 10.1177/1464420720916765.

C. Ramirez, E. Agaliotis, and V. Pettarin. Fracture toughness and overall characterization of pla based biocomposites with natural fibers: A comparative study. *Polymer*, 307: 127309, 2024. doi: 10.1016/j.polymer.2024.127309.

A. Rashedi, I. Sridhar, and K. Tseng. Multi-objective material selection for wind turbine blade and tower: Ashby's approach. *Materials & Design*, 37:521–532, 2012. doi: 10.1016/j.matdes.2011.12.048.

Y. Ren, R. Huo, and D. Zhou. Buckling and post-buckling analysis of restrained non-uniform columns in fire. *Engineering Structures*, 272:114947, 2022. doi: 10.1016/j.engstruct.2022.114947.

A. Reza Torabi, A. Carpinteri, K. Głowacka, S. Mohammadi, C. Ronchei, D. Scorza, A. Zanichelli, and S. Vantadori. Translaminar fracture toughness characterisation for a glass fibre/polyamide 6 laminated composite by a novel approach based on fictitious material concept. *Composite Structures*, 351:118605, 2025. doi: 10.1016/j.compstruct.2024.118605.

M. I. N. Rosa, K. Karapiperis, K. Radi, E. Pescialli, and D. M. Kochmann. Enhanced deformability through distributed buckling in stiff quasicrystalline architected materials. *Advanced materials (Deerfield Beach, Fla.)*, 37(24):e2505125, 2025. doi: 10.1002/adma.202505125.

P. L. Rosendahl and P. Weißgraeber. Modeling snow slab avalanches caused by weak-layer failure – part 1: Slabs on compliant and collapsible weak layers. *The Cryosphere*, 14 (1):115–130, 2020. doi: 10.5194/tc-14-115-2020.

M. H. Sadd. *Elasticity: Theory, applications, and numerics*. Academic Press, London, fourth edition edition, 2021. ISBN 9780128159880.

A. Salazar, P. M. Frontini, and J. Rodríguez. Determination of fracture toughness of propylene polymers at different operating temperatures. *Engineering Fracture Mechanics*, 126:87–107, 2014. doi: 10.1016/j.engfracmech.2014.04.023.

J. H. Sampaio and J. R. Hundhausen. A mathematical model and analytical solution for buckling of inclined beam-columns. *Applied Mathematical Modelling*, 22(6):405–421, 1998. doi: 10.1016/S0307-904X(98)10014-8.

A. Sanner, L. Michel, A. Lingua, and D. S. Kammer. Less is more: removing a single bond increases the toughness of elastic networks. *International Journal of Fracture*, 249(4), 2025. doi: /10.1007/s10704-025-00891-x.

A. J. D. Shaikeea, H. Cui, M. O'Masta, X. R. Zheng, and V. S. Deshpande. The toughness of mechanical metamaterials. *Nature Materials*, 21(3):297–304, 2022. doi: 10.1038/s41563-021-01182-1.

L. Shenhav and D. Sherman. Fracture of 3d printed brittle open-cell structures under compression. *Materials & Design*, 182:108101, 2019. doi: 10.1016/j.matdes.2019.108101.

S. S. Shukla, K. Murthy, and S. Sajith. Mixed mode (I/III) fracture studies using a new specimen setup. *International Journal of Mechanical Sciences*, 243:108036, 2023. doi: 10.1016/j.ijmecsci.2022.108036.

J. R. Sims. Standards and codes to control hydrogen-induced cracking in pressure vessels and pipes for hydrogen gas storage and transport. In R. P. Gangloff and B. P. Somerday, editors, *Gaseous hydrogen embrittlement of materials in energy technologies*, Woodhead Publishing in materials, pages 177–192. Woodhead Publishing, Cambridge UK and Phildelphia PA, 2012. ISBN 978-1-84569-677-1. doi: 10.1533/9780857093899.1.177.

P. Sirisalee, M. Ashby, G. Parks, and P. John Clarkson. Multi-criteria material selection of monolithic and multi-materials in engineering design. *Advanced Engineering Materials*, 8(1-2):48–56, 2006. doi: 10.1002/adem.200500196.

E. A. Smith. Behavior of columns with pretensioned stays. *Journal of Structural Engineering*, 111(5):961–972, 1985. doi: 10.1061/(ASCE)0733-9445(1985)111:5(961).

J. U. Surjadi, L. Gao, H. Du, X. Li, X. Xiong, N. X. Fang, and Y. Lu. Mechanical metamaterials and their engineering applications. *Advanced Engineering Materials*, 21 (3), 2019. doi: 10.1002/adem.201800864.

H. C. Tankasala and N. A. Fleck. The crack growth resistance of an elastoplastic lattice. *International Journal of Solids and Structures*, 188-189:233–243, 2020. doi: 10.1016/j.ijsolstr.2019.10.007.

H. C. Tankasala, V. S. Deshpande, and N. A. Fleck. 2013 Koiter medal paper: Crack-tip fields and toughness of two-dimensional elastoplastic lattices. *Journal of Applied Mechanics*, 82(9), 2015. doi: 10.1115/1.4030666.

S. Thelandersson and H. J. Larsen. *Timber engineering*. J. Wiley, Chichester, 2003. ISBN 978-0-470-84469-4.

C. R. Thomsen, F. Wang, and O. Sigmund. Buckling strength topology optimization of 2d periodic materials based on linearized bifurcation analysis. *Computer Methods in Applied Mechanics and Engineering*, 339:115–136, 2018. doi: 10.1016/j.cma.2018.04.031.

S. Timoshenko and J. M. Gere. *Theory of elastic stability.* McGraw-Hill, New York, 2nd ed. edition, 1961.

A. Turon, C. G. Dávila, P. P. Camanho, and J. Costa. An engineering solution for mesh size effects in the simulation of delamination using cohesive zone models. *Engineering Fracture Mechanics*, 74(10):1665–1682, 2007. doi: 10.1016/j.engfracmech.2006.08.025.

C. van Innis and T. Pardoen. Thickness-dependent selection of adhesive joints. *The Journal of Adhesion*, 100(12):1155–1208, 2024. doi: 10.1080/00218464.2023.2294131.

Z. Vangelatos, G. X. Gu, and C. P. Grigoropoulos. Architected metamaterials with tailored 3d buckling mechanisms at the microscale. *Extreme Mechanics Letters*, 33: 100580, 2019. doi: 10.1016/j.eml.2019.100580.

A. Viswanath, M. Khalil, F. Al Maskari, W. J. Cantwell, and K. A. Khan. Harnessing buckling response to design lattice structures with improved buckling strength. *Materials & Design*, 232:112113, 2023. doi: 10.1016/j.matdes.2023.112113.

A.-J. Wang and D. L. McDowell. In-plane stiffness and yield strength of periodic metal honeycombs. *Journal of Engineering Materials and Technology*, 126(2):137–156, 2004. doi: 10.1115/1.1646165.

H. Wang, Y. Lyu, S. Bosiakov, H. Zhu, and Y. Ren. A review on the mechanical metamaterials and their applications in the field of biomedical engineering. *Frontiers in Materials*, 10, 2023. doi: 10.3389/fmats.2023.1273961.

W. Wang and J. Xiong. A buckling model of fiber-reinforced composite lattice cylinders with the cutout imperfections. *Engineering Fracture Mechanics*, 325:111343, 2025. doi: 10.1016/j.engfracmech.2025.111343.

W.-J. Wang, W.-M. Zhang, H. Yang, Z.-Y. Li, and L. Ma. Energy absorption characteristics of embedded mechanical metamaterials. *International Journal of Mechanical Sciences*, 309:110998, 2026. doi: 10.1016/j.ijmecsci.2025.110998.

Z. Wang, K. Wu, J. Ding, J. Jin, Y. Zhou, M. Li, Y. Yao, L. He, Z. Song, and Y. Ni. Strut-buckling transformation enabling anomalous density-scaling toughening law in ultralight lattice metamaterials. *Advanced materials (Deerfield Beach, Fla.)*, 37(27): e2419635, 2025. doi: 10.1002/adma.202419635.

P. Weißgraeber and W. Becker. Finite fracture mechanics model for mixed mode fracture in adhesive joints. *International Journal of Solids and Structures*, 50(14):2383–2394, 2013. doi: 10.1016/j.ijsolstr.2013.03.012.

P. Weißgraeber, D. Leguillon, and W. Becker. A review of finite fracture mechanics: crack initiation at singular and non-singular stress raisers. *Archive of Applied Mechanics*, 86: 375–401, 2016. doi: 10.1007/s00419-015-1091-7.

H. M. Westergaard. Bearing pressures and cracks: Bearing pressures through a slightly waved surface or through a nearly flat part of a cylinder, and related problems of cracks. *Journal of Applied Mechanics*, 6(2):A49–A53, 1939. doi: 10.1115/1.4008919.

Wolfram Research. Findroot, 2003. URL https://reference.wolfram.com/language/ref/FindRoot.html. [Accessed: 17-March-2025].

K. Wu, X. Qiang, Z. Xing, and X. Jiang. Buckling in prestressed stayed beam–columns and intelligent evaluation. *Engineering Structures*, 255:113902, 2022. doi: 10.1016/j.engstruct.2022.113902.

S. Wu, Z. Luo, Z. Li, S. Liu, and L.-C. Zhang. Topological design of pentamode metamaterials with additive manufacturing. *Computer Methods in Applied Mechanics and Engineering*, 377:113708, 2021. doi: 10.1016/j.cma.2021.113708.

G. Xia. Generalized foundation Timoshenko beam and its calculating methods. *Archive of Applied Mechanics*, 92(3):1015–1036, 2022. doi: 10.1007/s00419-021-02090-1.

S. Yan, W. Liu, X. Tan, Z. Meng, W. Luo, H. Jin, Y. Wen, J. Sun, L. Wu, and J. Zhou. Bio-inspired mechanical metamaterial with ultrahigh load-bearing capacity for energy dissipation. *Materials Today*, 77:11–18, 2024. doi: 10.1016/j.mattod.2024.06.003.

H. Yang and L. Ma. Multi-stable mechanical metamaterials by elastic buckling instability. *Journal of Materials Science*, 54(4):3509–3526, 2019. doi: 10.1007/s10853-018-3065-y.

Y. Yang, Y. Hui, P. Li, J. Yang, Q. Huang, G. Giunta, S. Belouettar, and H. Hu. Global/local buckling analysis of thin-walled I-section beams via hierarchical one-dimensional finite elements. *Engineering Structures*, 280:115705, 2023. doi: 10.1016/j.engstruct.2023.115705.

G. Ye, H. Bi, Z. Li, and Y. Hu. Compression performances and failure modes of 3d printed pyramidal lattice truss composite structures. *Composites Communications*, 24: 100615, 2021. doi: 10.1016/j.coco.2020.100615.

J.-Z. Zhang and X.-P. Zhou. Fracture process zone (fpz) in quasi-brittle materials: Review

and new insights from flawed granite subjected to uniaxial stress. *Engineering Fracture Mechanics*, 274:108795, 2022. doi: 10.1016/j.engfracmech.2022.108795.

S. Zhang, Y. Ma, and Z. Deng. Analytical solution and experimental verification for the buckling failure of additively manufactured octagonal honeycombs. *Composite Structures*, 303:116306, 2023. doi: 10.1016/j.compstruct.2022.116306.

W. Zhang and J. Xu. Advanced lightweight materials for automobiles: A review. *Materials & Design*, 221:110994, 2022. doi: 10.1016/j.matdes.2022.110994.

J. Zhao, J. He, and Z. Sun. Bending-dominated to compression-dominated transition mechanism in additively-manufactured lattice structures. *Materials Today Communications*, 48:113561, 2025. doi: 10.1016/j.mtcomm.2025.113561.

X. Zheng, H. Lee, T. H. Weisgraber, M. Shusteff, J. DeOtte, E. B. Duoss, J. D. Kuntz, M. M. Biener, Q. Ge, J. A. Jackson, S. O. Kucheyev, N. X. Fang, and C. M. Spadaccini. Ultralight, ultrastiff mechanical metamaterials. *Science (New York, N.Y.)*, 344(6190): 1373–1377, 2014. doi: 10.1126/science.1252291.

H. Zhong, R. Das, J. Gu, and M. Qian. Low-density, high-strength metal mechanical metamaterials beyond the gibson-ashby model. *Materials Today*, 68:96–107, 2023. doi: 10.1016/j.mattod.2023.07.018.

O. C. Zienkiewicz, R. L. Taylor, and J. Z. Zhu. Chapter 1 - the standard discrete system and origins of the finite element method. In O. C. Zienkiewicz, R. L. Taylor, and J. Z. Zhu, editors, *The Finite Element Method: its Basis and Fundamentals (Seventh Edition)*, pages 1–20. Butterworth-Heinemann, Oxford, 2013. ISBN 978-1-85617-633-0. doi: 10.1016/B978-1-85617-633-0.00001-0.

C. Zschernack, M. A. Wadee, and C. Völlmecke. Nonlinear buckling of fibre-reinforced unit cells of lattice materials. *Composite Structures*, 136:217–228, 2016. doi: 10.1016/j.compstruct.2015.09.059.

A total of 159 references.

# A. Material list

Table A.1 provides the list of materials and corresponding material properties used in chapter 3.

Table A.1.: Material used analysis of the brittleness filter. The symbols refer to the methods used to determine the material strength: Yield strength *, Tensile strength $^{+}$, Flexural strength (modulus of rupture) °.

| No. | Name | Strength (MPa) | Fracture Toughness (MPa $m^{1/2}$) | Density ($kg/m^3$) | Young's Modulus (MPa) | Material class | Reference[a] |
|---|---|---|---|---|---|---|---|
| 1 | High carbon steel* | 800 | 59.5 | 7850 | 210000 | Metal | |
| 2 | Nickel alloys* | 585 | 95 | 8900 | 205000 | Metal | |
| 3 | Medium carbon steel* | 605 | 52 | 7850 | 210000 | Metal | |
| 4 | Stainless steel* | 135 | 106 | 7850 | 200000 | Metal | |
| 5 | Aluminium alloys* | 265 | 28.5 | 2700 | 75000 | Metal | |
| 6 | Copper alloys* | 265 | 60 | 8900 | 130000 | Metal | |
| 7 | Low alloy steel* | 950 | 107 | 7850 | 215000 | Metal | |
| 8 | Titanium Aluminide alloy* | 648.8 | 20.4 | 4600 | 93800 | Metal | (Chan, 1990) |
| 9 | Steel AISI5150* | 360 | 23 | 7850 | 140000 | Metal | (Husaini et al., 2019) |
| 10 | CFRP$^{+}$ | 825 | 13.1 | 1550 | 109500 | Composite | |
| 11 | GFRP$^{+}$ | 190 | 15 | 1900 | 21500 | Composite | |
| 12 | PEEK/CF° | 698 | 8.7 | 1600 | 47200 | Composite | (Eremin et al., 2024) |
| 13 | SMC$^{+}$ | 124.3 | 3.2 | 1890 | 12800 | Composite | (da Silva et al., 2025) |
| 14 | PLA natural fiber$^{+}$ | 45 | 4.8 | 1240 | 3000 | Composite | (Ramirez et al., 2024) |
| 15 | Glass fiber/Polyamide$^{+}$ | 705 | 34.2 | 1690 | 30100 | Composite | (Reza Torabi et al., 2025) |
| 16 | ABS* | 35 | 2.75 | 1100 | 2000 | Polymer | |
| 17 | Epoxies* | 54 | 1.3 | 1250 | 2750 | Polymer | |
| 18 | PEEK* | 80 | 3.5 | 1300 | 3900 | Polymer | |
| 19 | PP* | 29 | 3.75 | 900 | 1250 | Polymer | |
| 20 | PTFE* | 20 | 1.55 | 2150 | 475 | Polymer | |
| 21 | PA* | 72.2 | 3.9 | 1100 | 2900 | Polymer | |
| 22 | PET* | 59.5 | 5 | 1350 | 3450 | Polymer | |
| 23 | Alumina° | 370 | 4.05 | 3900 | 365000 | Ceramic | |
| 24 | Alumina nitride° | 325 | 2.95 | 3300 | 325000 | Ceramic | |
| 25 | Silicon° | 170 | 0.885 | 2350 | 150000 | Ceramic | |

Continued on next page

[a]Material data is from (Ashby, 2016) unless otherwise noted.

**Table A.1 – continued from previous page**

| No. | Name | Strength (MPa) | Fracture Toughness (MPa $m^{1/2}$) | Density ($kg/m^3$) | Young's Modulus (MPa) | Material class | Reference[a] |
|---|---|---|---|---|---|---|---|
| 26 | Silicon carbide° | 505 | 4.3 | 3150 | 430000 | Ceramic | |
| 27 | Tungsten carbides° | 460 | 2.9 | 10550 | 665000 | Ceramic | |
| 28 | Wood, across grain$^+$ | 4 | 0.65 | 730 | 1750 | Natural mat. | |
| 29 | Wood, along grain$^+$ | 50 | 7 | 700 | 13000 | Natural mat. | |
| 30 | Mongolian Scots pine$^+$ | 59.7 | 1.38 | 514 | 9825 | Natural mat. | (Ji et al., 2022) (Konofalska et al., 2021) |
| 31 | Black Walnut$^+$ | 287 | 5.18 | 660 | 9800 | Natural mat. | (Ji et al., 2022) (Forest Products Laboratory, 1999) |

[a]Material data is from (Ashby, 2016) unless otherwise noted.

# Declaration of generative AI and AI-assisted technologies in the writing process

ChatGPT/OpenAI and DeepL Write were used to edit the language of individual sections during the preparation of this work. After using this tool, the text was reviewed and edited as needed. I take full responsibility for the content of this work.